Optical Properties and Transport Properties of Hydrogenated Amorphous Silicon

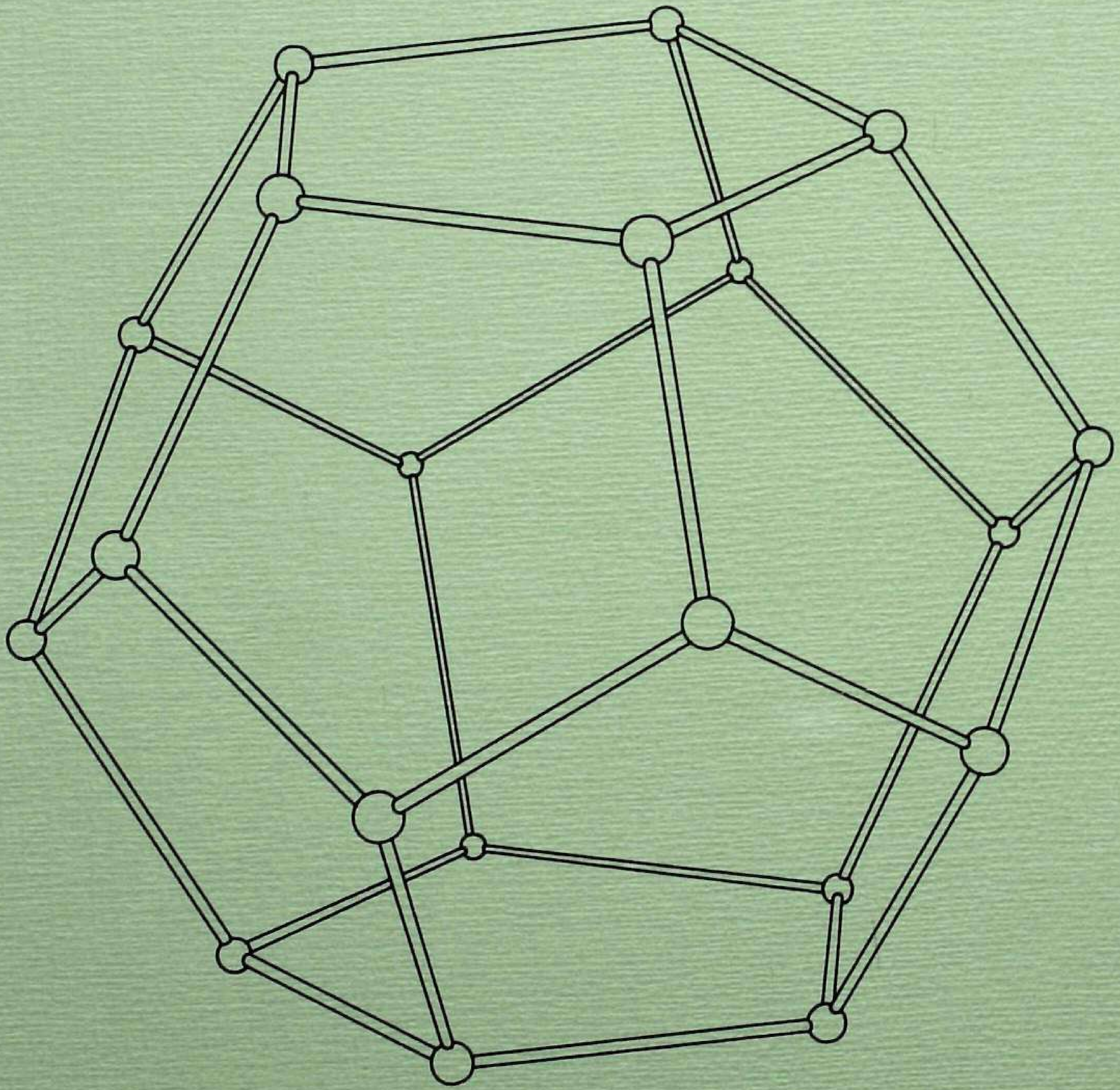

Johan van den Heuvel

Optical Properties and Transport Properties
of
Hydrogenated Amorphous Silicon

Optical Properties and Transport Properties of Hydrogenated Amorphous Silicon

Proefschrift

ter verkrijging van de graad van doctor
aan de Technische Universiteit Delft,
op gezag van de Rector Magnificus,
prof.drs. P. A. Schenck, in het openbaar
te verdedigen ten overstaan van een commissie
aangewezen door het College van Dekanen,
op maandag 11 december 1989 te 14.00 uur

door

Johannes Cornelis van den Heuvel

geboren te Sommelsdijk
doctorandus in de experimentele natuurkunde

Dit proefschrift is goedgekeurd door de
promotor prof.dr. M. Kleefstra

Τὴν τοῦ γεγονότος ὁρατοῦ
καὶ πάντως αἰσθητοῦ μητέρα...
μήτε γῆν μήτε ἀέρα μήτε πῦρ μήτε ὕδωρ
λέγωμεν..., ἀλλ’ ἀνόρατον εἰδός τι
καὶ **ἄμορφον**... καὶ δυσαλωτότατον....

The mother of all created and visible things...
is neither earth nor air nor fire nor water...,
but an invisible and **formless** being,
and she is most incomprehensible...

Plato, Timaeus 51a

Aan mijn moeder

Aan Heddi

Preface

Hydrogenated amorphous silicon (a-Si:H) is a semiconductor that can be used for thin film solar cells. In this work the properties of a-Si:H that are relevant to the performance of a-Si:H solar cells are studied.

This thesis is a result of the research project "*Hoge efficiency zonnecellen*" that was was initiated by the International Solar Energy Society (ISES) and financed by the ministry of Economic affairs of the Dutch government.

The scope of this thesis is the optical properties and transport properties of a-Si:H. These properties are closely related to the performance of a-Si:H solar cells, since the absorption of light and the transport of the generated electrons and holes determine the efficiency of the solar cell. The optical properties are studied in chapter 3, after the introductory chapters 1 and 2, and the transport properties are studied in chapters 4 and 5. The study presented in this thesis is directed at increasing the understanding of the material in relation to the practical application of a-Si:H in solar cells.

In chapter 3 the optical properties, in particular the refractive index and the optical bandgap, are studied in relation to the hydrogen concentration in the a-Si:H layer. The influence of the hydrogen concentration is described by making use of a model for the incorporation of hydrogen in the a-Si:H layer, the concept of bond polarizabilities, and the concept of atomic oscillators.

In chapter 4 the diffusion length of a-Si:H is studied. The diffusion length is the average distance that a generated hole travels before it recombines with an electron, and is therefore a measure for the quality of the a-Si:H layer.

In chapter 5 the Space Charge Limited Current (SCLC) method is investigated. This method measures the density of states in the bandgap of a-Si:H. These states in the bandgap decrease the electric field in the solar cell and increase the recombination of electrons and holes. Therefore, the density of states must be low in high efficiency solar cells.

Delft, 1989 *J.C. van den Heuvel*

Contents

Chapter 1

General Introduction

1.1 History

Hydrogenated amorphous silicon (a-Si:H) is a member of the large class of thin film materials that are commonly called amorphous semiconducting films. A thin film is usually called amorphous if its diffraction *pattern consists of a few broad rings and if its corresponding radial* distribution function differs significantly from that of a (micro)crystalline film of the same material [1]. The radial distribution function is the average number of atoms per unit volume at a distance r, measured from any atom. The radial distribution functions for amorphous silicon (without hydrogen) and for crystalline silicon are shown in figure 1.1.

These amorphous semiconducting films are used for a broad range of applications such as, xerography, protective coatings, and optical coatings [3]. There have also been many studies on their fundamental properties. From these studies the concepts of mobility gap and localized tail states have emerged. It was found that in spite of the lack of long-range order there existed a gap in the distribution of electron states where the number of states is low. Inside this gap, known as the mobility gap, the states are localized while outside the gap the states are delocalized and are called extended states [4]. The localized states in the mobility gap are called tail states, because these states are concentrated at the edge of the valence band and at the edge of the *conduction band.*

Before hydrogenated amorphous silicon (a-Si:H) could be used for the application of solar cells two important breakthroughs had to be made, the reduction of the density of states in the gap and the ability

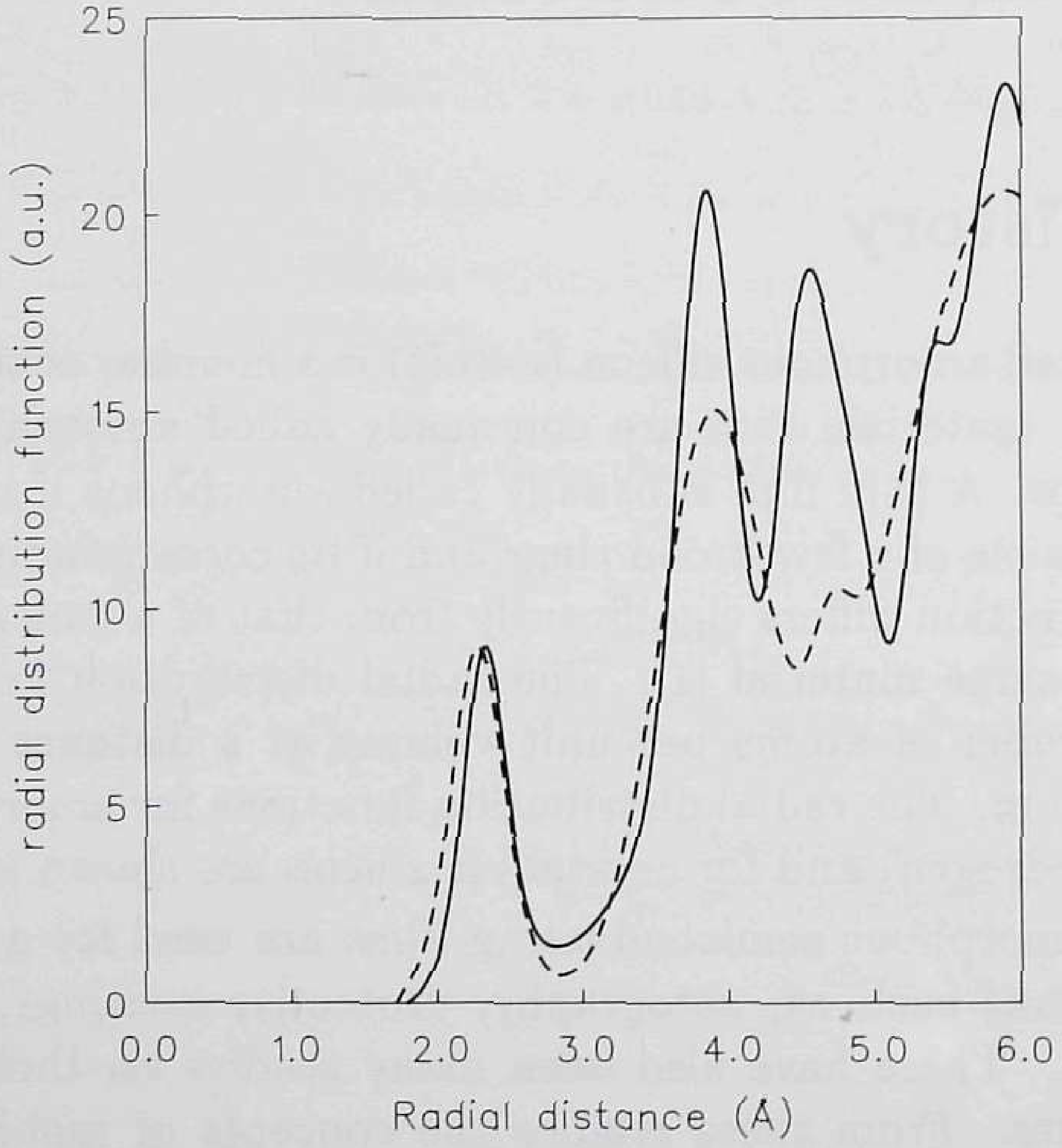

Figure 1.1: Radial distribution function of amorphous (dashed line) and crystalline silicon (solid line) as determined from the analysis of electron diffraction data. (From Moss and Graczyk [2]).

to dope the material. The first breakthrough was achieved by Chittick who used the radio-frequency glow discharge technique to deposit films of a-Si:H from silane gas (SiH_4) [5]. The doping of this material was investigated by Spear and LeComber who added phosphine (PH_3) and diborane (B_2H_6) to silane to obtain n- and p-doping, respectively [6]. They were able to increase the conductivity by a factor 10^6. That amorphous semiconductors could be doped at all was a major breakthrough since it was believed that every impurity atom would be incorporated in the amorphous network according to its natural valence [7,8].

In 1976 D.E. Carlson and C.R. Wronski succeeded in fabricating the first solar cell based on a-Si:H, the efficiency at that time was 2.4 % [9]. From that time the efficiency of a-Si:H solar cells has increased to 13.6 % [10]. This increase has been obtained by optimizing the cell structure, by the use of important new materials such as silicon-carbide alloys for the window-side material, and by new designs such as a two stacked a-Si:H solar cells [11].

1.2 Structure

At first sight it seems contradictory to speak of the structure of an amorphous material (amorphous comes from the Greek word amorphos meaning without shape). It is true that amorphous material lacks the rigid structure of the crystal lattice, however the atoms are not completely randomly distributed as in a gas. For amorphous silicon (without hydrogen) the radial distribution function has been obtained from diffraction measurements (X-ray, electron, and neutron diffraction) [12,2,13]. It was found (see figure 1.1) that there are two well defined shells one of four nearest neighbours and one of twelve next-nearest neighbours, at longer distances there are no longer clearly separable coordination shells. This shows that in amorphous silicon there is short-range order but no long-range order. There used to be a controversy as to whether the radial distribution function could be caused by microcrystals. At the moment the random-network model is more popular than the microcrystalline model. A random-network of silicon atoms can be constructed by connecting every silicon atom with four neighbours, but allowing a variation in bond angle to cause a loss of

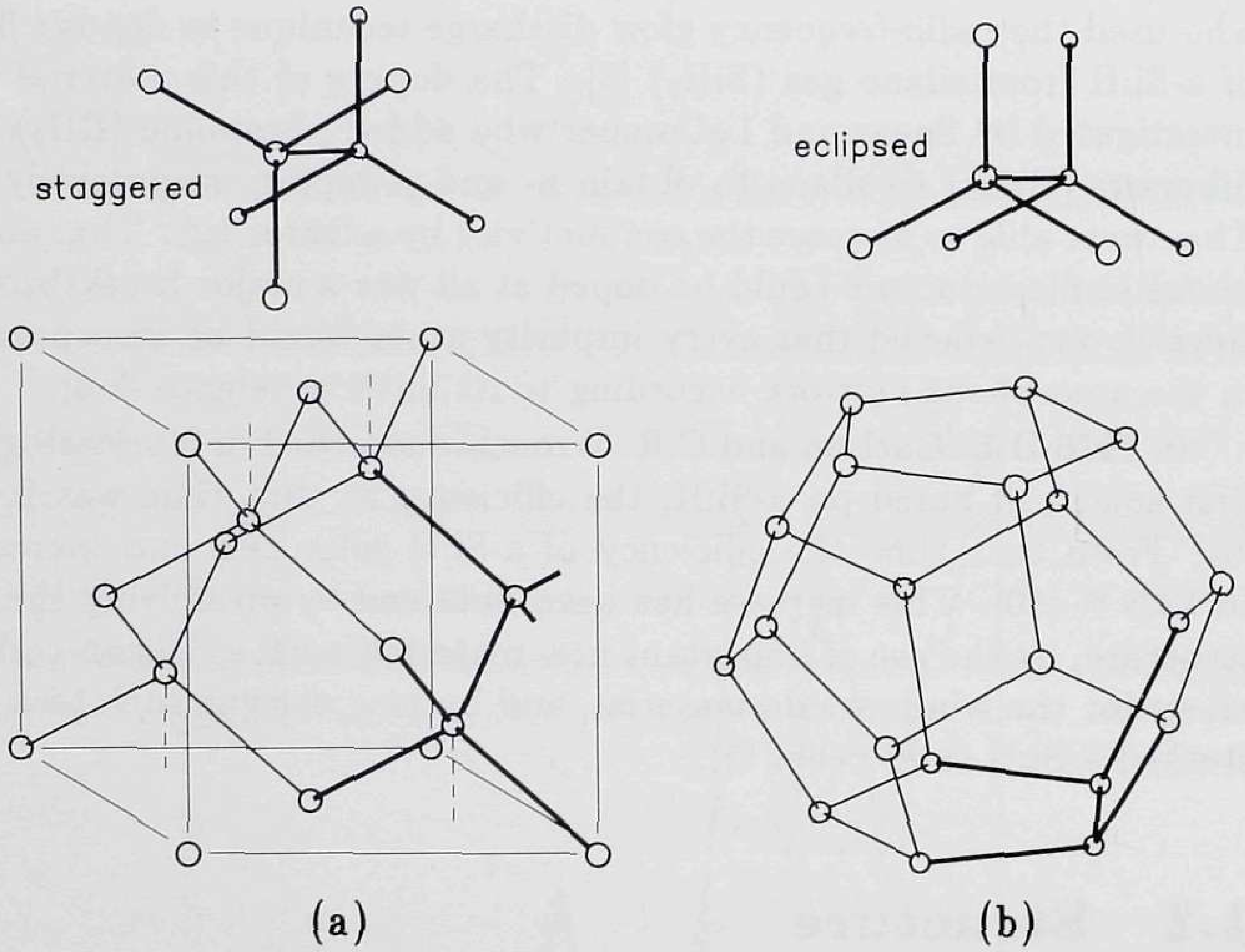

Figure 1.2: The unit cell of crystalline silicon (a) and an amorphon (b). In the amorphon the silicon bonds are "eclipsed" while in crystalline silicon the bonds are "staggered".

local order and ultimately to cause the absence of long-range order [14].

The random-network of silicon atoms must agree with the radial distribution function shown in figure 1.1. It can be seen in figure 1.1 that the third-neighbour peak present in crystalline silicon is absent in amorphous silicon. In figure 1.2 the unit cell of crystalline silicon and an "amorphon" (see [4], page 325) are shown. In the unit cell of crystalline silicon the bonds are "staggered", while in the amorphon the bonds are "eclipsed". These two units have different third-neighbour distances. The amorphon units cannot fill space completely, therefore in amorphous silicon only a fraction of the random-network may consist of amorphons.

In the case of hydrogenated amorphous silicon (a-Si:H) the problem of structure is even more difficult. Because of the hydrogen content there are three radial distribution functions, namely the Si-Si, Si-H, and H-H pairs. There have been attempts to obtain these radial distribution functions from neutron diffraction experiments [15]. Another method that is used to derive the structure of a-Si:H is infrared absorption spectroscopy. The vibrational spectra of a-Si:H films when compared with those of gaseous silanes seem to show that much of the hydrogen is attached to silicon by ordinary covalent bonds. A silicon atom may be bound to one, two, or three hydrogen atoms, in which case these atomic groups are referred to as mono-, di-, or trihydrides, respectively.

Since a-Si:H is an alloy of hydrogen and silicon the question arises whether a-Si:H is homogeneous. There is experimental evidence from NMR (nuclear magnetic resonance) measurements that a-Si:H may have regions with a diameter between 10 Å and 100 Å. Some of these regions are poorer and some are richer in hydrogen than the average composition [16,17,18,19]. The above-mentioned regions of higher and lower hydrogen content suggest that the material is not homogeneous. In addition to compositional inhomogeneity there is also structural inhomogeneity commonly called voids or microcracks [20]. These two kinds of inhomogeneity may be connected, for instance, the hydrogen may be clustered in voids [21].

At the present time there is no consensus about the role of microstructure in device-quality material using the word microstructure as it is often used to encompass all kinds of structures of a larger scale than the atomic scale. A problem is that the terminology for the different kinds of microstructure is derived from experimental data that have been obtained from material that has been deposited under different conditions than the conditions that are normally used to make devices.

An important question is whether this microstructure, the compositional and structural inhomogeneity, depends on the film thickness. The reason for this is that a growth structure, the so-called columnar structure, is found in amorphous silicon deposited at low temperatures [18,22,23]. However, there is no clear evidence that this columnar structure exists in a-Si:H deposited at conditions that are used to obtain device-quality material [20]. Perhaps there is a growth structure at these conditions; in that case the quality of the material near the substrate will be different from the material at the top of the layer.

As this short introduction to the structure of amorphous silicon shows, there is structure in the material. It is, however, difficult to correlate this structure to optical and transport properties, because of the lack of a theoretical framework and also the lack of exclusive experimental data.

1.3 Band Theory

The concept that the one electron states in a crystal are separated in bands, with an upper and lower energy bound, emerges directly from the long-range order. In the crystal we have a periodic potential of the form:

$$U(\vec{r}+\vec{R}) = U(\vec{r}) \,, \tag{1.1}$$

where $\vec{r}$ is the space coordinate and $\vec{R}$ is a translation vector that maps the infinite crystal on itself. This gives us the following solution to the Schrodinger equation:

$$\psi(\vec{r}+\vec{R}) = e^{i\vec{k}\cdot\vec{R}}\psi(\vec{r}) \,, \tag{1.2}$$

where $\vec{k}$ is the wave vector. This solution is called Bloch's theorem and it can be shown that the energy is of the form $E_n(\vec{k})$, where n represents the different discrete solutions of the Schrodinger equation for a certain $\vec{k}$ [24]. It follows directly from equation 1.2 that $E_n(\vec{k})$ is periodic in $\vec{k}$ and continuous and has therefore an upper and lower bound. This shows that all the levels $E_n(\vec{k})$ lie in a band of energies.

In amorphous silicon there is no long-range order and calculations that use Bloch's theorem are impossible. However, there is substantial experimental evidence that there is a bandgap in amorphous silicon without long-range order.

Band theory calculations of an amorphous material use a modification of the solution of Bloch's theorem. The Bloch wave function for an electron in a crystal can be written as

$$\psi(\vec{r}) = \sum_{\vec{R}} e^{i\vec{k}\cdot\vec{R}}\phi(\vec{r}-\vec{R}) \,, \tag{1.3}$$

where ϕ is an atomic wavefunction. It is easily verified that equation 1.3 agrees with Bloch's theorem (equation 1.2). Equation 1.3 is modified

by introducing random phases

$$\psi_{\mathrm{am}}(\vec{r}) = \sum_{\vec{R}} A_{\vec{R}}\,\phi(\vec{r}-\vec{R}) \,, \tag{1.4}$$

where the $A_{\vec{R}}$ are random in phase and amplitude. These calculations result in localized states [4]. If states are localized, then an electron (or hole) can move from one state to another state only through thermal activation. Mott (see [4], pages 15–27) pointed out that if the disorder is less than a critical value, a tail to the nonlocalized (energy) band exists and the states in the band tail are localized. The localized states in the band tails are separated from the nonlocalized states by sharp energy levels. These energy levels are called E_c and E_v; E_c for the transition from localized to nonlocalized in the conduction band and E_v for the transition in the valence band.

1.4 Density of States

There are two models for the density of states in the gap of a-Si:H that are often used. The oldest model was proposed by Cohen, Fritzsche, and Ovshinsky [25]. This model is called the CFO model and is shown in figure 1.3a. In this model the gap states are formed by overlapping tails of localized states. The states derived from the valence band are neutral when full and the states derived from the conduction band are neutral when empty. In the model proposed by Mott (see [4], pages 210–215), shown in figure 1.3b, the band tails are located close to the mobility edges E_v and E_c and the states in approximately the middle of the gap originate from defects acting both as donors and acceptors (for example, dangling bonds).

A distinction between shallow states and deep states can be made. Shallow states are the states located near the mobility edges while deep states are located in approximately the middle of the gap. The states that are close to the mobility edges are usually called the tail states and are attributed to the absence of long-range order. This means that the tail states are correlated to the bond angle and bond length deviation [26]. Whether there are also *deep* tails in a-Si:H as in the CFO model is not clear. These deep tails should arise only from gross density or bond-angle fluctuations (see [4], page 211).

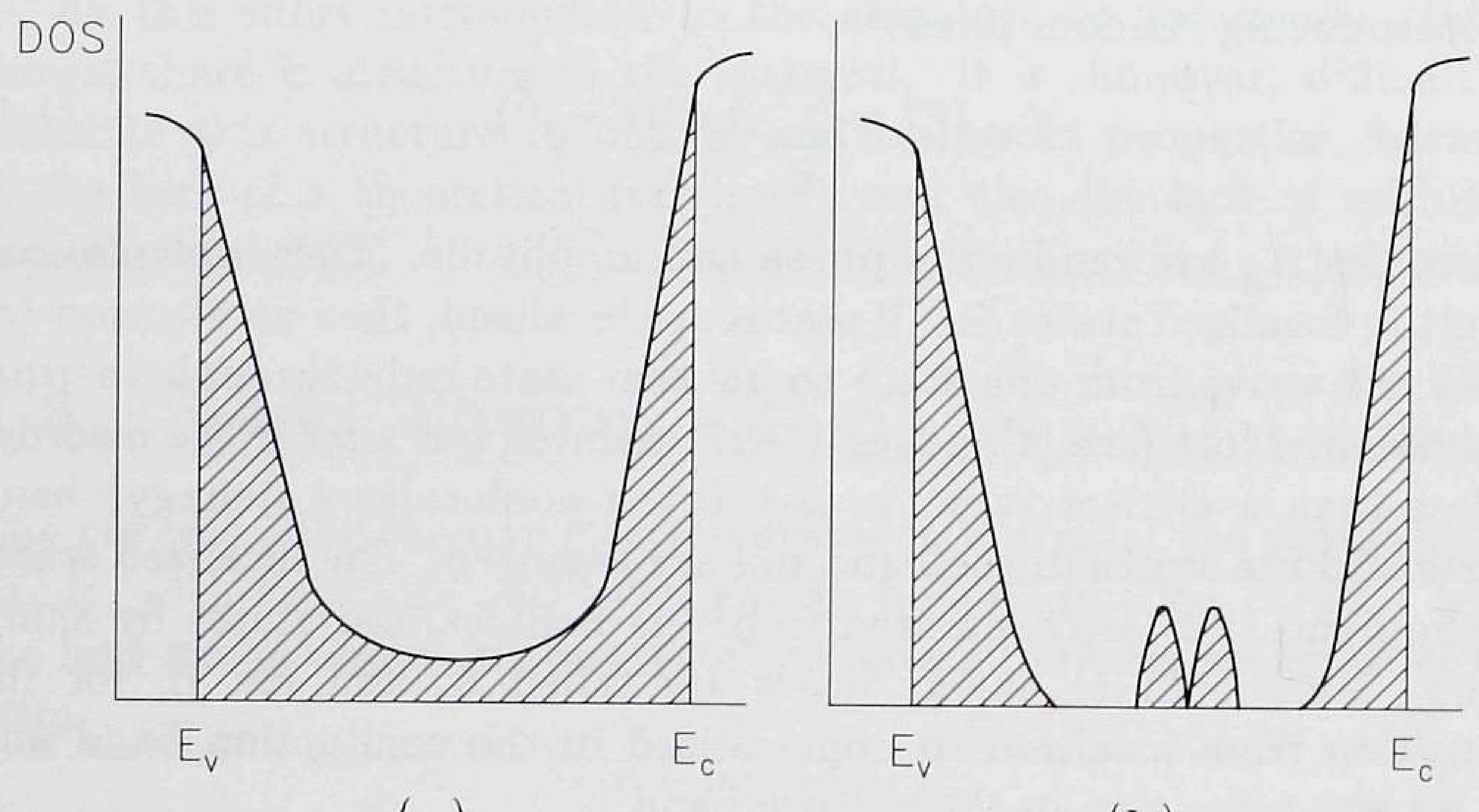

(a) (b)

Figure 1.3: Two proposed forms for the density of states in a-Si:H: (a) the CFO model with overlapping conduction and valence band tails; (b) the model proposed by Mott with shallow band tails and defect levels in approximately the middle of the gap.

The states in approximately the middle of the gap are normally attributed to defects. These defects can be regarded as disturbances of the continuous random-network. These defects can give a density of states concentrated in the middle of the gap as in the model of Mott (see figure 1.3b). However, a gap states distribution resembling the CFO model due to defects is also possible. This last distribution was proposed by Lecomber and Spear [27], who suggested a defect distribution in the form of two overlapping tails.

There is still uncertainty about the kind of defect that is the most prominent. The dangling silicon bond is considered by many to be the most important defect and is also the most simple to imagine. It is, however, not the only possible defect, for instance, Pantelides has proposed the five-fold coordinated silicon atom as a defect and called it a floating bond [28]. Other possible defects are the two-fold coordinated silicon atom, three-center bonds, intimate pairs, and other defects [29].

There is much discussion about the correlation energy of the dangling bond. The correlation energy is the difference in energy between an electron in a singly occupied dangling bond and an electron in a double occupied dangling bond, see figure 1.4. A negative correlation energy would mean that dangling bonds that are singly occupied are less stable than empty and double occupied dangling bonds. In this case the dangling bonds will exchange electrons to form empty and double occupied dangling bonds.

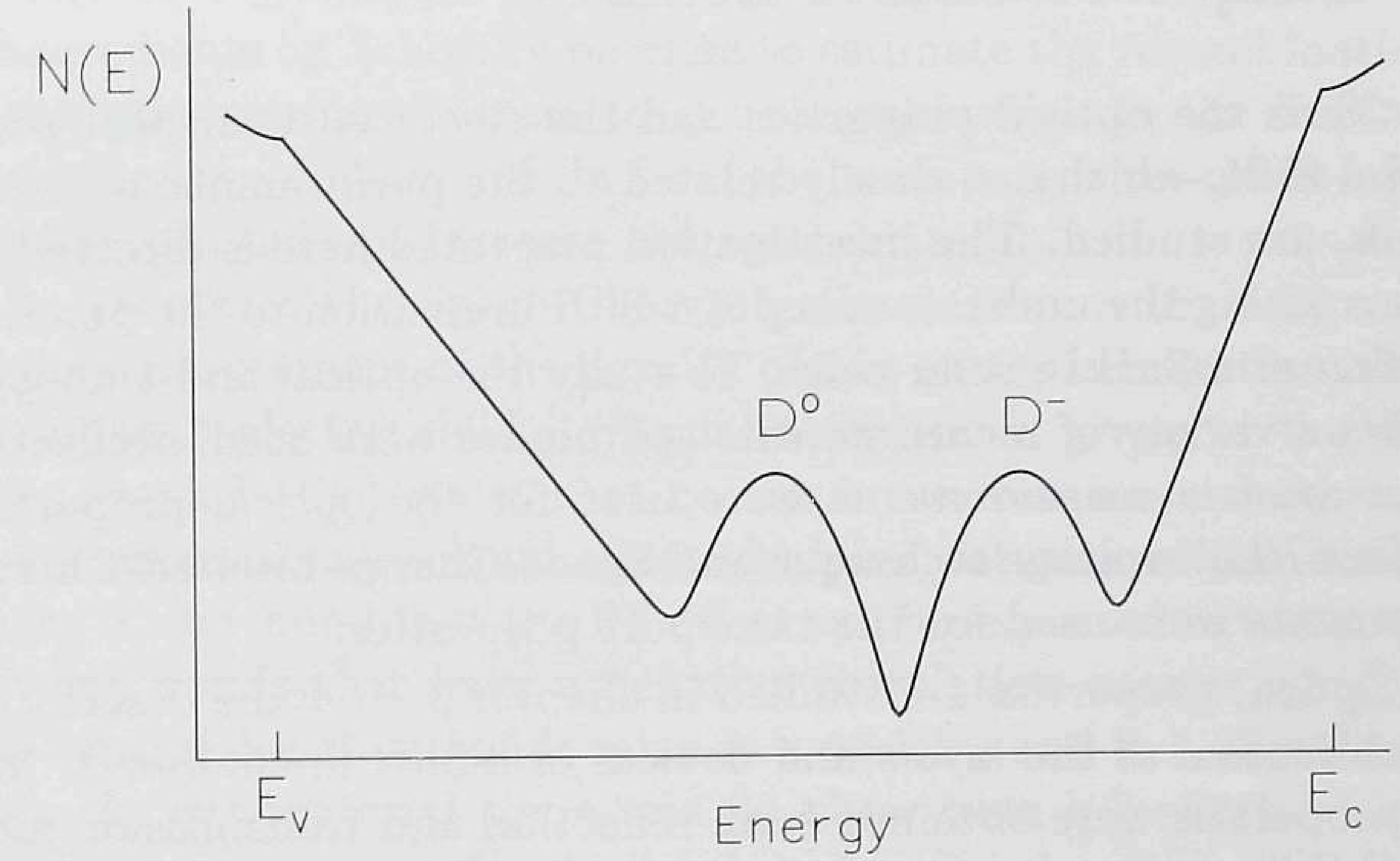

Figure 1.4: The energy levels of a single occupied and double occupied dangling bond. D^0 and D^- indicate the single and double occupied dangling bond.

The effect of defects on the electronic properties differs from the effect of the tail states. In a solar cell we have two kinds of charge carriers, namely holes and electrons. The tail states reduce the effective mobility of the holes and electrons, because most of the carriers are trapped in the tail states and only take part in the conduction when they are thermally excited into the extended states in the conduction band and valence band. The defects are effective recombination centers which reduce the lifetimes of the carriers. The defects also control the band-bending in the same way as donors and acceptors in crystalline semiconductors. This band-bending results in a low electric field and this will reduce the drift velocity and the collection of the carriers. These effects show that the understanding and reduction of tail states and defects in solar cells is of great importance.

1.5 Scope of this Thesis

In this thesis the optical properties and the electrical transport properties of a-Si:H, which are closely related to the performance of a-Si:H solar cells, are studied. The investigation presented here is directed towards increasing the understanding of a-Si:H in relation to the practical application of a-Si:H in solar cells. To study the optical and transport properties a variety of measurements techniques were used. Reflection and transmission measurements were used for the optical properties; the Surface Photovoltage technique and Space-Charge-Limited-Current measurements were used for the transport properties.

The optical properties are studied in chapter 3 after the description of the fabrication of the layers and devices of a-Si:H in chapter 2. The optical properties were obtained from reflection and transmission measurements. The theory of harmonic oscillators on an atomic scale is used as a starting point instead of the more conventional band theory. A model for the incorporation of hydrogen in the a-Si:H layer will be introduced to describe the relations between the hydrogen concentration in the layer, the refractive index, and the optical gap.

The inhomogeneity of microcrystalline silicon (μc-Si:H) was also studied using reflection and transmission measurements. Microcrystalline silicon consists of microcrystals of approximately 100 Å in diameter surrounded by a-Si:H. This material (μc-Si:H) can be used for the first layer in a solar cell because of its low light absorption and high conductivity. It will be shown that the first 200 Å of a μc-Si:H layer is amorphous. This thin interfacial layer has to be eliminated to obtain solar cells with high efficiency.

In chapter 4 the Surface Photovoltage (SPV) technique is used to measure the diffusion length. The diffusion length in a-Si:H is the average distance that a generated hole travels before it recombines with an electron. The diffusion length is a parameter that is closely related to the performance of a solar cell. In a solar cell the current is limited by the recombination of the generated holes and electrons and the diffusion length is a direct measure of this recombination. It will be shown that the term "diffusion length" is misleading, since the hole drift current is of the same order of magnitude as the hole diffusion current. This hole drift current increases the diffusion length by a factor $\sqrt{2}$.

The SPV technique is used in combination with current-voltage measurements on Schottky barriers to estimate the recombination close to the substrate in contrast to the recombination in the bulk. It was found that the diffusion of tin from the transparent tin-oxide layer used in solar cells did not increase the recombination.

In chapter 5 the Space-Charge-Limited-Current (SCLC) technique for the measurement of the density of gap states is investigated for the case of high electric fields. Special attention is given to the so-called Poole-Frenkel (PF) effect that occurs in various amorphous semiconductor materials and could affect the interpretation of the SCLC technique. It was found that the PF effect can be expected in materials with dangling bonds that have a negative correlation energy, which means that neutral dangling bonds relax in a positive and in a negative charge state. In our material there was no observable PF effect which gives additional support to the theory that dangling bonds in a-Si:H have a positive correlation energy.

The density of gap states obtained by the SCLC method shows a large temperature dependence, however, the density of gap states of a-Si:H is supposed to be independent of the temperature. It will be shown that the temperature dependence is caused by the tail states near the conduction band edge, and not by a change in the density of gap states.

References

[1] R. Grigorovici. Amorphous semiconducting thin films. *Thin Solid Films*, 9:1–23, 1971.

[2] S.C. Moss and J.F. Graczyk. In *Proc. 10th Int. Conf. on the Physics of Semicond.*, page 658, 1970.

[3] R. Grigorovici. Amorphous semiconducting films: physical background of applications. *Thin Solid Films*, 12:153–166, 1972.

[4] N.F. Mott and E.A. Davis. *Electronic Processes in Non-Crystalline Materials*, chapter 1. Clarendon Press, 2 edition, 1979.

[5] R.C. Chittick, J.H. Alexander, and H.F. Sterling. The preparation and properties of amorphous silicon. *J. Electrochem. Soc.*, 116(1):77–81, January 1969.

[6] W.E. Spear and P.G. Le Comber. Substitutional doping of amorphous silicon. *Solid State Comm.*, 17(9):1193–1196, 1975.

[7] N.F. Mott. *Adv. Phys.*, 16:49, 1967.

[8] R.W. Haisty and H. Krebs. *J. Non-Cryst. Solids*, 1:399, 1969.

[9] D.E. Carlson and C.R. Wronski. Amorphous silicon solar cell. *Appl. Phys. Lett.*, 28(11):671–673, June 1976.

[10] S. Guha, J. Yang, P. Nath, and M. Hack. Enhancement of open-circuit voltage in high efficiency amorphous silicon solar cells. *Appl. Phys. Lett.*, 49(4):218, 1986.

[11] Y. Hamakawa and H. Okamoto. *Amorphous Semiconductor Technologies and Devices*, chapter 5, pages 200–211. Volume 16, Elsevier Science Publishers, 1984.

[12] S.C. Moss and J.F. Graczyk. *Phys. Rev. Lett.*, 23:1167, 1969.

[13] L. Guttman. *Semiconductors and Semimetals*, chapter 11, pages 225–246. Volume 21A, Academic Press, London, 1984.

[14] Zachariasen. *J. Am. Chem. Soc.*, 54:3841, 1932.

[15] T.A. Postol, C.M. Falco, R.T. Kampwirth, and I.K. Schuller. Structure of amorphous silicon and silicon hydrides. *Phys. Rev. Lett.*, 45(8):648–652, 1980.

[16] J.A. Reimer and R.W. Vaughan. Proton nmr studies of annealed plasma-deposited amorphous si:h films. *Solid State Comm.*, 37(2):161–164, 1981.

[17] W.E. Carlos and P.C. Taylor. Hydrogen-associated disorder modes in amorphous Si:H films. *Phys. Rev. Lett.*, 45(5):358–362, 1980.

[18] J.C. Knights and R.A. Lujan. Microstructure of plasma-deposited a-Si:H films. *Appl. Phys. Lett.*, 35(3):244–246, 1979.

[19] P. D'Antonio and J.H. Konnert. Small-angle-scattering evidence of voids in hydrogenated amorphous silicon. *Phys. Rev. Lett.*, 43(16):1161–1163, 1979.

[20] A. Chenevas-Paule. *Semiconductors and Semimetals*, chapter 12, pages 247–271. Volume 21A, Academic Press, London, 1984.

[21] M.H. Brodsky. Quantum well model of hydrogenated amorphous silicon. *Solid State Comm.*, 36(1):55–59, 1980.

[22] Thornton. Influence of apparatus geometry and deposition conditions on the structure and topography of thick sputtered coatings. *J. Vac. Sci. Technology*, 11(4):666–670, 1974.

[23] W. Paul. Closing address. In *Proc. Int. Conf. on Amorph. and Liq. Semicond.*, pages 1165–1171, 1981.

[24] N.W. Ashcroft and N.D. Mermin. *Solid State Physics*, pages 132–145. Holt-Saunders International Editions, 1976.

[25] M.H. Cohen, H. Fritzsche, and S.R. Ovshinsky. *Phys. Rev. Lett.*, 22:1065, 1969.

[26] S. John, C. Soukoulis, M.H. Cohen, and E.N. Economou. Theory of electron band tails and the urbach optical-absorption edge. *Phys. Rev. Lett.*, 57(14):1777–1780, 1986.

[27] P.G. LeComber and W.E. Spear. *Topics in Applied Physics*, chapter 9, pages 251–285. Volume 36, Springer-Verlag, 1979.

[28] S.T. Pantelides. Defects in amorphous silicon: a new perspective. *Phys. Rev. Lett.*, 57(23):2979–2982, 1986.

[29] D. Adler. *Semiconductors and Semimetals*, chapter 14, pages 291–318. Volume 21A, Academic Press, London, 1984.

Chapter 2

Fabrication of Films and Devices of Hydrogenated Amorphous Silicon

2.1 Introduction

The radio frequency (rf) glow discharge technique is the deposition technique which led to the improvement of the electronic properties of hydrogenated amorphous silicon (a-Si:H) that made electronic devices possible [1]. In this deposition technique the silane feed gas (SiH_4) decomposes under the impact of electrons in the plasma. The rf plasma is inductively or capacitively coupled with an rf generator that provides the energy for the plasma. The two coupling methods are sketched in figure 2.1. The capacitively coupled reactor using two parallel plates can be scaled up easily and is used more often than the inductively coupled reactor [2]. The plasma emits light as electrons fall back from an excited state to a lower state, and this accounts for the term "glow discharge".

The glow discharge decomposition of silane is normally used in the substrate temperature range of 150°C up to 300°C. The low temperatures and the amorphous character of the material make it possible to deposit a-Si:H on a wide range of substrates. Cheap substrates such as glass plates and steel foil have been used to deposit solar cells on. An interesting substrate that has been used to fabricate solar cells on is a substrate in the form of a roof tile. The use of this type of roof tiles can reduce the cost of a solar energy system because of the low installation cost [3].

The glow discharge technique is a versatile process. The a-Si:H can be doped in the gas phase by adding a small amount of doping

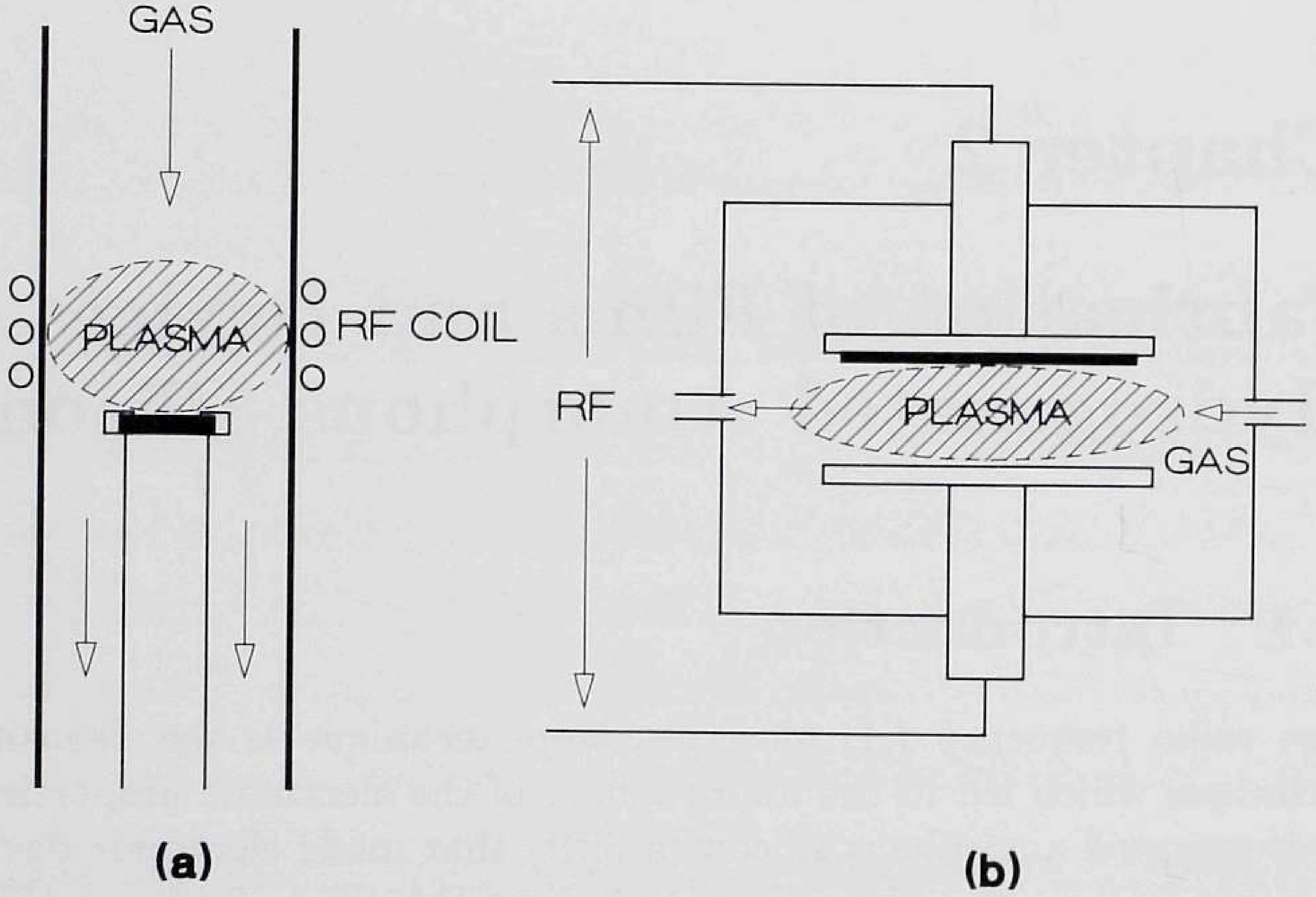

Figure 2.1: Diagrams illustrating experimental methods for glow discharge deposition: (a) inductive coupling of the rf, (b) capacitance coupling.

gases to the silane feed gas. Phosphine (PH_3) is added to obtain n-type films, and diborane (B_2H_6) is added to obtain p-type films. It is also possible to increase or decrease the bandgap by mixing the silane with gases such as methane (CH_4), ammonia (NH_3) or germane (GeH_4). The alloys that are obtained unfortunately have more defects than the a-Si:H material. There is considerable ongoing research to improve the quality of amorphous silicon germanium (a-SiGe:H) since this material is very promising for tandem-type solar cells [4]. The a-SiGe:H alloy has a lower bandgap than a-Si:H and thus can be used to absorb the light (of long wavelength) that is not absorbed by the a-Si:H.

There is still a lot of research going on directed towards understanding and improving the glow discharge deposition. Efforts are directed towards the increase of the deposition rate and the improvement of the quality of a-Si:H and its alloys [5,6].

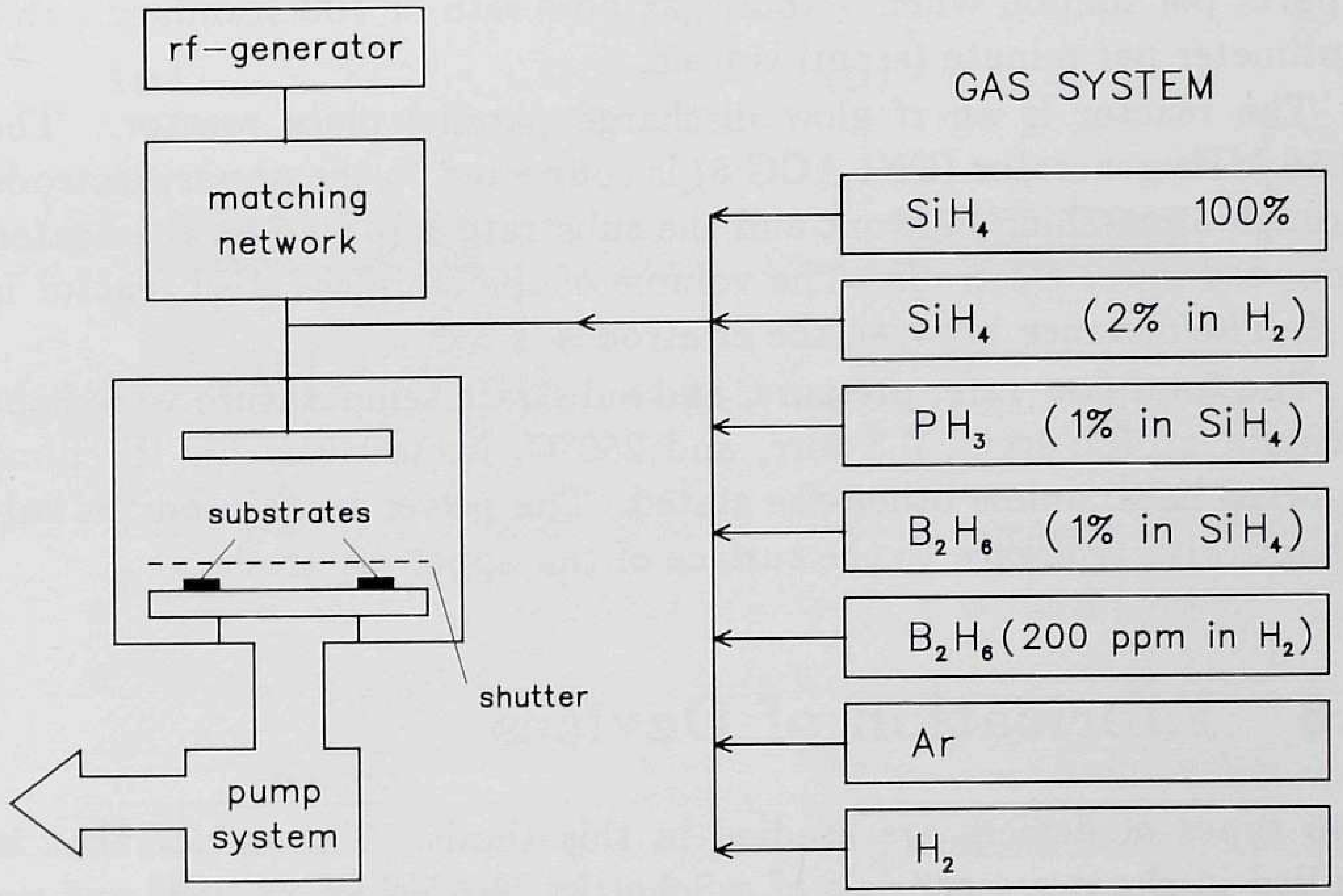

Figure 2.2: The glow discharge reactor that was used to deposit the a-Si:H films reported in this thesis.

2.2 The Glow Discharge Reactor

The apparatus used for the deposition of a- and μc-Si:H films is schematically given in figure 2.2. The system consists of three main parts:

- The reactor chamber, fabricated by the Japanese firm Samco, model PD 10.
- The vacuum pump system, in our case a rotary pump with a capacity of 45 m^3/h which keeps the pressure during the deposition at around 0.3 torr.
- The gas handling system, fabrication ASM. The gas flow rates are controlled by electronic mass flow controllers with an accuracy of 1%. Mixing of the gases takes place in the common gas tube leading to the reactor.

The combined leak/desorption rate of the system is below 2.10^{-5} torr.ℓ/s. This gives a background contamination level in the gas below

5 parts per million when a total gas flow rate of 100 standard cubic centimeter per minute (sccm) is used.

The reactor is an rf glow discharge parallel plate reactor. The 13.56 MHz generator (ENI ACG 5) is connected to the upper electrode through a matching network and the substrate is placed on the heated grounded lower electrode. The volume of the stainless steel reactor is 17 ℓ. The distance between the electrodes is 5 cm.

The total flow rate, pressure, and substrate temperature were kept constant at 100 sccm, 0.3 torr, and 250°C, respectively for the films reported here, unless otherwise stated. The power level in cm^2 is calculated with reference to the surface of the upper electrode.

2.3 Fabrication of Devices

Two types of devices are studied in this thesis. The device that is studied in chapter 4 consists of a Schottky barrier on one side and an ohmic contact on the other side. This device structure will be referred to as an i-n structure. The device that is studied in chapter 5 consists of two ohmic contacts, and it will be referred to as an n-i-n structure. These two device structures, the i-n and n-i-n structures, are depicted in figure 2.3.

Both device structures have at least one ohmic contact. The ohmic contact consists of a metal layer on top of a heavily doped n-type layer (n^+-layer). The use of a heavily doped layer results in a thin barrier between the semiconductor and the metal, and electrons can easily tunnel through this thin barrier. The Schottky barrier on the other hand consists of a metal/intrinsic-a-Si:H interface, and a large barrier between the semiconductor and the metal is formed which results in a rectifying contact [7].

The deposition conditions that are used for the different layers in the devices are listed in table 2.1. These are the standard conditions that are used unless stated otherwise. A shutter was used to shield the substrates from the ignition of the glow discharge plasma. After stabilization of the plasma the shutter was removed. The shutter was not used for several i-n structures and this had a substantial effect on the quality of the diodes. This effect is discussed in chapter 4.

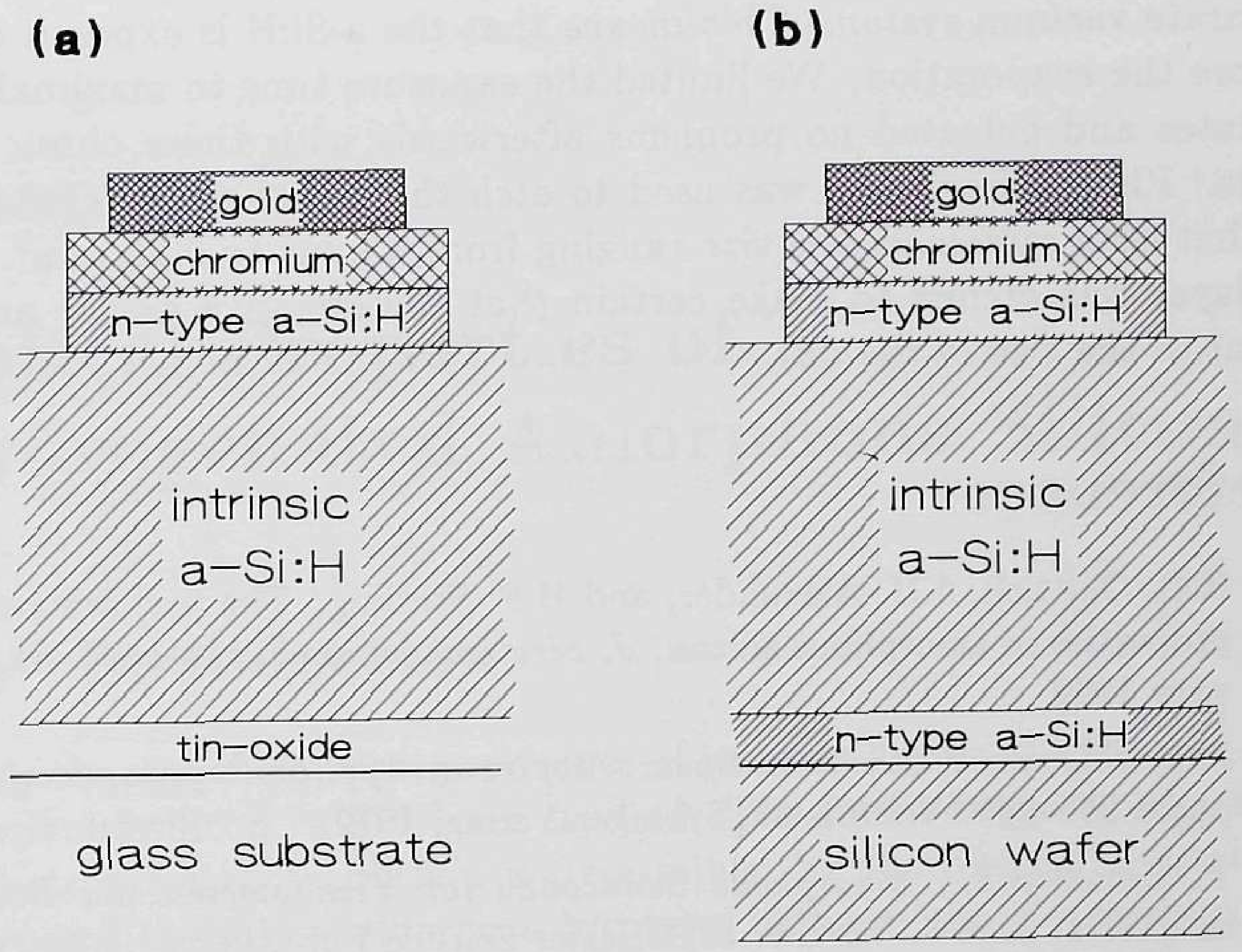

Figure 2.3: The device structures discussed in chapters 4 and 5; (a) is the i-n structure of chapter 4, and (b) is the n-i-n structure of chapter 5.

Table 2.1: Deposition conditions for the i- and n-layer.

material	gas	temperature °C	pressure torr.	flow rate sccm	rf power W/cm^2	growth rate Å/s
intrinsic	SiH_4	250	0.3	50	36	5
	H_2			50		
n-type	SiH_4	250	0.3	99	16	1
	PH_3			1		

The metal on top of the a-Si:H is deposited by evaporation in a separate vacuum system. This means that the a-Si:H is exposed to air before the evaporation. We limited the exposure time to maximally 15 minutes and detected no problems afterwards with these ohmic contacts. Photolithography was used to etch the metal and the n^+-layer so that dots remained of a size ranging from 2 mm^2 to 0.25 mm^2. The n^+-layer was etched to make certain that the effective device area is equal to the size of the dot.

References

[1] R.C. Chittick, J.H. Alexander, and H.F. Sterling. The preparation and properties of amorphous silicon. *J. Electrochem. Soc.*, 116(1):77–81, January 1969.

[2] P.G. LeComber and W.E. Spear. *Topics in Applied Physics*, chapter 9, pages 251–285. Volume 36, Springer-Verlag, 1979.

[3] Y. Hamakawa. *Amorphous Semiconductor Technologies and Devices*, chapter 1, page 5. Volume 16, Elsevier Science Publishers, 1984.

[4] S. Guha. Advances in high-efficiency, multiple-gap, multi-junction amorphous silicon-based alloy thin-film solar cells. In *Amorphous Silicon Technology*, Materials Research Society, 1989.

[5] R.C. van Oort. *Hydrogenated Amorphous and Microcrystalline Silicon Deposited from Silane-Hydrogen Mixtures.* PhD thesis, Delft University of Technology, 1989.

[6] G.H. Bauer, C.E. Nebel, and G. Schumm. Band tailing and transport in a-SiGe:H-alloys. In *Amorphous Silicon Technology*, Materials Research Society, 1989.

[7] E.H. Rhoderick. *Metal-Semiconductor Contacts.* Clarendon Press, Oxford, 1980.

Chapter 3

Optical Properties of Hydrogenated Amorphous Silicon

3.1 Introduction

In this chapter the optical properties of intrinsic layers of hydrogenated amorphous silicon (a-Si:H) are studied. The linear response of a solid to electromagnetic radiation is determined by the dielectric constant. In general there is a difference in phase between the electromagnetic radiation and the linear response, and the dielectric constant is a complex number, i.e., $\tilde{\varepsilon} = \varepsilon_1 - i\varepsilon_2$. The refractive index and the extinction coefficient are related to $\tilde{\varepsilon}$ by $\varepsilon_1 = n^2 - k^2$ and $\varepsilon_2 = 2nk$.

The optical properties of a-Si:H are described by the refractive index n and the extinction coefficient k. These n and k are called the optical constants, although they depend on the wavelength. The absorption coefficient α and the optical gap E_g (related to the bandgap) are obtained from the extinction coefficient. Reflection (R) and transmission (T) measurements were used to obtain the refractive index and the extinction coefficient of the i-layers. The analysis of the R and T measurements is described in section 3.2.

In section 3.3 two models that are used to analyze the optical properties of a-Si:H are described. The first model uses a description analogous to the band theory of a crystalline semiconductor. This model is used to obtain the optical gap from the extinction coefficient. The second model is based on the oscillator approximation. In this model the optical properties of a-Si:H are approximated by the optical properties of a system of harmonic oscillators. This second model is used to describe the dependency of the refractive index and the optical gap on the hydrogen concentration in the layer.

We studied the optical properties of intrinsic a-Si:H deposited from silane-hydrogen mixtures and various rf powers. The silane-hydrogen mixtures and the rf powers we investigated are close to the optimum conditions for devices, e.g., solar cells. In this chapter the relation between structure and optical properties of the i-layers will be discussed. In particular the role of hydrogen in the layers will be investigated.

The refractive index and the optical gap of a-Si:H depend on the hydrogen concentration in the a-Si:H layer. In section 3.5 we introduce a model for the incorporation of hydrogen in the a-Si:H network. This model for the incorporation of hydrogen is used in section 3.5 with the concept of bond polarizabilities to calculate the refractive index as a function of the hydrogen concentration in the layer. The experimental and calculated refractive index as a function of the hydrogen concentration show a reasonable correspondence.

The optical gap as a function of the hydrogen concentration in the a-Si:H layer is discussed in section 3.6. The oscillator model is used with the model for the incorporation of hydrogen to calculate the optical gap as a function of the hydrogen concentration. The calculated relation between the optical gap and the hydrogen concentration corresponds with the experimental relations as found by other research groups.

In section 3.7 the inhomogeneity of microcrystalline silicon (μc-Si:H) is studied. We present a simple optical method to study this inhomogeneity. With this method it is found that the first 200 Å of a 5000 Å thick μc-Si:H layer is amorphous. This amorphous interfacial layer is harmful to the efficiency of a solar cell that uses a μc-Si:H layer as a p^+ window layer.

3.2 Analysis of Reflection and Transmission Measurements

In this section the method to obtain the refractive index n and the extinction coefficient k from the reflection R and the transmission T is described. The basic principle of this method can be divided into a simulation part and an optimization part. By simulation is meant the calculation of R and T for a given n and k. By optimization is

meant the adjustment of n and k until the best correspondence of the calculated R and T with the measured R and T is obtained.

3.2.1 Simulation

If light passes the boundary between two media with different refractive indices, then some energy will be transmitted and some energy will be reflected. The reflection R and the transmission T are defined by

$$T = \frac{\text{Transmitted energy}}{\text{Incident energy}} \quad \text{and} \quad R = \frac{\text{Reflected energy}}{\text{Incident energy}}. \qquad (3.1)$$

The reflection and transmission depend on the refractive indices of the two media, on the angle between the direction of the light and the boundary, and on the polarization state of the light. In normal incidence, the reflection and transmission depend only on the refractive indices of the two media. In the remainder of this chapter we will only consider the case of normal incidence.

The reflection and transmission coefficients are defined by the following formulas using the amplitude of the light. The reflection coefficient r and transmission coefficient t are given by

$$r = \frac{\text{amplitude of reflected light}}{\text{amplitude of incident light}} = \frac{n_0 - n_1}{n_0 + n_1} \qquad (3.2)$$

and

$$t = \frac{\text{amplitude of transmitted light}}{\text{amplitude of incident light}} = \frac{2n_0}{n_0 + n_1}, \qquad (3.3)$$

where n_0 is the refractive index of the first medium and n_1 is the refractive index of the second medium. These r and t are called the Fresnel coefficients. The reflection and transmission can be expressed in r and t by

$$R = r^2 = \frac{(n_0 - n_1)^2}{(n_0 + n_1)^2} \quad \text{and} \quad T = \frac{n_1}{n_0} t^2 = \frac{4n_0 n_1}{(n_0 + n_1)^2}. \qquad (3.4)$$

It is easy to verify that $R + T = 1$.

The calculation of R and T is described in appendix A. In the appendix the following optical systems are treated:

- A single non-absorbing layer, coherent or incoherent.
- A single absorbing layer.
- A thin film (coherent) on a substrate (incoherent).
- The method to obtain R and T for a large number of layers.

The refractive index n and the extinction coefficient k are obtained from the measured R and T by fitting the calculated R and T to the measured R and T. The fitting procedure is described in the next subsection.

3.2.2 Optimization

The method to obtain the refractive index (n), the extinction coefficient (k), and the layer thickness (d) of the a-Si:H film from R and T measurements will be described in this subsection. The method is based on the optimization of n, k, and d until the best correspondence of the calculated R and T with the measured R and T is obtained. This subsection is divided in the optimization of d, the optimization of k, and the optimization of n. The outline for the remainder of this subsection is

- Determination of the layer thickness.
- Determination of the extinction coefficient as a function of the wavelength.
- Determination of the refractive index as a function of the wavelength.

The layer thickness

The layer thickness of an a-Si:H film can be obtained from the distance between the minima and maxima in the reflection which are caused by interference. A typical measured reflection signal is shown in figure 3.1. These extrema in the reflection occur when the double layer thickness is an integer multiple of the half wavelength in the layer (λ/n_1) and the absorption of the layer is negligible

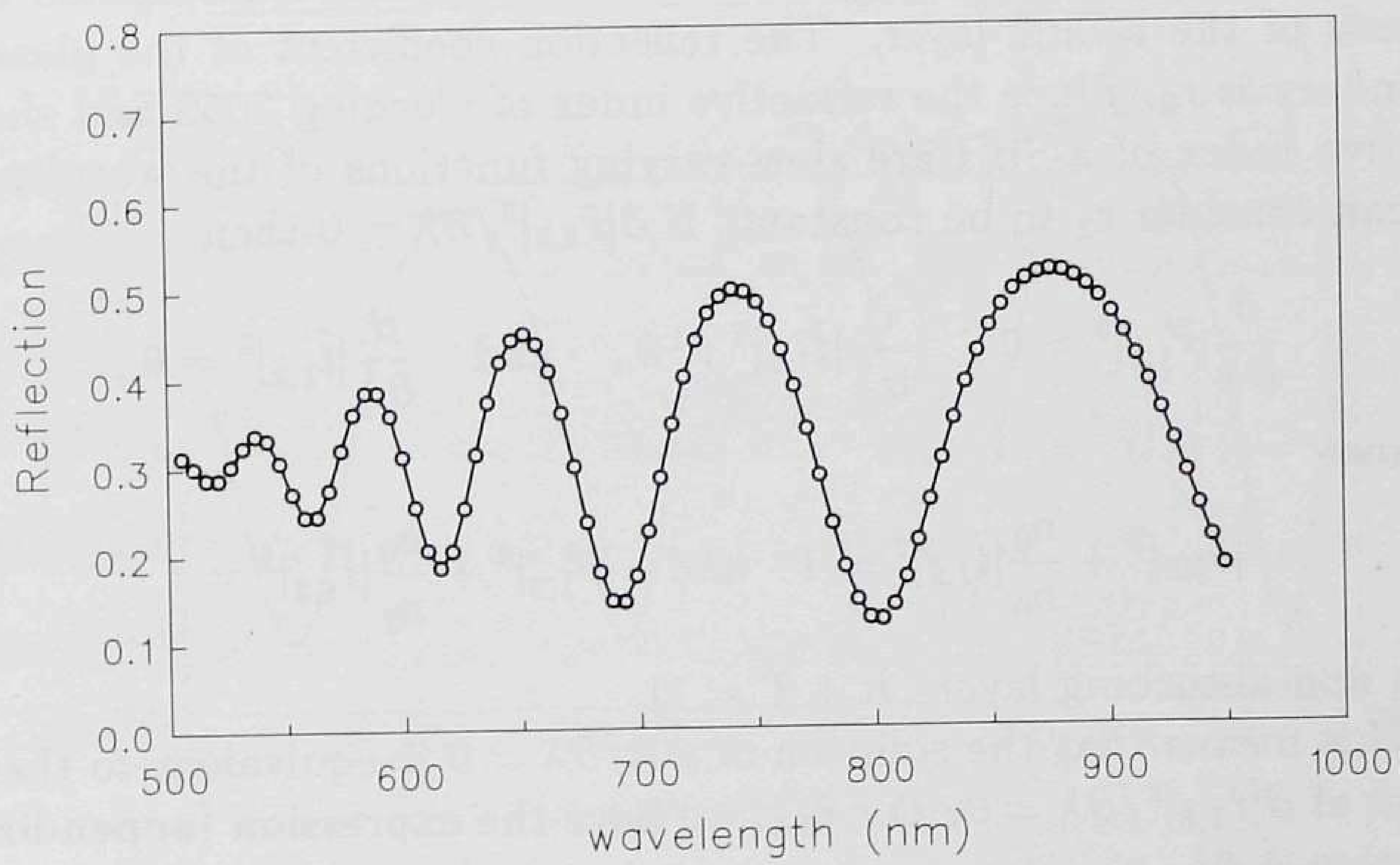

Figure 3.1: The reflection of an a-Si:H film on a Corning 7059 substrate.

$$\tfrac{1}{2}\mathrm{k_o}\lambda = 2n_1 d_1\,, \qquad \text{where} \qquad \mathrm{k_o} = 1,\,2,\,3,\,\ldots . \tag{3.5}$$

In the above equation is λ the wavelength in vacuum, n_1 the refractive index of the a-Si:H layer, and d_1 in the layer thickness. The indices refer to the notation used by Heavens [1], where the layers and interfaces are numbered from 1 to N starting at the top layer (see the illustration in appendix A). For a-Si:H films on a glass substrate the maxima in the reflection occur for $\mathrm{k_o}$ is odd, because $n_{\mathrm{air}} < n_{\mathrm{a-Si:H}}$ and $n_{\mathrm{glass}} < n_{\mathrm{a-Si:H}}$. Equation 3.5 is only valid for a non-absorbing layer. Because the absorption of a-Si:H is negligible at long wavelengths, equation 3.5 can be used (at long wavelengths).

Equation 3.5 is obtained by differentiating the reflection as a function of the wavelength and by solving $\partial R/\partial\lambda = 0$. For a coherent non-absorbing layer (a-Si:H film) on an incoherent non-absorbing substrate (Corning 7059) the reflection is given by (appendix A, equation A.20)

$$R = |\tilde{r}_{1,2}|^2 + \frac{|\tilde{t}_{1,2}|^2\,|\tilde{t}'_{1,2}|^2\,|r_3|^2}{1 - |r_3|^2\,|\tilde{r}'_{1,2}|^2}\,, \tag{3.6}$$

where $\tilde{r}_{1,2}$, $\tilde{r}'_{1,2}$, $\tilde{t}_{1,2}$, and $\tilde{t}'_{1,2}$ are the reflection and transmission coefficients of the a-Si:H layer. The reflection coefficient of the glass/air boundary is r_3. Since the refractive index of Corning 7059 and the refractive index of a-Si:H are slow varying functions of the wavelength, we can consider r_3 to be constant. If $\partial|\tilde{r}_{1,2}|^2/\partial\lambda = 0$ then

$$\frac{\partial}{\partial\lambda}|\tilde{r}'_{1,2}|^2 = 0\,, \quad \frac{\partial}{\partial\lambda}|\tilde{t}_{1,2}|^2 = 0\,, \quad \text{and} \quad \frac{\partial}{\partial\lambda}|\tilde{t}'_{1,2}|^2 = 0\,,$$

because

$$|\tilde{r}_{1,2}|^2 + \frac{n_2}{n_0}|\tilde{t}_{1,2}|^2 = 1 \quad \text{and} \quad |\tilde{r}'_{1,2}|^2 + \frac{n_0}{n_2}|\tilde{t}'_{1,2}|^2 = 1$$

for a non-absorbing layer ($R + T = 1$).

This means that the solution of $\partial R/\partial\lambda = 0$ is equivalent to the solution of $\partial|\tilde{r}_{1,2}|^2/\partial\lambda = 0$. For $\tilde{r}_{1,2}$, we have the expression (appendix A, equation A.6)

$$\tilde{r}_{1,2} = \frac{r_1 + r_2\,e^{-2i\delta_1}}{1 + r_2 r_1\,e^{-2i\delta_1}}\,, \tag{3.7}$$

where r_1 and r_2 are the reflection coefficients of the air/a-Si:H and the a-Si:H/glass boundary, respectively. The phase shift δ_1 is the shift in phase of the light wave when it travels from the top to the end of the layer, and $\delta_1 = (2\pi/\lambda)n_1 d_1$. The derivative of $|\tilde{r}_{1,2}|^2$ is

$$\frac{\partial}{\partial\lambda}|\tilde{r}_{1,2}|^2 = 2r_1 r_2 \sin 2\delta_1 \frac{(1-r_1^2)(r_2^2-1)}{(1+2r_1r_2\cos 2\delta_1 + r_2^2 r_1^2)^2}\,\frac{\partial 2\delta_1}{\partial\lambda}\,. \tag{3.8}$$

The solution of $\partial|\tilde{r}_{1,2}|^2/\partial\lambda = 0$ is

$$\sin 2\delta_1 = 0 \Longrightarrow \delta_1 = \frac{2\pi}{\lambda}n_1 d_1 = \tfrac{1}{2}\mathrm{k_o}\pi\,, \quad \text{where} \quad \mathrm{k_o} = 1,\,2,\,3,\,\ldots, \tag{3.9}$$

and is equal to equation 3.5.

Before the layer thickness can be obtained from the position of the reflection maxima with equation 3.5, the refractive index of the layer has to be obtained. The refractive index can be obtained from the height of the reflection maxima. This is done by solving the following equation with Newton's iteration

$$R_{\mathrm{meas}} - R_{\mathrm{calc}} = 0\,, \tag{3.10}$$

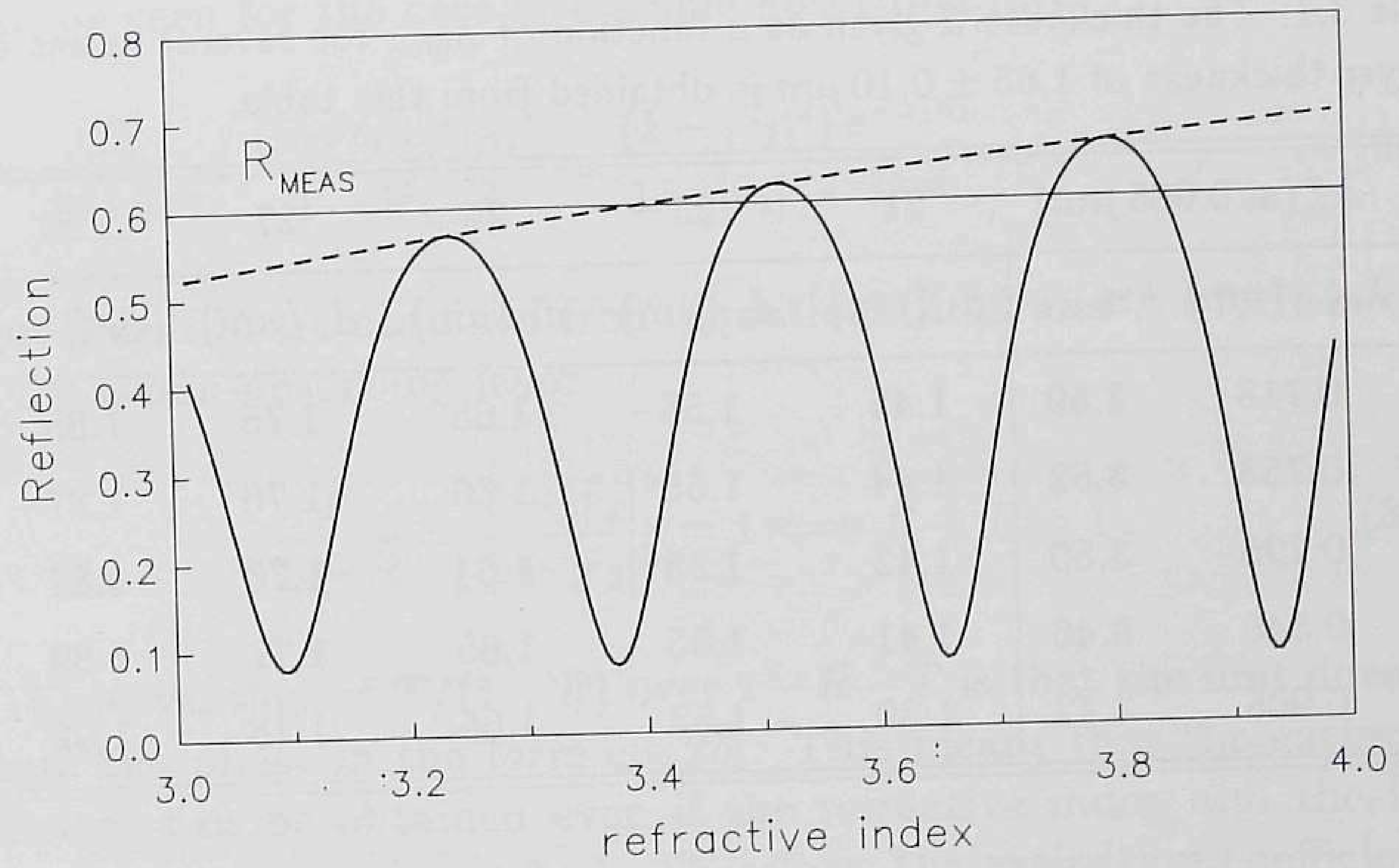

Figure 3.2: The calculated reflection as a function of the refractive index. The solid line is the reflection with a constant layer thickness, and the dashed line is the reflection with an adjusted layer thickness so that nd = constant. The horizontal line is used as an illustration of a measured reflection.

with

$$n_1 d_1 = \text{constant}\,. \tag{3.11}$$

R_{meas} is the measured reflection and R_{calc} is the calculated reflection. Because R_{calc} is an oscillating function of n_1, the condition $n_1 d_1$ = constant is used. This condition is necessary to obtain a unique solution as can be seen in figure 3.2.

The layer thickness can be obtained from the wavelengths at the reflection maxima (λ_{max}), and the refractive indices at these wavelengths (n_{max}). The layer thickness d_1 as a function of λ_{max}, n_{max}, and $\mathrm{k_o}$ is given by

$$d_1 = \frac{\mathrm{k_o}\lambda_{\mathrm{max}}}{4n_{\mathrm{max}}}\,, \qquad \text{where} \qquad \mathrm{k_o} = 1,\,3,\,5,\,\ldots. \tag{3.12}$$

The layer thickness d_1 can be obtained from equation 3.12, if the order $\mathrm{k_o}$ is known. This order cannot be obtained directly. We use the fact that d_1 is not constant but a function of λ_{max} when $\mathrm{k_o}$ is incorrect. This is illustrated in table 3.1 for an a-Si:H layer on a Corning 7059

Table 3.1: The thickness d given as a function of $\lambda_{\max}$ for several values of k_o. A layer thickness of $1.65 \pm 0.10\,\mu$m is obtained from this table.

k_o (at 0.905 μm)		21	23	25	27	29
$\lambda_{\max}$ (μm)	$n_{\max}$	d_1 (μm)	d_1 (μm)	d_1 (μm)	d_1 (μm)	d_1 (μm)
0.718	3.59	1.45	1.55	1.65	1.75	1.85
0.753	3.52	1.44	1.55	1.66	1.76	1.87
0.795	3.50	1.42	1.53	1.64	1.76	1.87
0.845	3.46	1.41	1.53	1.65	1.77	1.89
0.905	3.42	1.39	1.52	1.65	1.78	1.92

glass substrate. In this table the thickness d_1 is given as a function of $\lambda_{\max}$ for several values of k_o, and a layer thickness of $1.65 \pm 0.10\,\mu$m is obtained.

The extinction coefficient

The extinction coefficient k_1 is obtained from the absorption coefficient α_1

$$k_1 = \frac{\lambda \alpha_1}{4\pi}\,. \tag{3.13}$$

Naturally, the layer thickness has to be known before the absorption coefficient can be obtained from the R and T measurements. Therefore, the absorption (or extinction) coefficient is optimized after the layer thickness is obtained. The values of $n_{\max}$ of the layer thickness optimization are used for the refractive index.

The absorption coefficient is obtained by solving the following equation with Newton's iteration

$$\frac{T_{\text{meas}}}{1 - R_{\text{meas}}} - \frac{T_{\text{calc}}}{1 - R_{\text{calc}}} = 0\,. \tag{3.14}$$

The expression $T/(1-R)$ is closely related to the absorption coefficient, as can be seen for the case of a single absorbing layer

$$\frac{T}{1-R} = \frac{(n_2/n_0)\,|\tilde{t}_{1,2}|^2}{1 - |\tilde{r}_{1,2}|^2} \approx \frac{(1 - |\tilde{r}_2|^2)\, e^{-\alpha_1 d_1}}{1 - |\tilde{r}_2|^2\, e^{-2\alpha_1 d_1}} \approx e^{-\alpha_1 d_1}\,, \tag{3.15}$$

where R and T are obtained from equations A.16 and A.17. It is clear that for a non-absorbing layer

$$\frac{T}{1-R} = \frac{1 - |\tilde{r}_2|^2}{1 - |\tilde{r}_2|^2} = 1 \Longleftrightarrow R + T = 1\,. \tag{3.16}$$

The advantage of $T/(1-R)$ over $1 - R - T$ is that the first does not contain the phase in the form $\cos 2\delta_1$. This means that the extinction coefficient can be obtained even if the refractive index and the layer thickness are not well matched. Therefore, the extinction coefficient is optimized before the refractive index.

The refractive index

A problem with the optimization of the refractive index is the oscillating character of R and T as a function of n. For the optimization of the layer thickness, this problem was solved by adjusting n and d at the same time so that nd = constant. The constant was known since the maximum reflection points were used. The refractive indices between these maximum reflection points have to be obtained in another way since nd is not known.

We used the following method to obtain the refractive index. The refractive index is described by the function $n(\lambda) = a/\lambda^2 + b/\lambda + c$, and the parameters of this function $(a,\, b,\, c)$ are optimized. This optimization means that the following error function is minimized:

$$\text{err}(a,b,c) = \sum_{\text{datapoints}} \left(R_{\text{meas}} - R_{\text{calc}}(a,b,c)\right)^2 \tag{3.17}$$

The layer thickness is again adjusted so that $n_{\max} d$ = constant at the reflection maximum at the longest wavelength. The error function is minimized with the Gauss-Newton method [2].

3.3 Models for the Optical Properties

The linear response of a solid to electromagnetic radiation of angular frequency ω is determined by the complex dielectric constant as a function of frequency

$$\tilde{\varepsilon}(\omega) = \varepsilon_1(\omega) - i\varepsilon_2(\omega)\,. \tag{3.18}$$

The refractive index n and the extinction coefficient k that are obtained from the reflection and transmission measurements can be used to obtain $\tilde{\varepsilon}(\omega)$

$$\varepsilon_1(\omega) = n^2 - k^2\,, \tag{3.19}$$

$$\varepsilon_2(\omega) = 2nk\,. \tag{3.20}$$

The absorption coefficient is given by

$$\alpha(\omega) = \frac{4\pi}{\lambda}k = \frac{\omega}{nc}\varepsilon_2(\omega)\,, \tag{3.21}$$

where c is the speed of light in vacuum.

In the research field of the optical properties of crystals the attention is focused on the imaginary part of the dielectric constant $\varepsilon_2(\omega)$. This $\varepsilon_2(\omega)$ gives information about the density of states, since $\varepsilon_2(\omega)$ is related to the transition of electrons from the valence band to the conduction band. The Kramers-Kronig relations can be used to obtain $\varepsilon_1(\omega)$ from $\varepsilon_2(\omega)$ [3,4]. In a crystal $\varepsilon_2(\omega)$ can be obtained from the following expression [5]

$$\varepsilon_2(\omega) = \left(\frac{2\pi q}{m\omega}\right)^2 \frac{1}{3} P_{\mathrm{cr}}^2(\omega) J_{vc}(\omega)\,, \tag{3.22}$$

where $P_{\mathrm{cr}}(\omega)$ is the momentum matrix element for the transition between the valence band and the conduction band, and $J_{vc}(\omega)$ is the joint density of states that is obtained by a surface integral in $\vec{k}$-space. $J_{vc}(\omega)$ represents the number of states in the valence band and the conduction band which can undergo energy and $\vec{k}$-conserving transitions for the photon frequency ω.

For a-Si:H equation 3.22 is no longer valid. Through the loss of translational symmetry in a-Si:H, the wave vector $\vec{k}$ is no longer a good quantum number that needs to be conserved in an optical transition. Instead, an expression analogous to equation 3.22 is used [6,7,8]

$$\varepsilon_2(\omega) = \left(\frac{2\pi q}{m\omega}\right)^2 P_{\mathrm{am}}^2(\omega) \int N_v(E) N_c(E + \hbar\omega)\, dE \tag{3.23}$$

in which the joint density of states $J_{vc}(\omega)$ of the crystalline material has been replaced by a simple convolution of occupied valence and empty conduction density of states $N_v(E)$ and $N_c(E)$, respectively. Equation 3.23 is what one intuitively expects for transitions that are subject only to energy conservation, but no longer to $\vec{k}$ conservation.

Tauc [6] used the approximation that the momentum matrix elements $P_{\mathrm{am}}(\omega)$ are constant for transitions between delocalized states in the valence and conduction band, and he used the approximation that the valence and conduction band are parabolic. This gives for $\varepsilon_2(\omega)$:

$$\varepsilon_2(\omega) \propto \frac{P^2}{\omega^2} \times (\hbar\omega - E_g)^2 \tag{3.24}$$

for

$$N_v \propto \sqrt{E_v - E} \quad \text{and} \quad N_c \propto \sqrt{E - E_c} \tag{3.25}$$

with

$$E_g = E_c - E_v\,. \tag{3.26}$$

If the absorption coefficient $\alpha(\omega)$ is substituted for $\varepsilon_2(\omega)$ we obtain

$$\sqrt{\alpha(\omega)n(\omega)\omega} = \text{constant}\,(\hbar\omega - E_g)\,, \tag{3.27}$$

because $n(\omega)$ varies slowly with ω the following equation is used by experimentalists [9,10]

$$\sqrt{\alpha(\omega)\hbar\omega} = B(\hbar\omega - E_g)\,. \tag{3.28}$$

Equation 3.28 is used to obtain the so-called optical gap E_g of a-Si:H. This gap is also called the Tauc gap to distinquish it from other methods that give an optical gap. These other methods take a linear distribution for the valence band and conduction band, or the assumption of constant matrix elements is made for the matrix elements of the dipole operator instead of the momentum operator [11,12]. In this chapter we will use only the Tauc gap to analyze our data.

Another model for the optical properties is based on the single oscillator approximation. In this model the dielectric response of a solid is approximated by the response of a number of oscillators of the same type. The polarizability of the harmonic oscillator is [13]

$$\tilde{\alpha}_p = \frac{q^2}{m(\omega_0^2 - \omega^2 + i\gamma\omega)}, \tag{3.29}$$

where ω_0 is the natural frequency of the oscillator, m is the mass of the electron, and γ is the damping factor.

The dielectric constant is obtained from the polarizability with the Clausius-Mossotti relation

$$\frac{\tilde{\varepsilon} - 1}{\tilde{\varepsilon} + 2} = \frac{4\pi}{3} N_{os} \tilde{\alpha}_p, \tag{3.30}$$

where N_{os} is the number of oscillators per unit volume. The dielectric constant is not proportional to the sum of the polarizabilities because of the local field correction [14]. The electric field that is "felt" by the oscillator is not the applied field, because of the other oscillators. The surrounding oscillators modify the applied field, and this results in a different electric field at the place of the oscillator, which is called the local field. The dielectric constant is expressed by

$$\tilde{\varepsilon} = 1 + \frac{\omega_p^2}{\omega_1^2 - \omega^2 + i\gamma\omega}, \tag{3.31}$$

where

$$\omega_1^2 = \omega_0^2 - \frac{4\pi N_{os} q^2}{3m} \quad \text{and} \quad \omega_p^2 = 4\pi N_{os} \frac{q^2}{m}. \tag{3.32}$$

The replacement of ω_0^2 by ω_1^2 is the consequence of the local field correction [15].

Although equation 3.31 does not accurately describe the data, it can be used to determine ω_1 and ω_p, quantities that have physical significance. The plasma frequency ω_p is used to obtain the Penn gap $\hbar\omega_g$ using [16]

$$n_\infty^2 = 1 + \frac{2}{3}\frac{\omega_p^2}{\omega_g^2}, \tag{3.33}$$

where n_∞ is the low energy refractive index. The Penn gap is based on a simple two-band model for an isotropic semiconductor with a spherical Brillouin zone [17,18]. The Penn gap $\hbar\omega_g$ represents an average separation between valence and conduction bands and is a measure of the covalent bond strength [19,20].

3.4 Experiment

3.4.1 Deposition of the Films

In this chapter the optical properties of intrinsic films are studied. These films were made by means of the rf glow discharge process as described in chapter 2. The deposition conditions for the films were the same as the standard conditions in chapter 2, except for the silane/hydrogen ratio in the feed gas and the rf power. The rf power was varied between 15 and 482 mW/cm^2, and the silane (SiH_4) concentration in the feed gas was varied between 2 vol.% and 100 vol.%. A silane concentration of 25 vol.% means a hydrogen flow rate of 75 sccm and a silane flow rate of 25 sccm. The total flow rate was kept constant at 100 sccm.

The amount of hydrogen in the a-Si:H layer is considerable, namely between 5 and 25 atomic percent [21]. The concentration of hydrogen in the deposited layers was obtained from nuclear reaction analysis (NRA) [22]. These results are correlated with the optical measurements in sections 3.5 and 3.6.

At a low silane/hydrogen ratio and high rf powers microcrystalline silicon (μc-Si:H) is formed [23,24,25]. In section 3.7 these μc-Si:H layers are studied. The μc-Si:H films were grown with a silane/hydrogen ratio of 2 vol.% and an rf power of 310 mW/cm^2. The thickness of the layers was 5000 Å. The films were deposited on Corning 7059 glass for optical measurements. For X-ray diffraction measurements monocrystalline silicon wafers were used as a substrate. It was determined from the X-ray measurements that the average size of the crystallite in the μc-Si:H layer was 100 Å.

Microcrystalline silicon has a lower light absorption than a-Si:H. This means that μc-Si:H is an attractive material for the p$^+$ window layer in a thin film solar cell [26]. The growth of μc-Si:H is inhomo-

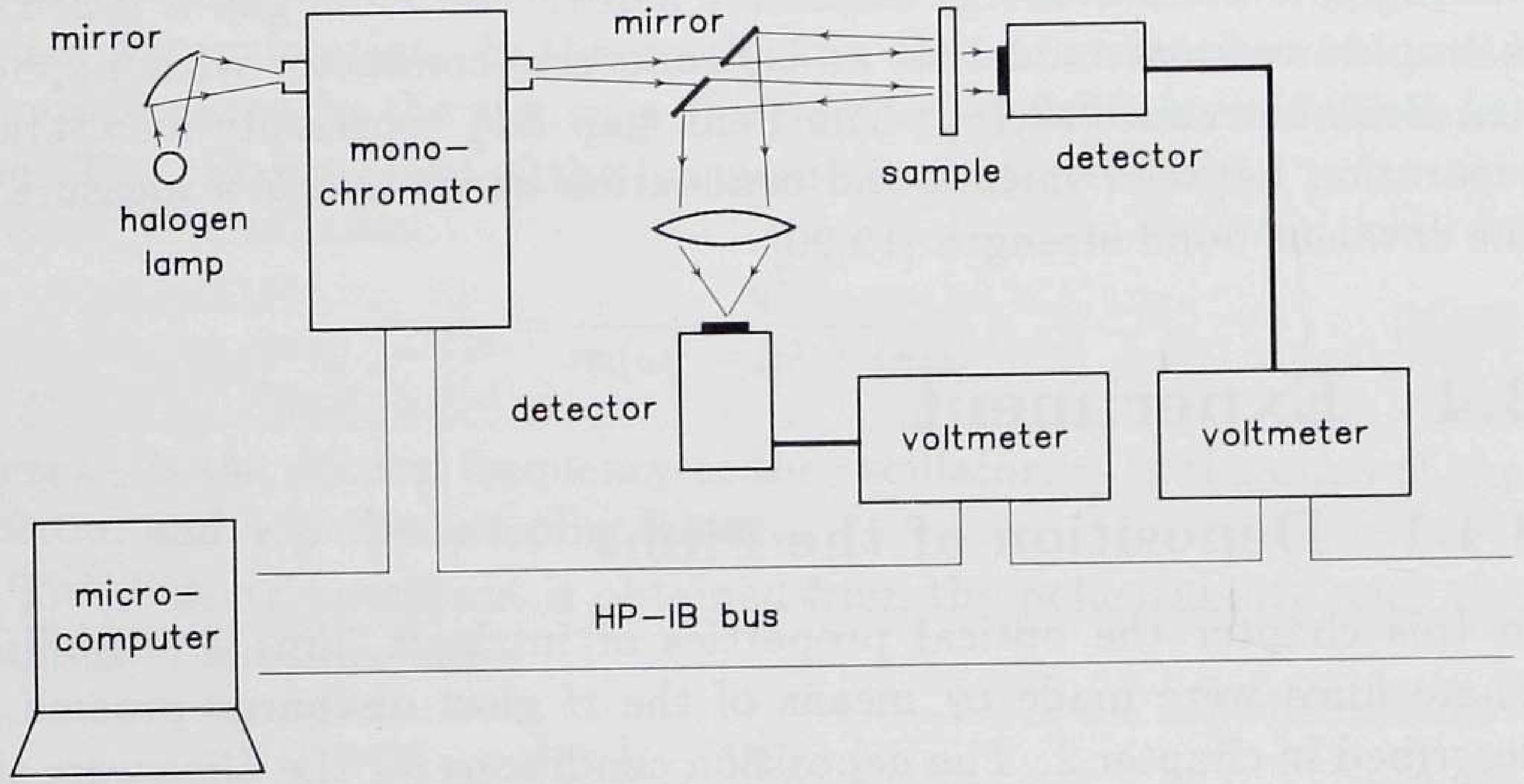

Figure 3.3: Experimental apparatus for the reflection and transmission measurements.

geneous which means that the material near the substrate is different from the material at the top of the layer. This effect, which is harmful to the operation of a solar cell, is studied in section 3.7 using optical measurements [27].

3.4.2 Experimental Setup

The experimental apparatus for the reflection and transmission measurements is schematically depicted in figure 3.3. A 100 W halogen lamp was used as a light source and was focused on the entrance slit of the monochromator (Hilger&Watts). The monochromatic light was connected by a fiber bundle with the reflection and transmission apparatus. This apparatus uses two EG&G HUV silicon photodiodes to measure the reflection and the transmission. The silicon photodiodes can be replaced by two germanium photodiodes (Germanium Power Devices GM-6) to extend the wavelength range to 1.6 μm. The wavelength range for the silicon photodiodes is 0.5 μm–1.0 μm. The wavelength range for the germanium photodiodes is 0.8 μm–1.6 μm. The measurement was controlled by an HP 310 microcomputer. The computer controlled the wavelength and read the voltage from the two HP 3478A voltmeters which are connected with the photodiodes.

We used the following procedure to measure the reflection and transmission of an a-Si:H layer on a Corning 7059 substrate. First a sapphire window was placed in the substrate holder (Melles Griot 02 WSA 008). The refractive index of this sapphire window is tabulated [28], and was used to calculate the reflection and transmission of the sapphire window. This reflection and transmission of the sapphire window was used as a reference. The wavelength was scanned from 0.5 μm to 0.95 μm when the silicon photodiodes were used. The voltage of the two silicon detectors was measured with the two voltmeters and stored in the memory of the computer. This procedure was repeated for the a-Si:H sample. Since the voltage of the silicon detectors is linear with the light intensity and the R and T of the sapphire reference sample is known, the calculation of the R and T of the a-Si:H film and Corning 7059 substrate is straightforward.

3.5 The Refractive Index

In this section the relation between the hydrogen concentration in the layer and the refractive index is studied. The refractive index depends strongly on the deposition conditions as can be seen in figure 3.4, where the refractive index as a function of the rf power is shown. We will analyze the relation between the hydrogen concentration and the refractive index with the model of bond polarizabilities and a model for the incorporation of hydrogen in the layer.

The refractive index at long wavelengths n_∞ can be written in terms of individual oscillators with a polarizability α_p using the Lorentz-Lorenz equation [29,30] (see equation 3.30)

$$\frac{n_\infty^2 - 1}{n_\infty^2 + 2} = \frac{4\pi}{3} N_{os} \alpha_p \,. \tag{3.34}$$

In the case of a-Si:H these oscillators are the Si–Si bond and the Si–H bond. Because the electrons are located in a covalent bond between the atoms, we use the concept of bond polarizability [31]. For an ionic compound the concept of ion polarizability has to be used.

The bond polarizability of the Si–Si bond is obtained from the refractive index of a-Si:H with a low hydrogen content. The refractive

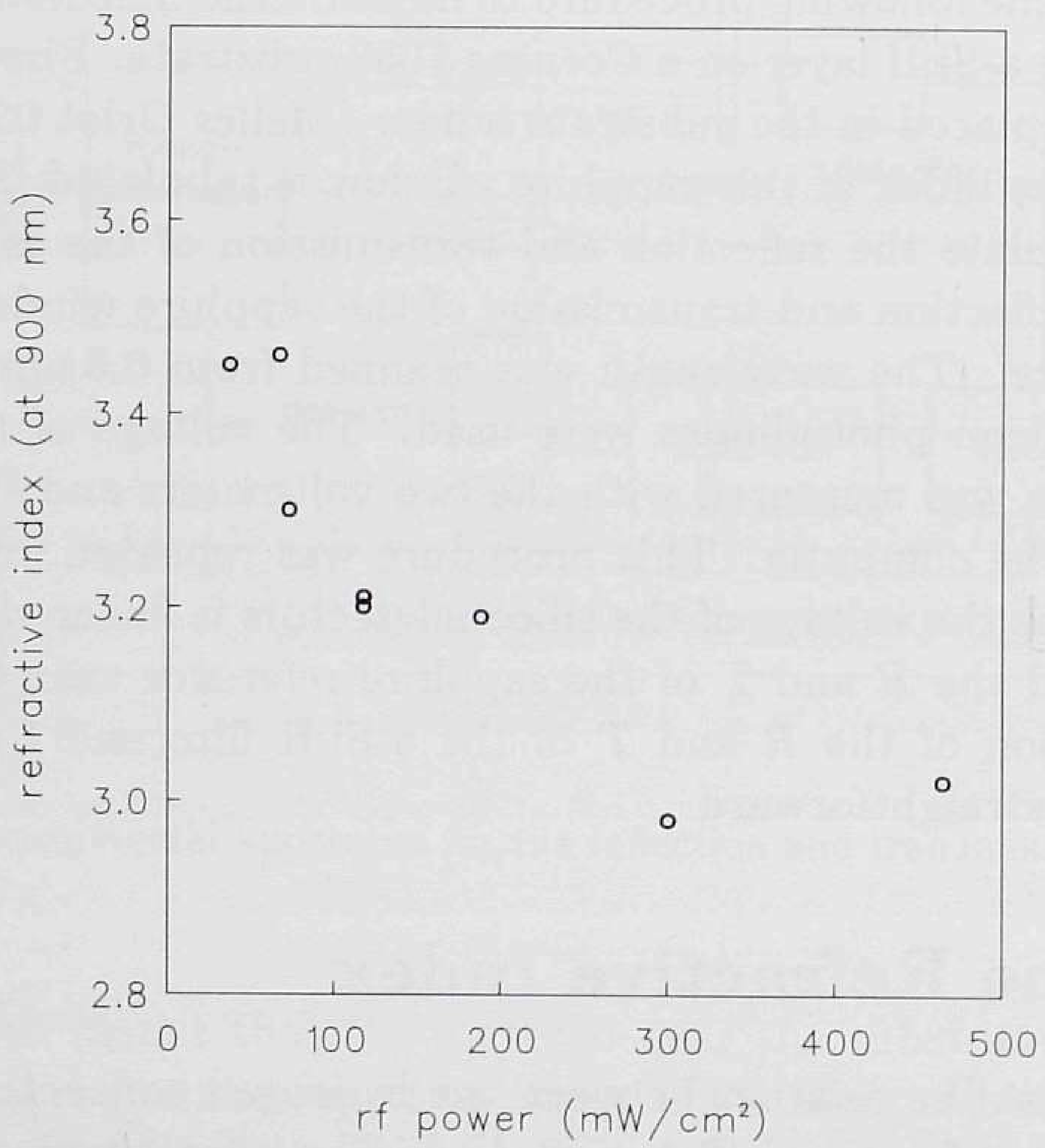

Figure 3.4: The refractive index as a function of the rf power. The feed gas was undiluted silane for all data.

index of a-Si:H with a low hydrogen content is higher than the refractive index of crystalline silicon, because the average bond strength (given by the Penn gap) is smaller for a-Si:H [32,33]. We used a refractive index of 3.6 and an atomic density of 5.0×10^{22} atoms/cm^3 (the density of c-Si) to obtain the polarizability of the Si–Si bond:

$$\alpha_{\text{Si-Si}} = 1.91 \times 10^{-24}\,\text{cm}^3 . \tag{3.35}$$

The bond polarizability of the Si–H bond is taken from the polarizability of the SiH$_4$ molecule which is [34]

$$\alpha_{\text{SiH}_4} = 5.44 \times 10^{-24}\,\text{cm}^3 \implies \alpha_{\text{Si-H}} = 1.36 \times 10^{-24}\,\text{cm}^3 . \tag{3.36}$$

The refractive index is obtained from the Lorentz-Lorenz equation:

$$\frac{n_\infty^2 - 1}{n_\infty^2 + 2} = \tfrac{4\pi}{3}(N_{\text{Si-Si}}\alpha_{\text{Si-Si}} + N_{\text{Si-H}}\alpha_{\text{Si-H}}) , \tag{3.37}$$

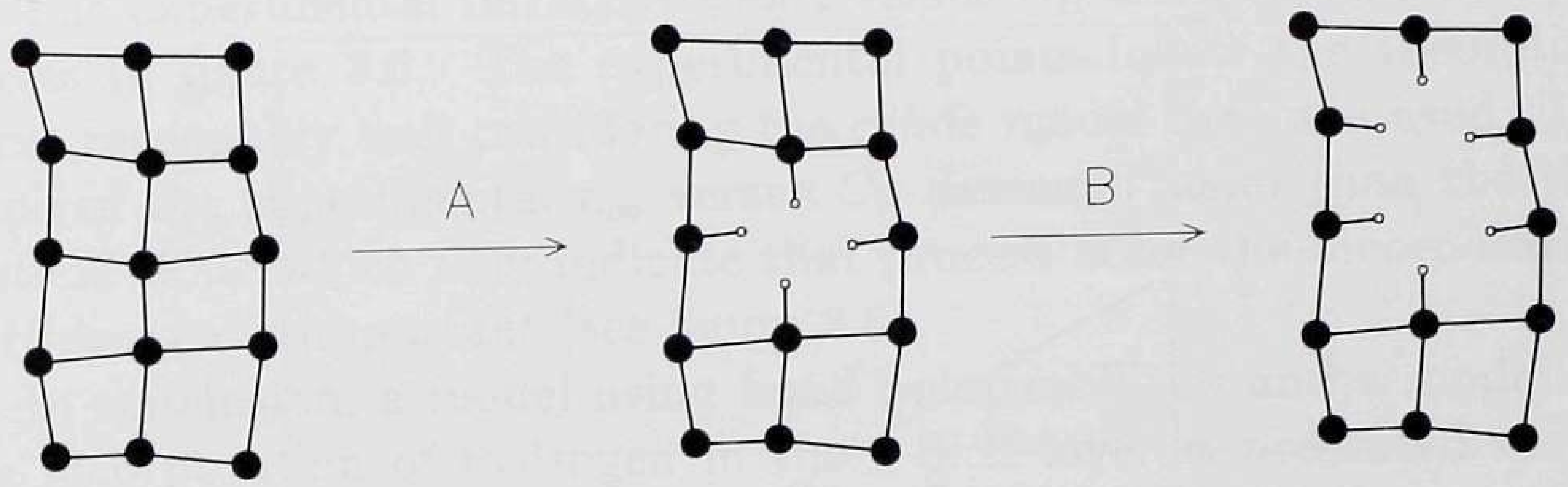

Figure 3.5: The incorporation of hydrogen in the a-Si:H network. The silicon atom is indicated by a large closed circle; the hydrogen atom is indicated by a small open circle.

where $N_{\text{Si-Si}}$ is the number of Si–Si bonds per unit volume and $N_{\text{Si-H}}$ is the number of Si–H bonds per unit volume.

The refractive index depends on the hydrogen content, because Si–Si bonds are broken and replaced by Si–H bonds. We will use the model depicted in figure 3.5 for the incorporation of hydrogen in the a-Si:H network. In figure 3.5 it can be seen that for every hydrogen atom one Si–Si bond is broken and replaced by one Si–H bond (process A). When more hydrogen is added, then two hydrogen atoms can break three Si–Si bonds which are replaced by two Si–H bonds (process B). This means that the total polarizability ($N_{\text{Si-Si}}\alpha_{\text{Si-Si}} + N_{\text{Si-H}}\alpha_{\text{Si-H}}$) decreases faster for process B than for process A.

The refractive index as a function of hydrogen concentration can be calculated with equation 3.37 for process A shown in figure 3.5. The hydrogen concentration in atomic ratio is given by

$$C_{\text{H}} = \frac{N_{\text{H}}}{N_{\text{Si}} + N_{\text{H}}} \implies C_{\text{H}} = \frac{N_{\text{H}}}{N_{\text{c-Si}} + (3/4)N_{\text{H}}} , \tag{3.38}$$

using

$$N_{\text{Si}} = N_{\text{c-Si}} - \tfrac{1}{4}N_{\text{H}} , \tag{3.39}$$

where N_{H} and N_{Si} are the number of hydrogen and silicon atoms per unit volume in the a-Si:H layer, and where $N_{\text{c-Si}}$ is the number of silicon atoms per unit volume in crystalline silicon. The number of hydrogen

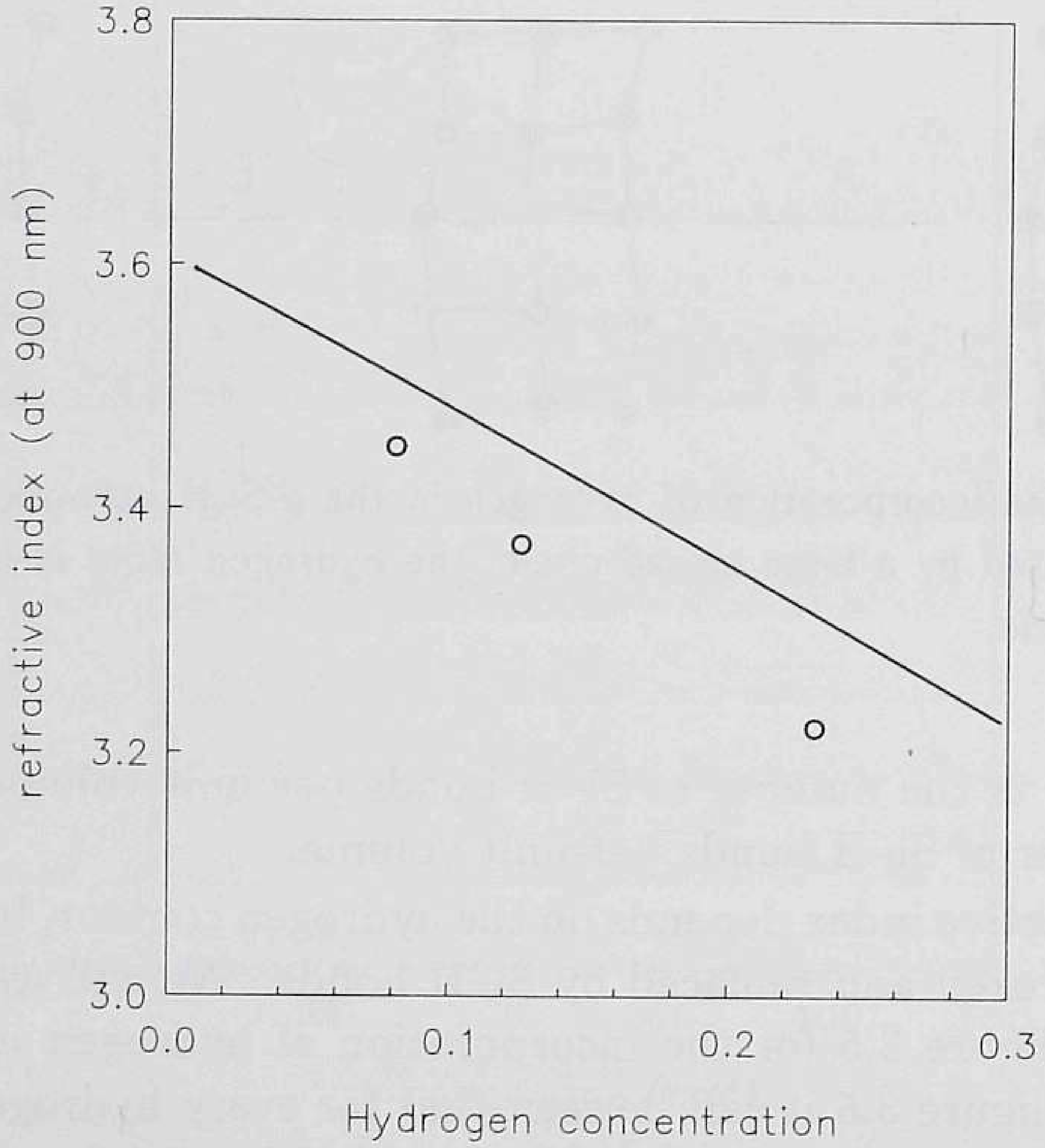

Figure 3.6: The refractive index versus the hydrogen concentration in atomic ratio. The line indicates the theoretical relation, and the circles indicate experimental data.

atoms per unit volume as a function of the hydrogen concentration is

$$N_{\mathrm{H}} = \frac{C_{\mathrm{H}} N_{\text{c-Si}}}{1-(3/4)C_{\mathrm{H}}} \approx N_{\text{c-Si}}(C_{\mathrm{H}} + \tfrac{3}{4}C_{\mathrm{H}}^2)\,. \tag{3.40}$$

The number of bonds per unit volume is given by

$$N_{\text{Si-Si}} = 2N_{\text{c-Si}} - N_{\mathrm{H}} \approx N_{\text{c-Si}}(2 - C_{\mathrm{H}} - \tfrac{3}{4}C_{\mathrm{H}}^2) \tag{3.41}$$

and by

$$N_{\text{Si-H}} = N_{\mathrm{H}} \approx N_{\text{c-Si}}(C_{\mathrm{H}} + \tfrac{3}{4}C_{\mathrm{H}}^2)\,. \tag{3.42}$$

The refractive index as a function of the hydrogen concentration can be calculated with equation 3.37, 3.41, and 3.42. The calculated refractive index versus the hydrogen concentration is shown in figure 3.6.

The experimental refractive index versus C_{H} are indicated by open circles in figure 3.6. The experimental points follow the theoretical curve reasonably well considering the crude model that was used. The slope of the experimental n_∞ versus C_{H} descends faster than the theoretical slope which may indicate that process B for the incorporation of hydrogen is important (see figure 3.5).

In conclusion, a model using bond polarizabilities and a model for the incorporation of hydrogen in the a-Si:H layer is presented to explain the relation between the hydrogen concentration in the layer and the refractive index. The experimental refractive index corresponds roughly with the calculated refractive index for hydrogen concentrations between 8 atomic percent and 23 atomic percent hydrogen.

3.6 The Optical Gap

In this section the relation between the hydrogen concentration in the layer and the optical gap is studied. The optical gap is obtained from the absorption coefficient using the Tauc relation

$$\sqrt{\alpha(h\nu)h\nu} = B(h\nu - E_g)\,, \tag{3.43}$$

where $h\nu$ is the photon energy, $\alpha(h\nu)$ is the absorption coefficient, B is a constant, and E_g is the optical gap. The optical gap depends strongly on the deposition conditions as can be seen in figure 3.7, where the optical gap as a function of the rf power is shown. We will analyze the relation between the hydrogen concentration and the optical gap with the model of harmonic oscillators that was presented in section 3.3, and with the model of the incorporation of hydrogen that was presented in section 3.5.

The optical properties of a-Si:H can be described with the oscillator model of section 3.3. The complex dielectric constant is given by

$$\tilde{\varepsilon} = 1 + \frac{\omega_p^2}{\omega_1^2 - \omega^2 + i\gamma\omega}\,, \tag{3.44}$$

where

$$\omega_1^2 = \omega_0^2 - \frac{4\pi N_{\mathrm{os}} q^2}{3m} \quad \text{and} \quad \omega_p^2 = 4\pi N_{\mathrm{os}} \frac{q^2}{m}\,. \tag{3.45}$$

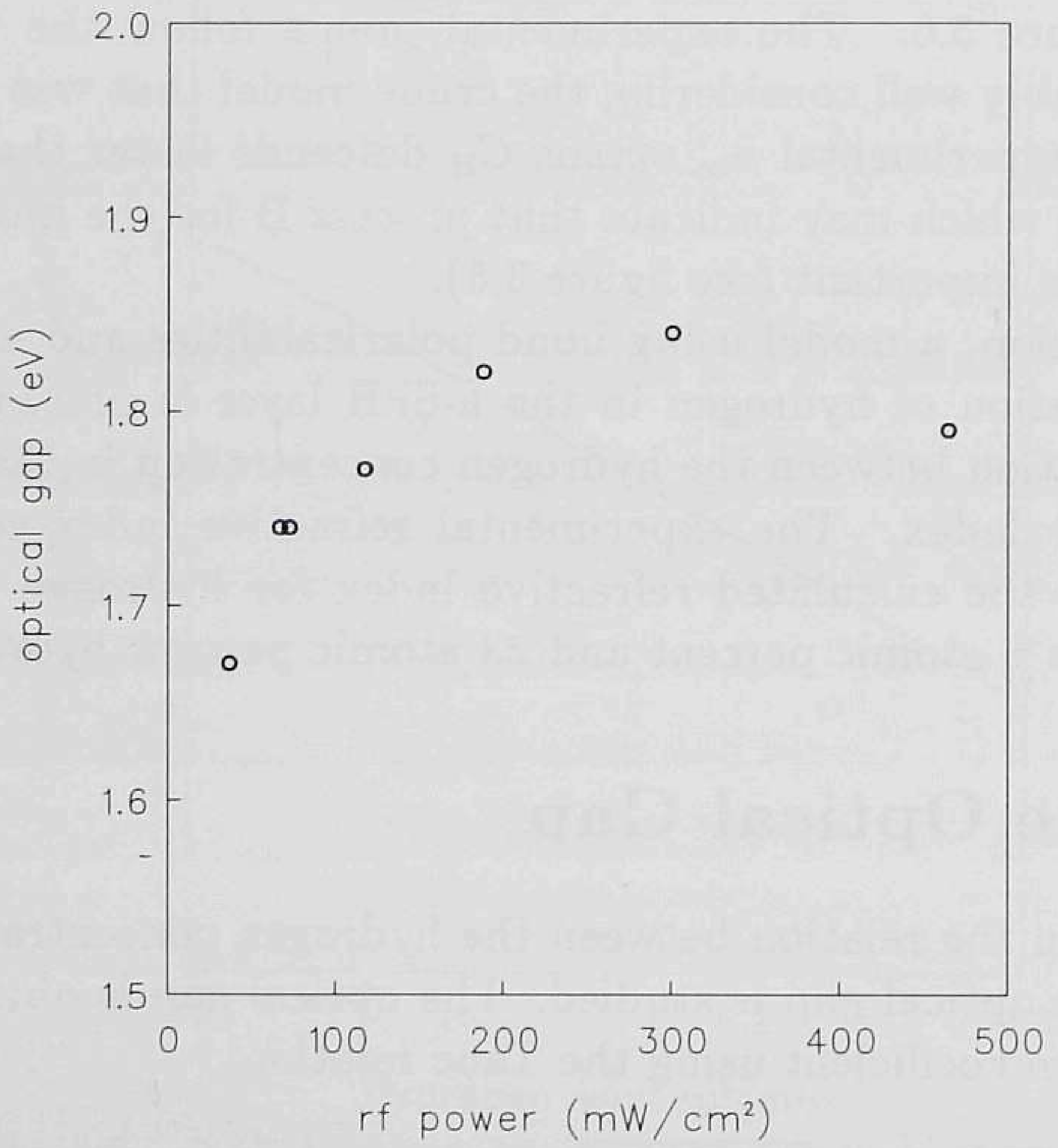

Figure 3.7: The optical gap as a function of the rf power. The feed gas was undiluted silane for all data.

The polarizability of a single oscillator is given by equation 3.29, for low frequencies it is given by

$$\alpha_p = \frac{q^2}{m\omega_0^2}\,. \tag{3.46}$$

The plasma frequency ω_p can be expressed in terms of ω_0 and the refractive index n_∞ using the Lorentz-Lorenz equation and α_p

$$\omega_p^2 = \frac{4\pi}{3} N_{os}\alpha_p \cdot \frac{3q^2}{m\alpha_p} = \frac{n_\infty^2 - 1}{n_\infty^2 + 2} \cdot 3\omega_0^2\,. \tag{3.47}$$

The plasma frequency ω_p increases from $1.48\,\omega_0$ to $1.55\,\omega_0$ if n_∞ increases from 3.0 to 3.6. This is a small relative increase compared to the shift in ω_1 from $0.27\,\omega_0$ to $0.20\,\omega_0$ for the same increase in the refractive index. This means that the shift in ω_1 will dominate the optical properties as a function of the hydrogen concentration.

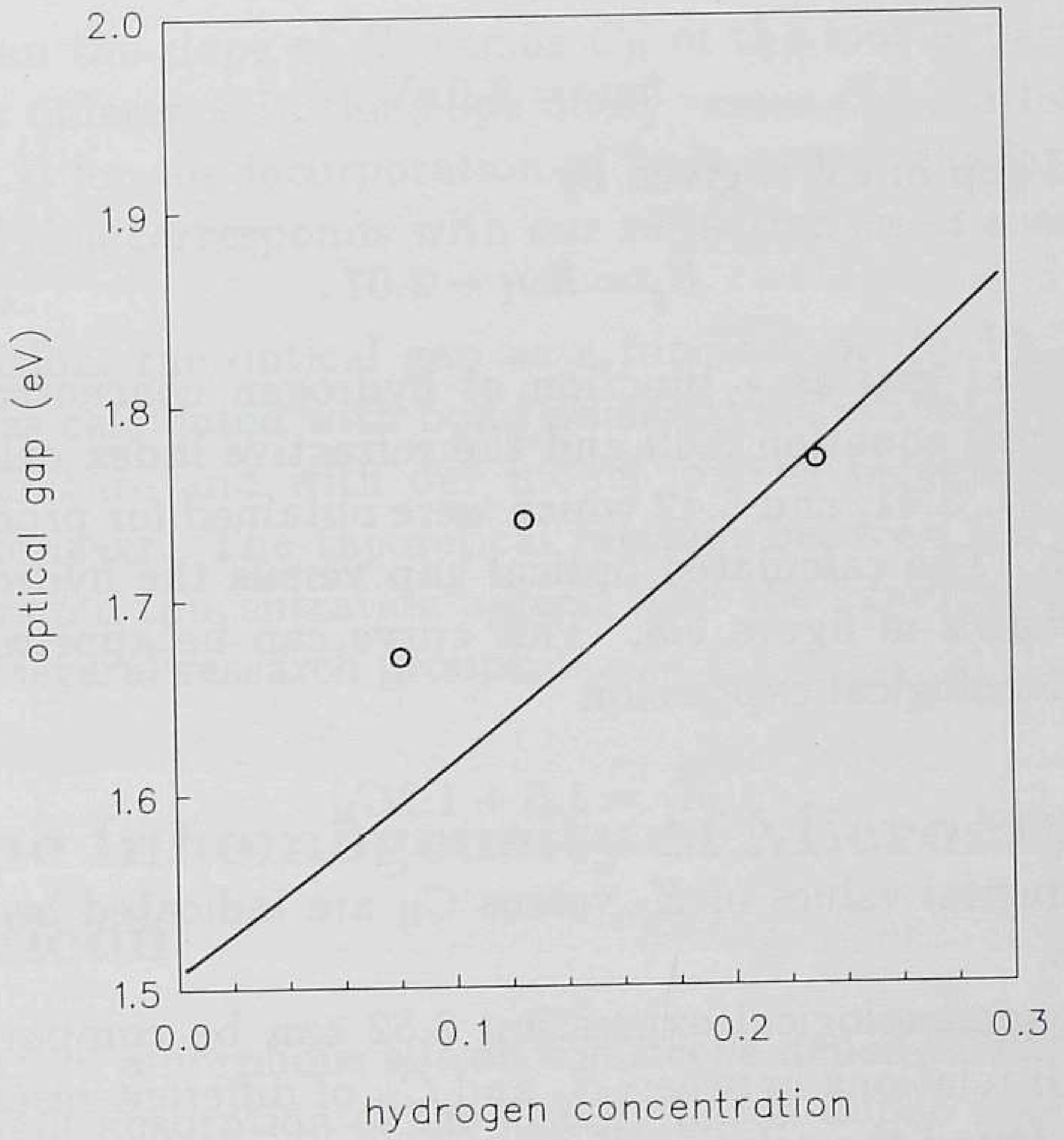

Figure 3.8: The optical gap versus the hydrogen concentration in atomic ratio. The line indicates the theoretical relation, and the circles indicate experimental data.

The optical gap will be described in terms of $\hbar\omega_1$. We will use the approximation that the shift in $\hbar\omega_1$ is the same as the shift in the optical gap

$$E_g = \text{constant} + \hbar\omega_1\,. \tag{3.48}$$

The peak position of the ε_2 spectrum ($\tilde{\varepsilon} = \varepsilon_1 - i\varepsilon_2$) which is equal to $\hbar\omega_1$ falls in the range of 3.55–3.75 eV [35,36]. The optical gap of a-Si:H with a low hydrogen content is about 1.5 eV [37,38,39,40]. We will use $\hbar\omega_1 = 3.6\,\text{eV}$, $n_\infty = 3.6$, and $E_g = 1.5\,\text{eV}$ at $C_\text{H} = 0$. $\hbar\omega_1$ is given by the following expression with the use of equations 3.45 and 3.47

$$\hbar\omega_1 = \hbar\omega_0\sqrt{1 - \frac{n_\infty^2 - 1}{n_\infty^2 + 2}}\,, \tag{3.49}$$

where

$$\hbar\omega_0 = 8.0\,\text{eV}\,. \tag{3.50}$$

The optical gap in eV is given by

$$E_g = \hbar\omega_1 - 2.07\,. \tag{3.51}$$

The optical gap as a function of hydrogen concentration can be calculated with equation 3.49 and the refractive index calculated with equations 3.37, 3.41, and 3.42 which were obtained for process A shown in figure 3.5. The calculated optical gap versus the hydrogen concentration is shown in figure 3.8. This curve can be approximated with the phenomenological expression

$$E_g = 1.5 + 1.2C_{\text{H}} \tag{3.52}$$

The experimental values of E_g versus C_{H} are indicated by open circles in figure 3.8.

The phenomenological expression 3.52 can be compared with the experimental relations between E_g and C_{H} of different research groups. Cody et al. found the relation [9]

$$E_g = 1.5 + 1.5\,C_{\text{H}}\,. \tag{3.53a}$$

The Matsuda's group found [41]

$$E_g = 1.48 + 1.9\,C_{\text{H}}\,. \tag{3.53b}$$

Ross et al. found [42]

$$E_g = 1.56 + 1.27\,C_{\text{H}}\,, \tag{3.53c}$$

and the relation

$$E_g = 1.7 + 1.7\,C_{\text{H}} \tag{3.53d}$$

was found by McKenzie et al. [43]. The few experimental points in figure 3.8, for the films deposited in our laboratory, are not enough to obtain an experimental relation like equations 3.53a–3.53d.

The theoretical relation between E_g and C_{H} (equation 3.52) corresponds reasonably well with the experimental relations (the four equations 3.53a–3.53d) considering the difference between the four experimental relations. The slope of E_g versus C_{H} of the theoretical relation is smaller than the slope of E_g versus C_{H} of the four experimental relations. This difference in the slope of E_g versus C_{H} can be explained with process B for the incorporation of hydrogen in the layer (see figure 3.5), and this corresponds with our refractive index measurements of section 3.5.

In conclusion, the optical gap as a function of the hydrogen concentration was calculated with bond polarizabilities that were obtained from the literature and with our model for the incorporation of hydrogen in the layer. The theoretical relation between the optical gap and the hydrogen concentration agreed with the experimental relation obtained by several research groups.

3.7 The Inhomogeneity of Microcrystalline Silicon

The efficiency of amorphous silicon solar cells depends strongly on the amount of light absorption of the heavily boron doped layer (p^+-layer) at the illuminated side of the solar cell (the window layer), because light that is absorbed in this layer does not contribute to the current in the solar cell. The standard p^+-layer of a-Si:H in a p-i-n solar cell can absorb 20% or more of the incident light. Microcrystalline silicon has the advantage of a lower absorption and a higher doping efficiency combined with a low activation energy. This results in a higher short circuit current (I_{sc}) and a higher open circuit voltage (V_{oc}) of the solar cell [26].

Microcrystalline silicon (μc-Si:H) is formed under different conditions than a-Si:H. The silane feed gas must be diluted with hydrogen up to 10 vol.% or less and higher rf power levels are necessary. This μc-Si:H consists of two phases of about 90 vol.% microcrystals, with an average diameter of 100 Å, embedded in an amorphous network [44]. We used Corning 7059 glass as a substrate and deposited layers in an rf glow discharge under the conditions for the growth of μc-Si:H. The deposition conditions are described in section 3.4.

Optical reflection and transmission measurements were used to characterize the films. The refractive index and absorption were obtained from the reflection and transmission by means of the computer fitting

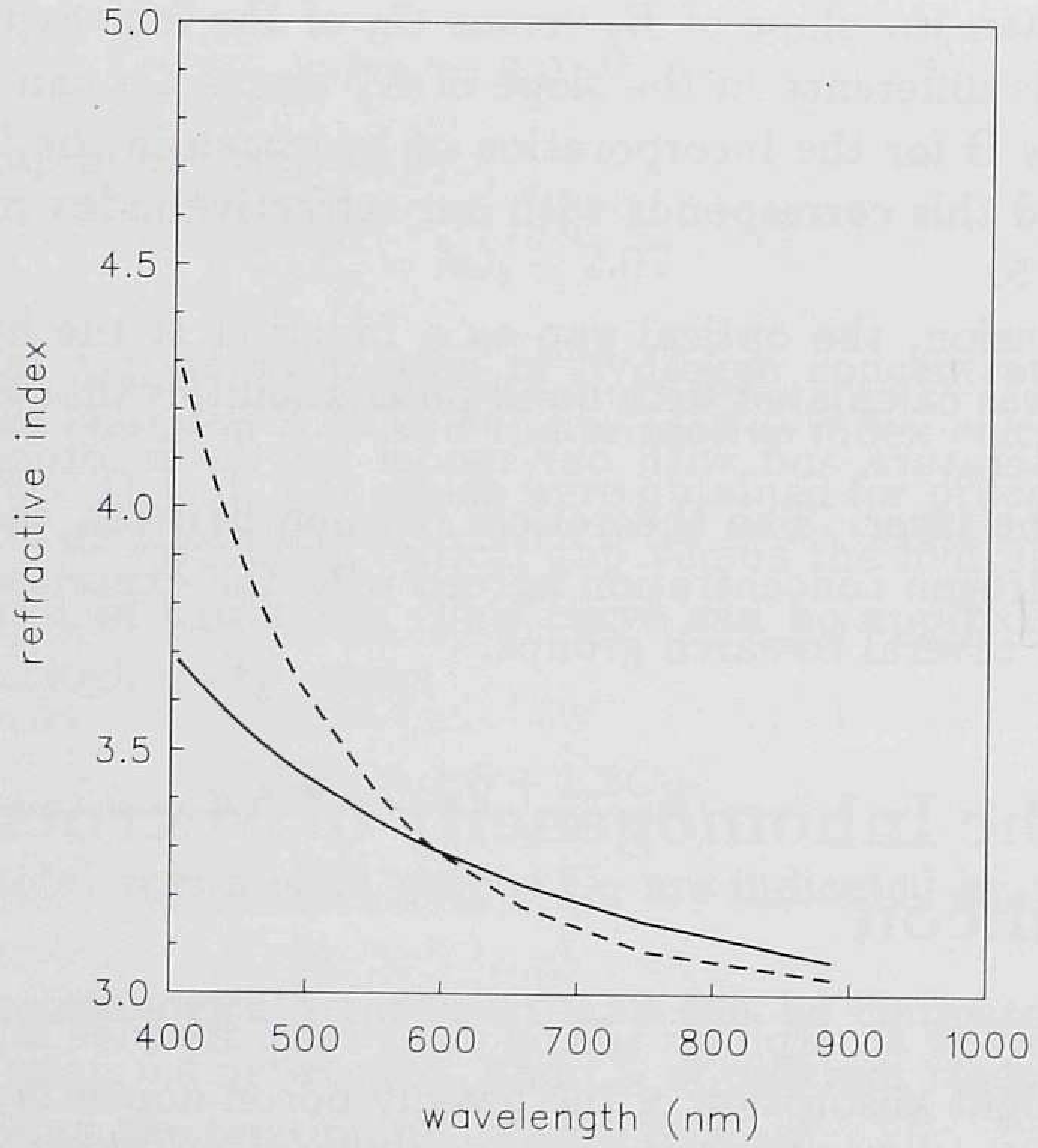

Figure 3.9: The refractive index of the μc-Si:H layer measured with the light incident at the substrate (dashed line) and with the light incident at the μc-Si:H layer (solid line).

procedure described in section 3.2. We found that the refractive index depended on the direction of the incident light. That is whether the light was incident at the substrate or incident at the μc-Si:H layer. Figure 3.9 shows the calculated refractive index when the light is incident at the substrate together with the calculated refractive index when the light is incident at the μc-Si:H. As can be seen from the figure the two curves are identical within experimental error between 600 nm and 900 nm. At shorter wavelengths the refractive index of the μc-Si:H layer measured from the substrate side increases faster than the other curve.

It has been reported that layers of a few hundred Ångstrom deposited under the conditions for the growth of μc-Si:H have different properties from layers thicker than approximately 1000 Å [26]. Transmission electron microscopy has been used to monitor the growth process of the μc-Si:H layer. Layers of a few hundred Ångstrom were amorphous and the microcrystalline phase increased with increasing film thickness [45]. We used this model to explain our optical measurements. When the glass substrate is placed in the glow discharge there is first the deposition of a thin a-Si:H layer and on top of that interfacial layer a μc-Si:H layer starts growing.

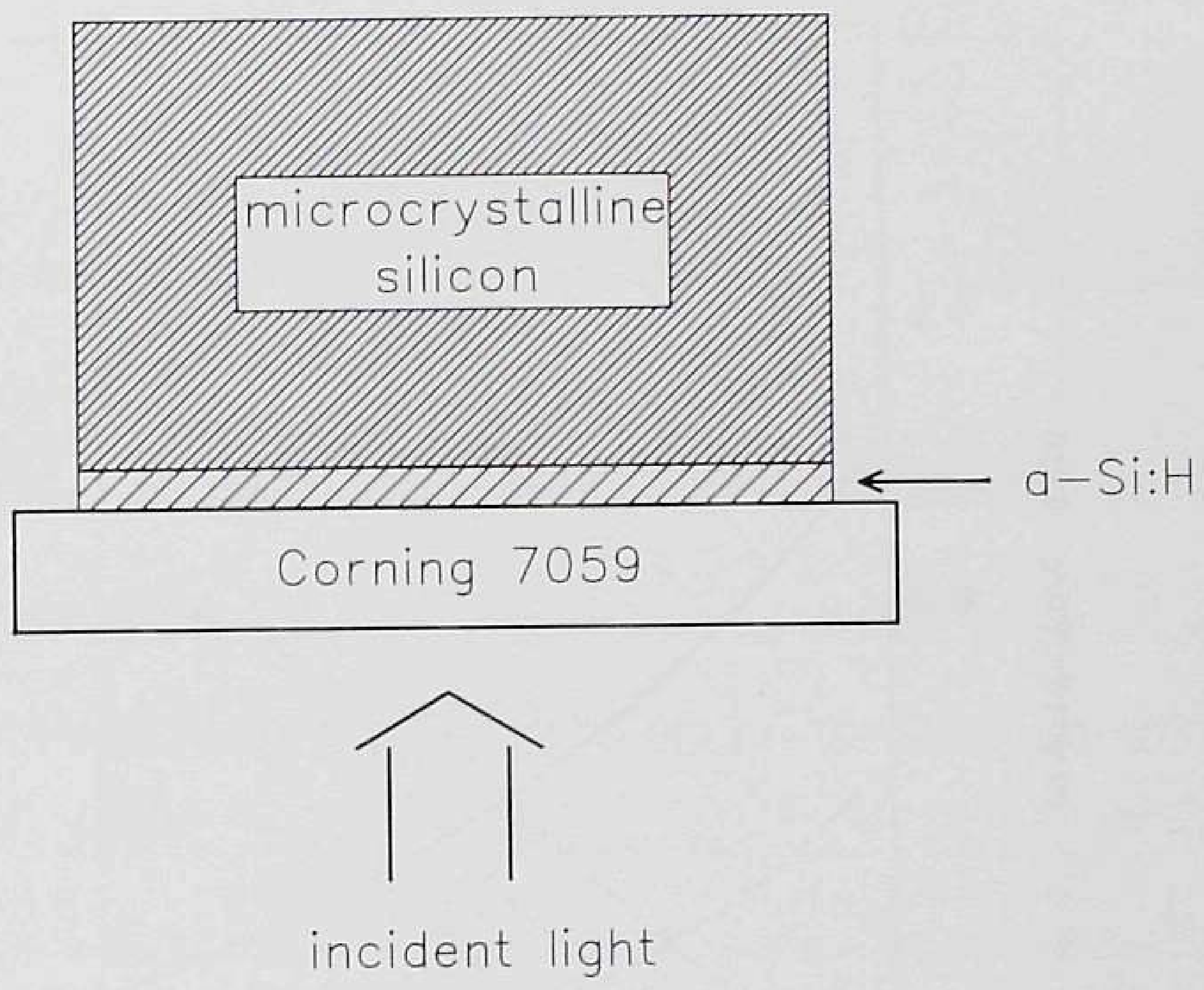

Figure 3.10: Optical system for the simulation of the reflection and transmission of a μc-Si:H layer.

Figure 3.10 shows the optical system that was used to calculate the reflection and transmission with the light incident at the substrate. For the refractive index of the a-Si:H layer and the μc-Si:H layer we used the experimental data of figure 3.11. There is a noticeable difference between the refractive index of a-Si:H and μc-Si:H. The cause of this difference is the lower density of μc-Si:H that reduces the refractive index [46]. This lower density is caused by the amorphous network with a low density that surrounds the microcrystals. The calculated reflection and transmission were treated in the same way as the measured reflection and transmission. We used the same fitting procedure to obtain the refractive index of one hypothetical homogeneous layer on the glass substrate. The result of this fitting procedure for three sets of simu-

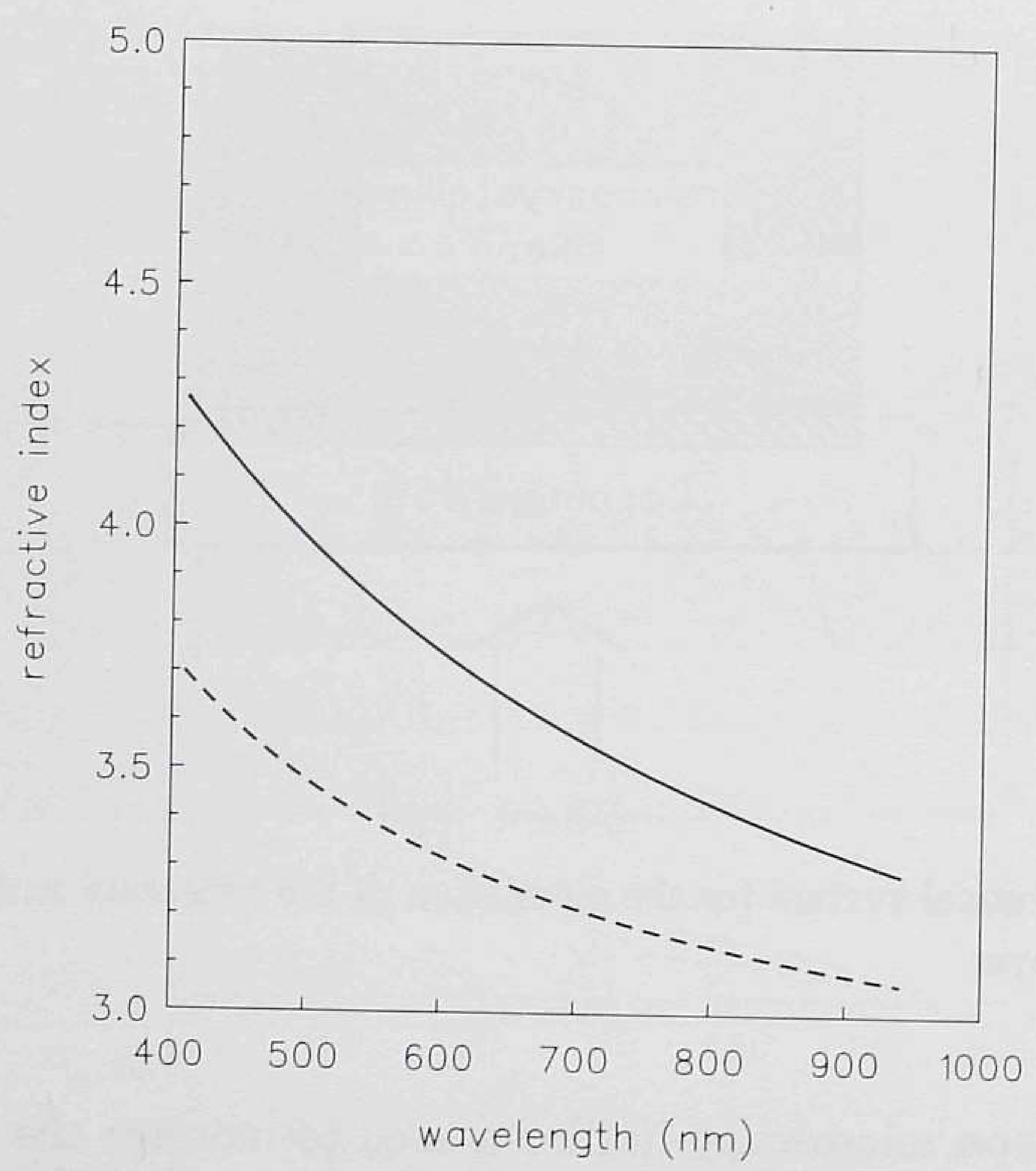

Figure 3.11: The refractive index of a-Si:H (solid line) and μc-Si:H (dashed line).

lated reflection and transmission data is shown in figure 3.12. As can be seen from the figure, the refractive index obtained from the calculated reflection and transmission with an a-Si:H layer of 200 Å corresponds with the refractive index obtained from the measured optical data with the light incident at the substrate.

The curve of the refractive index as a function of the wavelength can be explained by the wavelength dependent absorption. At decreasing wavelengths the penetration depth of the light decreases because of the increased absorption. At a small penetration depth the light incident at the substrate "sees" both the interfacial amorphous silicon layer and the μc-Si:H layer. The light incident at the μc-Si:H layer "sees" only the μc-Si:H material. Added to this effect is another effect caused by the fact that shorter wavelengths are more sensitive to interference effects caused by the thin interfacial a-Si:H layer. In this way the thin interfacial a-Si:H layer contributes more to the refractive index at shorter wavelengths, and with increasing thickness of the interfacial layer the refractive index at long wavelengths increases.

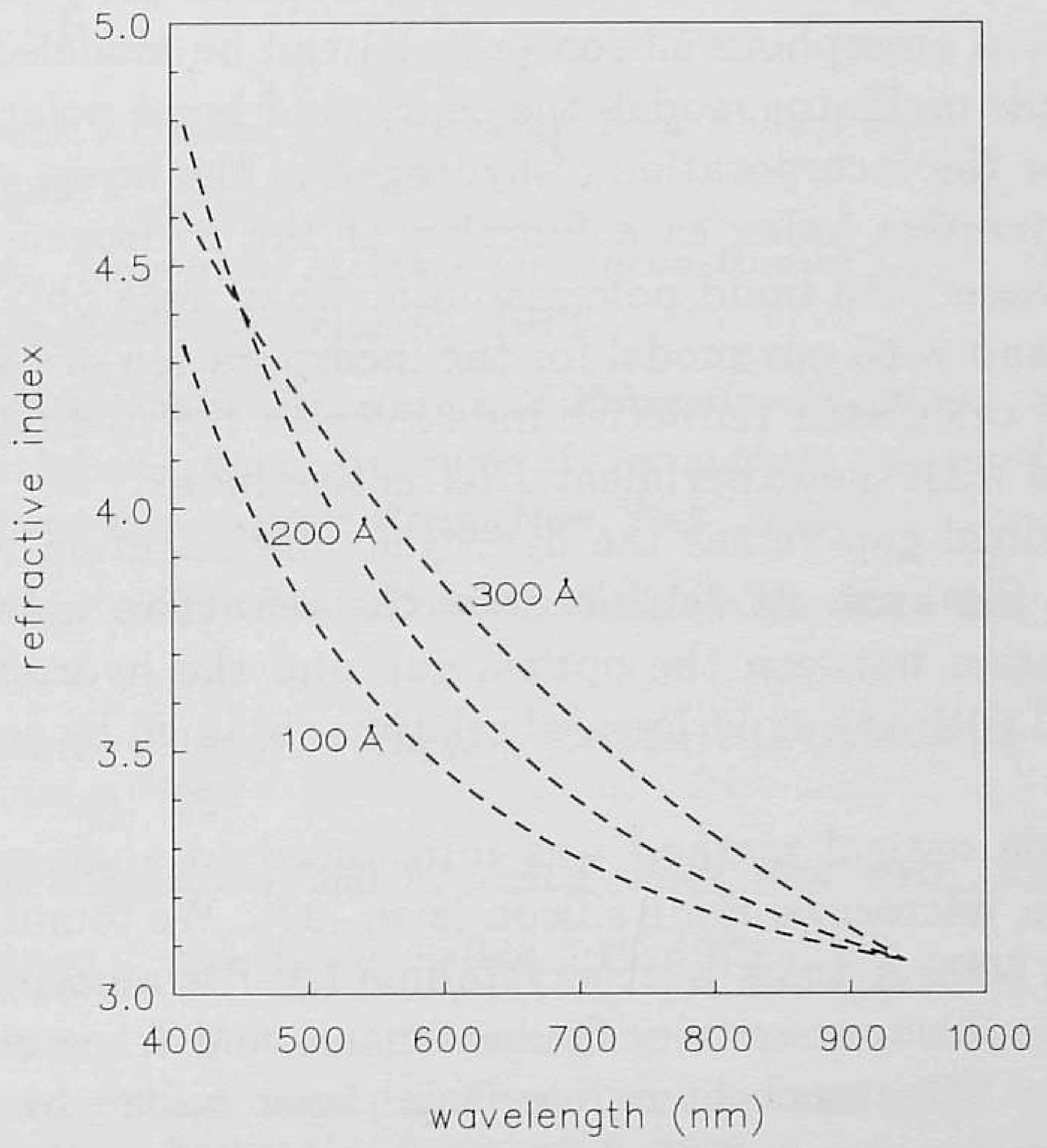

Figure 3.12: The calculated refractive index for the optical system of figure 3.10. Three different layer thicknesses have been used for the a-Si:H layer: 100 Å, 200 Å, and 300 Å.

In conclusion, a simple optical method has been developed to estimate the thickness of the amorphous interfacial layer of μc-Si:H films. This thickness, of the order of 200 Å, agrees with conductivity experiments on doped μc-Si:H [47]. The interfacial layer has to be eliminated to obtain an optimal p^+-layer for the window layer in amorphous silicon solar cells.

3.8 Conclusions

The refractive index at long wavelengths and the optical gap depend on the hydrogen concentration in the layer. We have shown that the influence of the hydrogen concentration on the optical properties of intrinsic hydrogenated amorphous silicon (a-Si:H) can be modeled with the single harmonic oscillator model, the concept of bond polarizabilities and a model for the incorporation of hydrogen in the layer.

The refractive index as a function of the hydrogen concentration was calculated with bond polarizabilities that were obtained from the literature and with our model for the incorporation of hydrogen in the layer. The calculated refractive index versus the hydrogen concentration agreed with the experimental refractive index.

The optical gap versus the hydrogen concentration was calculated employing the same models used for the refractive index. The theoretical relation between the optical gap and the hydrogen concentration agreed with the experimental relation obtained by several research groups.

A simple optical method was introduced to analyze the inhomogeneity of a microcrystalline silicon layer [27]. We found that the first 200 Å of a 5000 Å thick microcrystalline layer is amorphous. This result agrees with conductivity measurements and transmission electron microscopy. This amorphous interfacial layer has to be eliminated to obtain a good microcrystalline p^+ window layer for solar cells.

References

[1] O.S. Heavens. *Optical Properties of Thin Solid Films.* Butterworths, London, 1955.

[2] M.A. Wolfe. *Numerical Methods for Unconstrained Optimization.* Wokingham: van Nostrand Reinhold, 1978.

[3] M. Cardona. *Atomic Structure and Properties of Solids*, chapter Optical Properties and Band Structure of Germanium and Zincblende Type Semiconductors. Academic Press, New York, 1972.

[4] J.C. Phillips. *Solid State Physics.* Volume 18, Academic Press, New York, 1966.

[5] L. Ley. *Topics in Applied Physics*, chapter 3, pages 62–66. Volume 56, Springer-Verlag, 1984.

[6] J. Tauc, R. Grigorovici, and A. Vancu. *Phys. Stat. Sol.*, 15:627, 1966.

[7] N.K. Hindley. *J. Non-Cryst. Solids*, 5:17, 1970.

[8] E.A. Davis and N.F. Mott. Conduction in non-crystalline systems. v. conductivity, optical absorption, and photoconductivity in amorphous semiconductors. *Phil. Mag.*, 22:903–922, 1970.

[9] G.D. Cody, B. Abeles, C.R. Wronski, R.B. Stevens, and B. Brooks. Optical characterization of amorphous silicon hydride films. *Solar Cells*, 2:227–243, 1980.

[10] R.H. Klazes, M.H.L.M. van den Broek, J. Bezemer, and S. Radelaar. Determination of the optical bandgap of amorphous silicon. *Phil. Mag. B*, 45(4):377–383, 1982.

[11] G.D. Cody. *Semiconductors and Semimetals*, chapter 2, pages 11–82. Volume 21B, Academic Press, London, 1984.

[12] K.M.H. Maessen. *Hydrogenated Amorphous Silicon: Structure and Optical Properties.* PhD thesis, University of Utrecht, the Netherlands, 1988.

[13] F.C. Brown. *The Physics of Solids*, page 230. W.A. Benjamin, Inc., 1967.

[14] N.W. Ashcroft and N.D. Mermin. *Solid State Physics*, pages 534–542. Holt-Saunders International Editions, 1976.

[15] A.J. Dekker. *Solid State Physics*, page 156. Prentice Hall, 1958.

[16] N.F. Mott and E.A. Davis. *Electronic Processes in Non-Crystalline Materials*, page 383. Clarendon Press, Oxford, 2 edition, 1979.

[17] D. Penn. Wave-number-dependent dielectric function of semiconductors. *Phys. Rev.*, 128(5):2093–2097, 1962.

[18] J.C. Phillips. *Phys. Status Solidi B*, 44:41, 1971.

[19] J.C. Phillips. Ionicity of the chemical bond in crystals. *Rev. Mod. Phys.*, 42(3):317–356, 1970.

[20] J.A. van Vechten. Quantum dielectric theory of electronegativity in covalent systems. I. electronic dielectric constant. *Phys. Rev.*, 182(3):891–905, 1969.

[21] R.C. van Oort. *Hydrogenated Amorphous and Microcrystalline Silicon Deposited from Silane-Hydrogen Mixtures*. PhD thesis, Delft University of Technology, the Netherlands, 1989.

[22] M.J.M. Pruppers. *Phosphorus and Boron Doping of Hydrogenated Amorphous Silicon*. PhD thesis, University of Utrecht, the Netherlands, 1988.

[23] S. Veprek, Z. Iqbal, H.R. Ostwald, F.A. Sarrot, and J.J. Wagner. Parameters controlling the deposition of amorphous and microcrystalline silicon in Si/H discharge plasmas. *J. de Phys.*, 10:C4–251, 1981.

[24] R.C. van Oort, M.J. Geerts, and J.C. van den Heuvel. Growth model for hydrogenated microcrystalline silicon. *Appl. Surface Sc.*, 36:164, 1989.

[25] Y. Hamakawa. *Japan Annual Review in Electronics, Computers, and Telecommunication*. Elsevier Science Publ. B.V., 1984.

[26] S. Guha, J. Yang, P. Nath, and M. Hack. Enhancement of open-circuit voltage in high efficiency amorphous silicon solar cells. *Appl. Phys. Lett.*, 49(4):218, 1986.

[27] J.C. van den Heuvel, R.C. van Oort, M.J. Geerts, and J.W. Metselaar. Optical characterization of the interface between microcrystalline silicon and the substrate. In *The Euroforum New Energies Congress and Exhibition*, pages 167–169, 1988.

[28] Melles Griot. *Optics Guide 3*, page 65. Melles Griot, 1985.

[29] H.A. Lorentz. *Ann. Physik.*, 9:641, 1880.

[30] L. Lorenz. *Ann. Physik.*, 11:702, 1880.

[31] N.W. Ashcroft and N.D. Mermin. *Solid State Physics*, pages 542–552. Holt-Saunders International Editions, 1976.

[32] L. Ley. *Topics in Applied Physics*, chapter 3, pages 137–141. Volume 56, Springer-Verlag, 1984.

[33] E.C. Freeman and W. Paul. Optical constants of rf sputtered hydrogenated amorphous silicon. *Phys. Rev. B*, 20(2):716–728, 1979.

[34] R.C Weast. *CRC Handbook of Chemistry and Physics*, pages E–70. Edition 67, CRC Press, Florida, 1986.

[35] D. Ewald, M. Milleville, and G. Weiser. Optical spectra of glow-discharge-deposited silicon. *Phil. Mag. B*, 40:291–303, 1979.

[36] G. Weiser, D. Ewald, and M. Milleville. *J. Non-Cryst. Solids*, 35&36:447, 1980.

[37] M.H. Brodsky, R.S. Title, K. Weiser, and G.D. Petit. Structural, optical, and electrical properties of amorphous silicon films. *Phys. Rev. B*, 1(6):2632–2641, 1970.

[38] P.G. LeComber, R.J. Loveland, W.E. Spear, and R.A. Vaughn. In *Proc. Vth Intern. Conf. Amorphous and Liquid Semiconductors*, page 245, Taylor and Francis, London, 1974.

[39] M. Hirose, M. Taniguchi, and Y. Osaka. In *Proc. 7th Intern. Conf. Amorphous and Liquid Semiconductors*, page 352, University of Edinburgh, 1977.

[40] M. Janai, D.D. Aldred, D.C. Booth, and B.O. Seraphin. Optical properties and structure of amorphous silicon films prepared by CVD. *Sol. Energy Mat.*, 1:11–27, 1979.

[41] A. Matsuda, M. Matsumura, S. Yamasaki, H. Yamamoto, T. Imura, H. Okushi, S. Iizima, and K. Tanaka. Boron doping of hydrogenated silicon thin films. *Jap. J. Appl. Phys.*, 20(3):L183–L186, 1981.

[42] R.C. Ross and J. Jaklik Jr. Plasma polymerization and deposition of amorphous hydrogenated silicon from rf and dc silane plasmas. *J. Appl. Phys.*, 55(10):3785–3794, 1984.

[43] D.R. McKenzie, N. Savvides, R.C. McPhedran, L.C. Botten, and R.P. Netterfield. Optical properties of a-Si and a-Si:h prepared by dc magnetron techniques. *J. Phys. C*, 16:4933–4944, 1983.

[44] N. Abadou, N. Bustarret, A. Deneuville, and M. Toulemonde. Influence of hydrogen and residual disorder on the optical and electrical properties of microcrystalline silicon. *J. Non-Cryst. Solids*, 59&60:803–806, 1983.

[45] T. Imura, H. Kaya, H. Terauchi, H. Kiyono, A. Hiraki, and M. Ichihara. Structure change of microcrystalline silicon films in deposition process. *Jap. J. Appl. Phys.*, 23(2):179–183, 1984.

[46] D.E. Aspnes. Optical properties of thin films. *Thin Solid Films*, 89(3):249–262, 1982.

[47] H.M. Wentinck. *Carrier Injection in Amorphous Silicon Devices.* PhD thesis, Delft University of Technology, the Netherlands, 1988. page 52.

Chapter 4

Diffusion Length Measurements

4.1 Introduction

The diffusion length is a parameter that is closely related to the performance of a solar cell. In a solar cell the current is limited by recombination of the generated holes and electrons and the diffusion length is related to this recombination. The minority carrier diffusion length is the average distance that a generated minority carrier travels in the absence of an electric field before it recombines with a majority carrier. In intrinsic hydrogenated amorphous silicon (a-Si:H) the hole density and electron density are equal. Therefore, the diffusion length of a-Si:H is called the ambipolar diffusion length.

The ambipolar diffusion length of a-Si:H was measured by the Surface Photovoltage (SPV) technique. The principle of this technique is based on the illumination of a transparent rectifying contact with monochromatic light at different wavelengths. The resulting photovoltage is held constant by adjusting the light intensity at each wavelength. The diffusion length is obtained from the plot of the light intensity versus the reciprocal absorption coefficient ($1/\alpha$).

Schottky barriers of thin chromium layers or tin-oxide layers were used as the transparent rectifying contact for the SPV measurements. In addition to applications such as large area electron devices [1], Schottky barrier diodes made of a-Si:H are important tools in studying the electrical and photoelectrical properties of a-Si:H. The barrier parameters of the diodes (ideality factor and barrier height) have been used to measure the properties of a-Si:H [2,3,4,5]. Schottky barrier diodes have also been used to measure the density of states in the gap of a-Si:H through capacitance-voltage measurements.

In section 4.2 the method used to obtain the diffusion length is described in detail. In subsection 4.2.1 the differential equations (the current-density and continuity equations) are solved for the case of a-Si:H, and it is shown that the ambipolar diffusion length, instead of the minority carrier diffusion length, is obtained since the hole and electron densities are of the same order of magnitude. In subsection 4.2.2 an extension of the method is presented for the diffusion length measurement of thin layers. This extended method takes into account the effect of the reflection of light at the back contact in thin layers and the effect of a finite bandwidth of the monochromatic light [6].

The experimental setup for the diffusion length measurements is described in section 4.3.

In section 4.4 the results of SPV measurements on thin devices are shown. These measurements are analyzed with the extended method described in subsection 4.2.2.

In section 4.5 the effect of the substrate on the diffusion length and on the quality of the diode is studied. The properties of the material close to the substrate can differ substantially from the properties of the bulk of the material. This can be caused by the deposition process itself as has been shown by ellipsometry [7] or by diffusion of impurities from the substrate [8]. To study these effects diodes were made with the Schottky barrier at the substrate/a-Si:H interface. We used current-voltage (I-V) measurements to obtain the ideality factor and used the SPV technique to obtain the diffusion length. The diffusion length as determined by the SPV technique measures the material close to the substrate (with a characteristic distance equal to the diffusion length). But the SPV technique is much less sensitive to interface states compared to the parameters of the Schottky barrier (as obtained from I-V measurements). By comparing the diodes on tin-oxide and chromium coated substrates we tried to measure the influence of the diffusion of tin [9] on the current-voltage characteristics and on the diffusion length.

4.2 Theory of Surface Photovoltage Measurements

4.2.1 Solving the Differential Equations

The Surface Photovoltage (SPV) technique uses light generation to measure the minority carrier diffusion length. The principle of the technique is that minority carriers are generated in the bulk of the semiconductor and diffuse to the collecting surface, which results in a surface photovoltage.

The SPV technique was invented by Goodman who used it to obtain the minority carrier diffusion length [10]. The method is based on the following diffusion equation for n-type material:

$$D_p \frac{d^2 \Delta p}{dx^2} - \frac{\Delta p}{\tau_p} + \alpha I_{ph}\, e^{-\alpha x} = 0\,, \tag{4.1}$$

where $\alpha I_{ph}\, e^{-\alpha x}$ is the light generation term with α as the absorption coefficient, I_{ph} as the photon flux, and x as the distance from the surface. D_p is the hole diffusion coefficient, τ_p is the hole lifetime, and $\Delta p(x)$ $(= p(x) - p_0)$ is the excess hole concentration with p_0 as the equilibrium hole concentration.

The solution of this equation is of the form (with the condition $\Delta p \to 0$ when $x \to \infty$)

$$\Delta p = A\, e^{-x/L_p} + \frac{\alpha I_{ph} \tau_p}{1 - L_p^2 \alpha^2}\, e^{-\alpha x}\,, \tag{4.2}$$

where L_p is the minority carrier diffusion length defined by $L_p = \sqrt{D_p \tau_p}$, and A is a constant that depends on the boundary conditions. The boundary condition at the surface ($x = 0$) is

$$S_p \Delta p = D_p \frac{d\Delta p}{dx}\,, \tag{4.3}$$

where S_p is the hole surface recombination velocity. This gives the following result for A and $\Delta p(0)$:

$$A = -\frac{\alpha I_{ph} \tau_p}{1 - L_p^2 \alpha^2} \left(\frac{S_p + \alpha D_p}{S_p + D_p / L_p} \right) \tag{4.4}$$

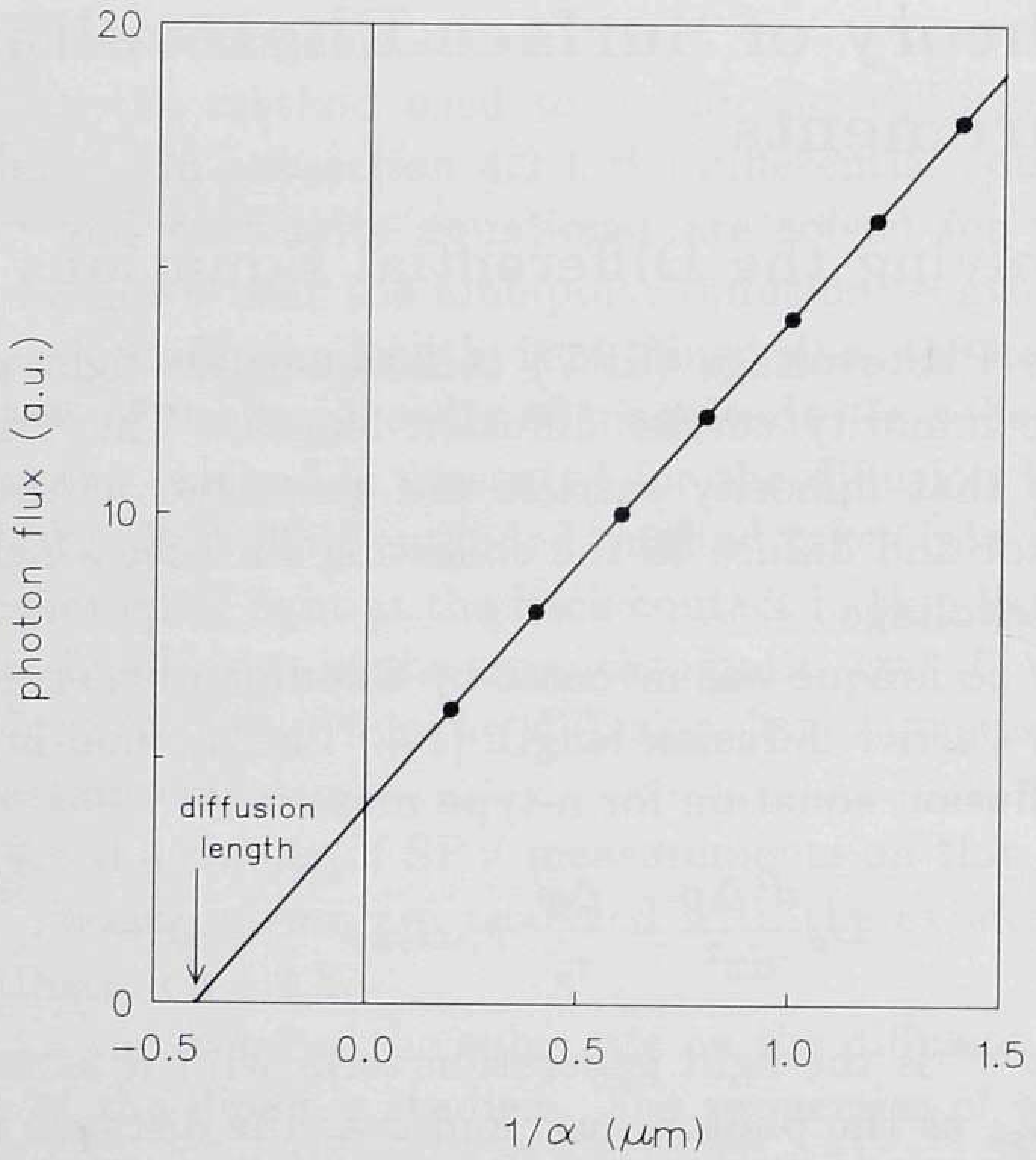

Figure 4.1: The graphic method of obtaining the diffusion length. The intercept of the straight line on the negative $1/\alpha$ axix yields the diffusion length.

and

$$\Delta p(0) = \frac{\alpha}{\alpha + 1/L_p} \cdot \frac{I_{ph}}{S_p + D_p/L_p} \,. \tag{4.5}$$

It is assumed that the surface photovoltage (ΔV) is a monotonic function of $\Delta p(0)$. If ΔV is fixed in the experiment, then $\Delta p(0)$ will also be fixed. We can rewrite equation 4.5 to obtain the photon flux in the situation of a constant photovoltage (i.e., a constant $\Delta p(0)$):

$$I_{ph} = \text{constant}\,(1/\alpha + L_p) \,. \tag{4.6}$$

Thus if the photon flux, required to keep the photovoltage constant at each wavelength, is plotted versus $1/\alpha$, then the result will be a straight line whose intercept on the negative $1/\alpha$ axis yields the minority carrier diffusion length L_p. This graphic method is illustrated in figure 4.1.

The SPV technique is often used to determine the diffusion length in a-Si:H [11,12,13]. In the articles by McElheny et al. the use of the SPV technique to measure the diffusion length of a-Si:H is disputed [14,15]. They showed by computer simulation that the hole drift current and the hole diffusion current are of the same order of magnitude. We will show that the SPV technique in the case of a-Si:H gives the ambipolar diffusion length which consists of the mobility and lifetime of both holes and electrons. In this case the drift current is not negligible.

In the case of intrinsic a-Si:H the generated carrier concentration exceeds the thermal equilibrium concentration. We cannot use the diffusion equation 4.1, because the holes cannot be considered as minority carriers. We will use the following equation

$$\frac{kT}{q}\left(\frac{\mu_n^d \mu_p^d}{\mu_n^d n_t + \mu_p^d p_t}\right)\left(p_t \frac{d^2 n_t}{dx^2} + n_t \frac{d^2 p_t}{dx^2}\right) - U + \alpha I_{ph}\, e^{-\alpha x} = 0 \,, \tag{4.7}$$

where U is the recombination, p_t is the total hole concentration, n_t is the total electron concentration, μ_p^d and μ_n^d are the hole and electron drift mobilities, respectively. The total hole concentration is the hole concentration in the extended states p_e and the hole concentration in the valence band tail p_{vt}. The total electron concentration is defined in a similar way, but here the electrons are trapped in the conduction band tail. The total electron concentration and total hole concentration are

$$n_t = n_e + n_{ct} \quad \text{and} \quad p_t = p_e + p_{vt} \,. \tag{4.8}$$

The drift mobilities are defined as

$$\mu_n^d = \frac{n_e}{n_t}\mu_n^e \quad \text{and} \quad \mu_p^d = \frac{p_e}{p_t}\mu_p^e \,, \tag{4.9}$$

where μ_n^e and μ_p^e are the extended states mobilities of electrons and holes, respectively. Because the tail states are in thermal equilibrium with the extended states, the drift mobilities can be regarded as constants.

Equation 4.7 can be derived from the current-density equations

$$J_n = q\mu_n^d n_t \mathcal{E} + kT\mu_n^d \frac{dn_t}{dx}\,, \tag{4.10}$$

$$J_p = q\mu_p^d p_t \mathcal{E} - kT\mu_p^d \frac{dp_t}{dx}\,, \tag{4.11}$$

and the continuity equation

$$\frac{1}{q}\frac{dJ_p}{dx} = -\frac{1}{q}\frac{dJ_n}{dx} = \alpha I_{ph}\, e^{-\alpha x} - U\,. \tag{4.12}$$

In these equations is $\mathcal{E}$ the electric field. The following equation is obtained by eliminating the electric field from equations 4.10 and 4.11:

$$\mu_p^d \frac{p_t}{n_t} J_n - \mu_n^d J_p = kT\mu_p^d \frac{p_t}{n_t}\mu_n^d \frac{dn_t}{dx} + kT\mu_n^d\mu_p^d \frac{dp_t}{dx}\,. \tag{4.13}$$

If we assume charge neutrality in the bulk then $p_t = n_t$. Equation 4.7 can now be derived by differentiating equation 4.13 to x (p_t/n_t is a constant) and substituting dJ_p/dx and dJ_n/dx using equation 4.12.

Equation 4.7 can be rewritten in the following form using $p_t = n_t$

$$2\frac{kT}{q}\left(\frac{\mu_n^d\mu_p^d}{\mu_n^d + \mu_p^d}\right)\frac{d^2 p_t}{dx^2} - U + \alpha I_{ph}\, e^{-\alpha x} = 0\,. \tag{4.14}$$

For the recombination we will use the Shockley-Read-Hall equation

$$U = \frac{p_t n_t - n_i^2}{n_t\tau_p + p_t\tau_n} \approx \frac{p_t}{\tau_p + \tau_n}\,, \tag{4.15}$$

where we have used $p_t n_t \gg n_i^2$, and $n_t = p_t$.

The solution of equation 4.14 is

$$p_t = A\, e^{-x/L_d} + \frac{\alpha I_{ph}(\tau_p + \tau_n)}{1 - L_d^2\alpha^2}\, e^{-\alpha x}\,, \tag{4.16}$$

where L_d is the so-called ambipolar diffusion length given by

$$L_d = \sqrt{2\frac{kT}{q}\left(\frac{\mu_n^d\mu_p^d}{\mu_n^d + \mu_p^d}\right)(\tau_p + \tau_n)}\,. \tag{4.17}$$

This expression for the ambipolar diffusion length was also obtained by Moore in a different way [11,12]. He used an equation obtained by Rothwarf and Böer [16] for the case of a constant electric field and assumed this field to be equal to zero. However, the assumption that the electric field is equal to zero is not correct as will be shown later on. We have not used this assumption, but we have eliminated the electric field from equations 4.11 and 4.10.

With the solution for the hole concentration of equation 4.16 it is possible to obtain the hole drift current and the hole diffusion current. The hole diffusion current density is given by

$$J_p^{\text{diff}} = -kT\mu_p^d \frac{dp_t}{dx} = kT\mu_p^d\left(\frac{A}{L_d}\, e^{-x/L_d} + \frac{\alpha^2 I_{ph}(\tau_p + \tau_n)}{1 - \alpha^2 L_d^2}\, e^{-\alpha x}\right)\,, \tag{4.18}$$

and the hole drift current density is given by

$$J_p^{\text{drift}} = q\int \frac{1}{q}\frac{dJ_p^{\text{drift}}}{dx}\,dx \tag{4.19a}$$

$$= q\int\left(G - U - \frac{1}{q}\frac{dJ_p^{\text{diff}}}{dx}\right)dx \tag{4.19b}$$

$$= \frac{qL_d^2 - kT\mu_p^d(\tau_p + \tau_n)}{\tau_p + \tau_n}\left(\frac{A}{L_d}\, e^{-x/L_d} + \frac{\alpha^2 I_{ph}(\tau_p + \tau_n)}{1 - \alpha^2 L_d^2}\, e^{-\alpha x}\right)\,. \tag{4.19c}$$

It is clear that the drift component cannot be neglected in all cases. The approximation $\mu_n^d \gg \mu_p^d$ gives the result that $J_p^{\text{drift}} = J_p^{\text{diff}}$. This result has also been obtained by McElheny et al. who used $\mu_n^e = 10\,\text{cm}^2/\text{Vs}$ and $\mu_p^e = 1\,\text{cm}^2/\text{Vs}$. This drift current assists the diffusion current and increases the measured diffusion length. If $\mu_n^d = \mu_p^d$, we obtain $J_p^{\text{drift}} = 0$.

If the electric field in equation 4.11 is assumed to be zero, the following diffusion equation is obtained by differentiating equation 4.11 to x and by substituting dJ_p/dx of equation 4.12

$$kT\mu_p^d \frac{d^2 p_t}{dx^2} - \frac{p_t}{(\tau_p + \tau_n)} + \alpha I_{ph}\, e^{-\alpha x} = 0\,. \tag{4.20}$$

In this case the diffusion length is

$$L_d = \sqrt{\frac{kT}{q}\mu_p^d(\tau_p + \tau_n)}\,. \tag{4.21}$$

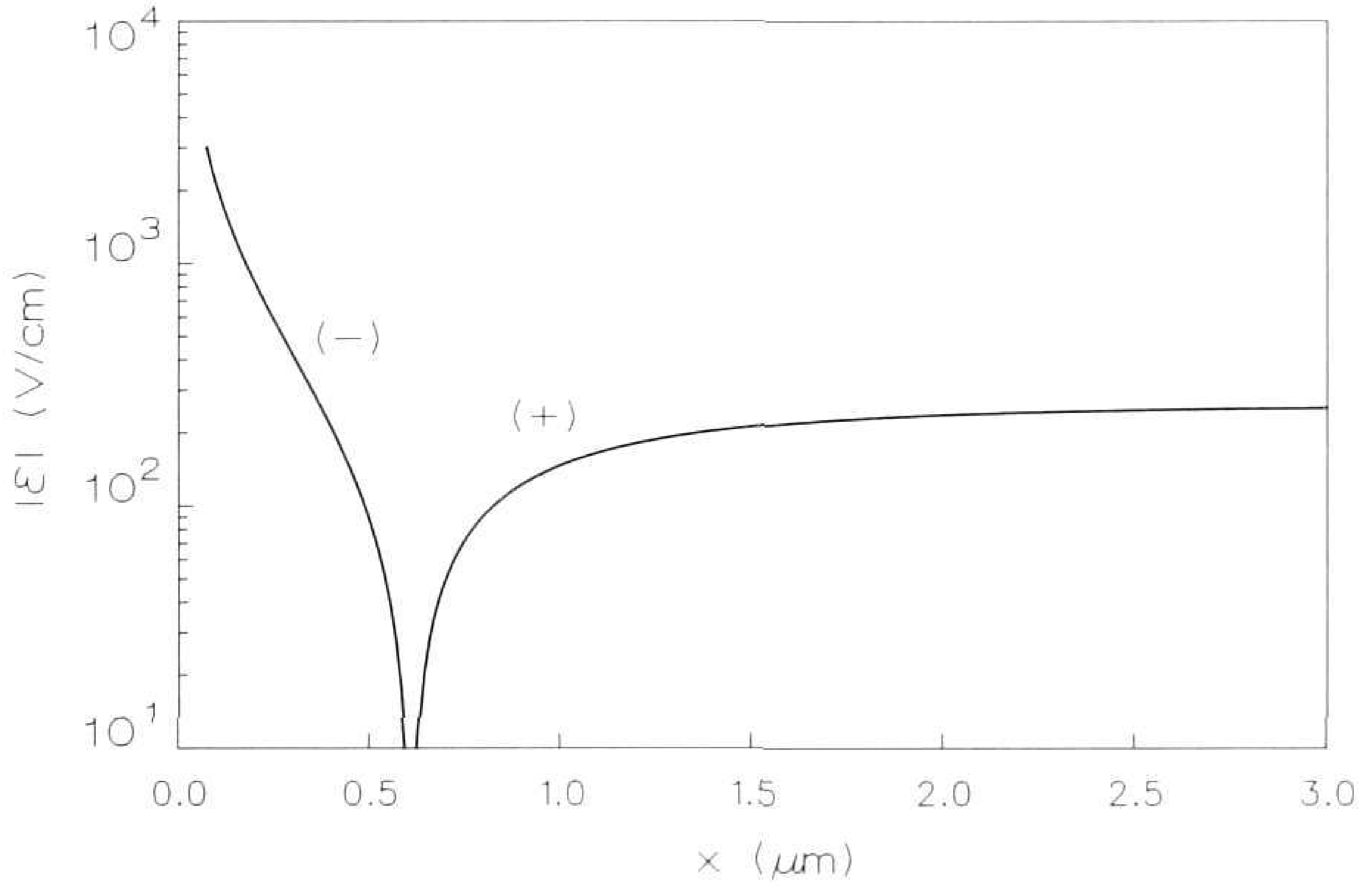

Figure 4.2: The electric field versus the distance from the surface with $L_d = 0.4\,\mu\text{m}$, $\mu_p^d = 1\,\text{cm}^2/\text{Vs}$, $\alpha = 1\,\mu\text{m}^{-1}$, $S_p = 10^7\,\text{cm/s}$, and $T = 300\,\text{K}$.

The ambipolar diffusion length for $\mu_n^d \gg \mu_p^d$ is obtained from equation 4.17 and is

$$L_d = \sqrt{2\frac{kT}{q}\mu_p^d(\tau_p + \tau_n)}\,. \tag{4.22}$$

Clearly the measured diffusion length is increased by a factor $\sqrt{2}$ compared to the situation with only diffusion.

The assumption that the hole concentration equals the electron concentration in the bulk has to be verified. It can be seen from the Poisson equation that the electric field has to be a constant when $p_t = n_t$. This is true for $\mu_p^d = \mu_n^d$ in which case the drift current equals zero as can be obtained from equation 4.19, so the electric field is a constant equal to zero. When $\mu_p^d = \mu_n^d$ the ambipolar diffusion length is given by equation 4.21.

For $\mu_n^d \gg \mu_p^d$ the electric field is not a constant. This can be seen from equations 4.16 and 4.19, because when J_p^{drift} is divided by p_t we obtain $q\mu_p^d\mathcal{E}$ which is not a constant. In figure 4.2 the electric field is shown as a function of x. The electric field is independent of the photon flux I_{ph}, so for high light intensity a small mismatch in the hole and electron concentration can generate this electric field. In the SPV technique high light intensities are used to decrease the width of the depletion layer, and this ensures that the condition $p_t = n_t$ is approximately true. Since the condition $p_t = n_t$ is only approximately true, the measured diffusion length is an averaged value of equations 4.21 and 4.22. The difference between the two values is about 40%, so the SPV technique gives a good estimation of the quality of the material.

In conclusion, the SPV technique can be used in the case of a-Si:H, but gives the ambipolar diffusion length which consists of the mobility and lifetime of both holes and electrons. In this case the hole drift current is of the same order of magnitude as the hole diffusion current. The drift current assists the diffusion current and increases the measured diffusion length by a factor $\sqrt{2}$ compared to the situation with diffusion alone. The drift current is caused by the difference in mobility between holes and electrons, thus in the case of equal mobilities the drift current is negligible.

4.2.2 Extended Method in the Case of Thin Layers

In the theory of the previous subsection we have not taken into account the width of the space charge region. This is not correct for a-Si:H since the diffusion length is of the same order of magnitude as the width of the space charge region in this material. The experimental solution is to use red bias light of high intensity to reduce the space charge width [12]. In the following theoretical analysis the space charge region will be incorporated in the analysis.

The sample is assumed to be one dimensional, divided into the space-charge region, $0 < x \leq W$, and the bulk, $W < x \leq d$. According to the theory of Moore [12] and Reichman [17], in the space-charge region holes and electrons flow in response to the local field and to concentration gradients but there is no recombination. However, there is surface recombination when the surface recombination velocity is high, and this recombination causes electrons to flow back to the surface and lower the photovoltage. In the bulk it is assumed that there is no electric field, carriers flow only by diffusion, and recombination is included.

The diffusion length is obtained from the photon flux versus the absorption coefficient. The formula given by Moore for the photon flux that is needed to keep the photovoltage constant is [12]

$$I_{ph} = \frac{\text{constant}\,(1/\alpha + L_d)(1 + V_T\mu_n^d/S_nF_1)F_1}{(1/\alpha + L_d)(1 + V_T\mu_n^d/S_nF_2)F_2 - (1 + V_T\mu_n^d/S_nF_1)(F_1/\alpha)e^{-\alpha W}}\,. \tag{4.23}$$

In this equation V_T is the thermal voltage kT/q, μ_n^d is the drift mobility of electrons, S_n is the electron surface recombination velocity, and F_1 and F_2 are integrating factors which lead to this result. Equation 4.23 leads to the following equation for small values of W ($W \ll L_d$)

$$I_{ph} = \text{constant}\,(1/\alpha + L_d)\,. \tag{4.24}$$

For small values of W, F_1 becomes equal to F_2. The condition $W \ll L_d$ is obtained in the experiment by using red bias light to reduce the space charge width. Equation 4.23 was obtained with the following expression for the generation of a sample with an infinite sample thickness

$$G(x) = q\alpha I_{ph}(1 - R)e^{-\alpha x}\,, \tag{4.25}$$

where R is the reflection of light from the surface, and x is the position in the sample.

For our model we first consider the current that is collected using the approximations mentioned above:

$$J(I_{ph}, \alpha) = \int_0^W G(x)\,dx + \int_W^d G(x)\,e^{(W-x)/L_d}\,dx\,. \tag{4.26}$$

The photon flux used to obtain a constant photovoltage is

$$I_{ph}(\alpha) = \frac{\text{constant}}{J(I'_{ph} = \text{constant}, \alpha)}\,. \tag{4.27}$$

Equation 4.26 and equation 4.27 can be evaluated using equation 4.25 for the generation in the case of an infinite sample thickness. We obtain for the photon flux

$$I_{ph}(\alpha) = \frac{\text{constant}\,(1/\alpha + L_d)}{(1/\alpha + L_d) - (1/\alpha)e^{-\alpha W}}\,. \tag{4.28}$$

This equation is equivalent to equation 4.23 in the case of a negligible surface recombination of electrons. For a negligible surface recombination S_n tends to zero, and the factors $(1 + V_T\mu_n^d/S_nF_1)F_1$ and $(1 + V_T\mu_n^d/S_nF_2)F_2$ tend to $V_T\mu_n^d/S_n$. Since the latter factor appears both in the numerator and denominator the result is equal to equation 4.28. In our experiments we found that the surface recombination of electrons can be disregarded, because at short wavelengths there was no decrease in the photovoltage which is the case for a high surface recombination. If the surface recombination effect is present, it occurs at short wavelengths when the generation is close to the surface due to the high absorption.

In the case of a finite sample thickness we have to replace the generation given by equation 4.25 with the following equation

$$G(x) = G_0(x) \cdot \frac{n_1}{n_0}\,|t_1|^2 \left|\frac{1 + r_2e^{-2i\delta(d-x)}}{1 - r_2r'_1e^{-2i\delta d}}\right|^2, \tag{4.29a}$$

$$G_0(x) = q\alpha I_{ph}e^{-\alpha x}\,, \tag{4.29b}$$

$$\tilde{\delta} = 2\pi\frac{n_1 - ik_1}{\lambda}\,, \tag{4.29c}$$

where n_0, n_1 and n_2 are the refractive indices, r'_1, r_2 and t_1 are the Fresnel coefficients, λ is the wavelength, and k_1 is the extinction coefficient. The indices refer to the notation used by Heavens [18] and the optical system that is depicted in figure 4.3.

To obtain the diffusion length it is no longer possible to use the simple graphic method based on equation 4.6. We used equations 4.26, 4.27, and 4.29 to calculate the curve of I_{ph} versus λ and adjusted L_d to obtain the best fit to the experimental photon flux.

In section 4.4 measurements of devices of 0.568 μm thick are analyzed using this extended method. The fabrication of the devices is described in chapter 2.

4.3 Experimental Setup

The experimental apparatus for the SPV measurements is schematically depicted in figure 4.4. One halogen lamp gives the probe light, the other lamp is used for the red bias light to reduce the space charge width. The probe light passes a chopper and a filter wheel that contains 8 band filters. The band filters are ORIEL narrow band interference filters

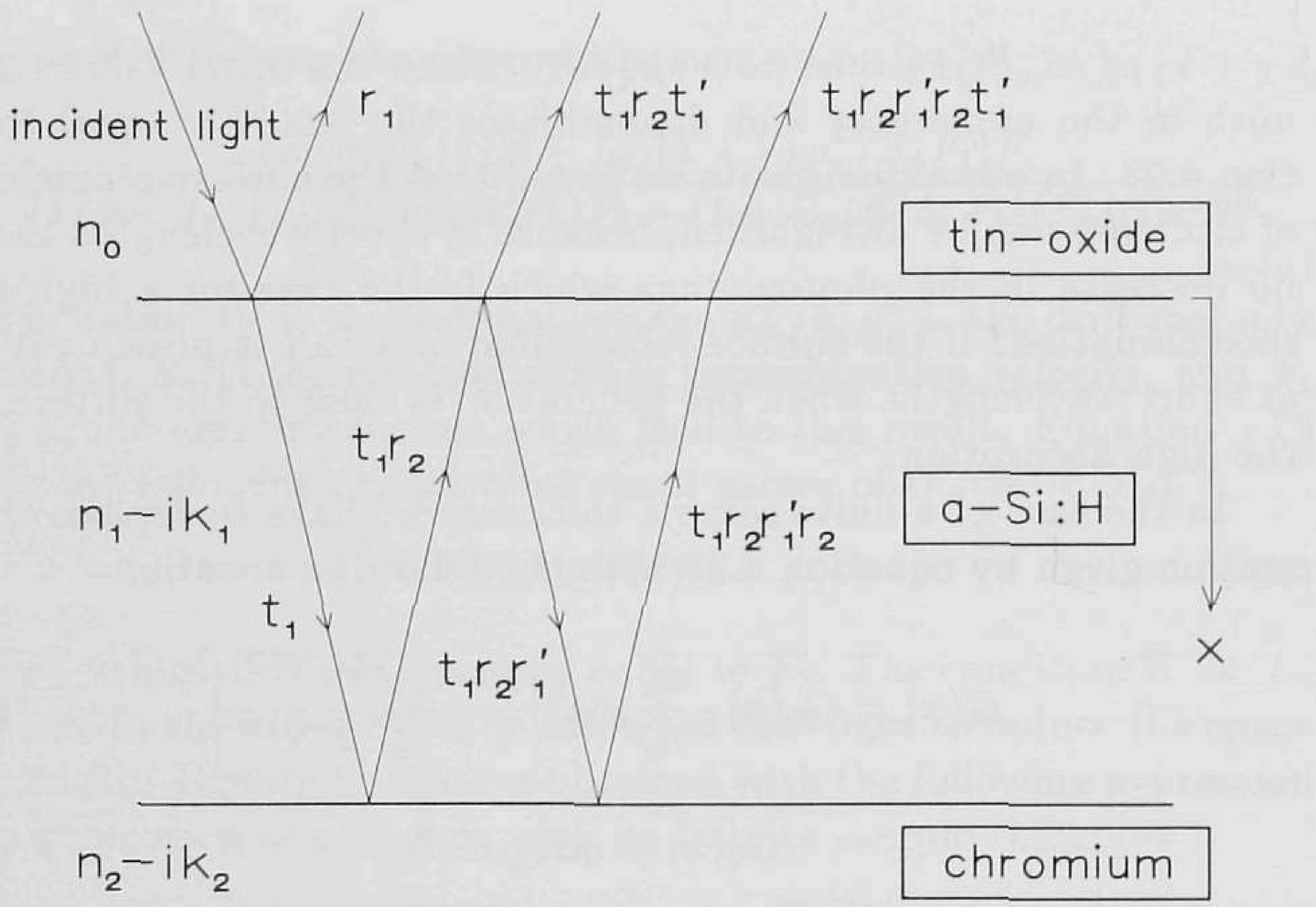

Figure 4.3: The optical system that was used to calculate the generation. The arrows indicate the light rays which are transmitted and reflected at the interface between the different media.

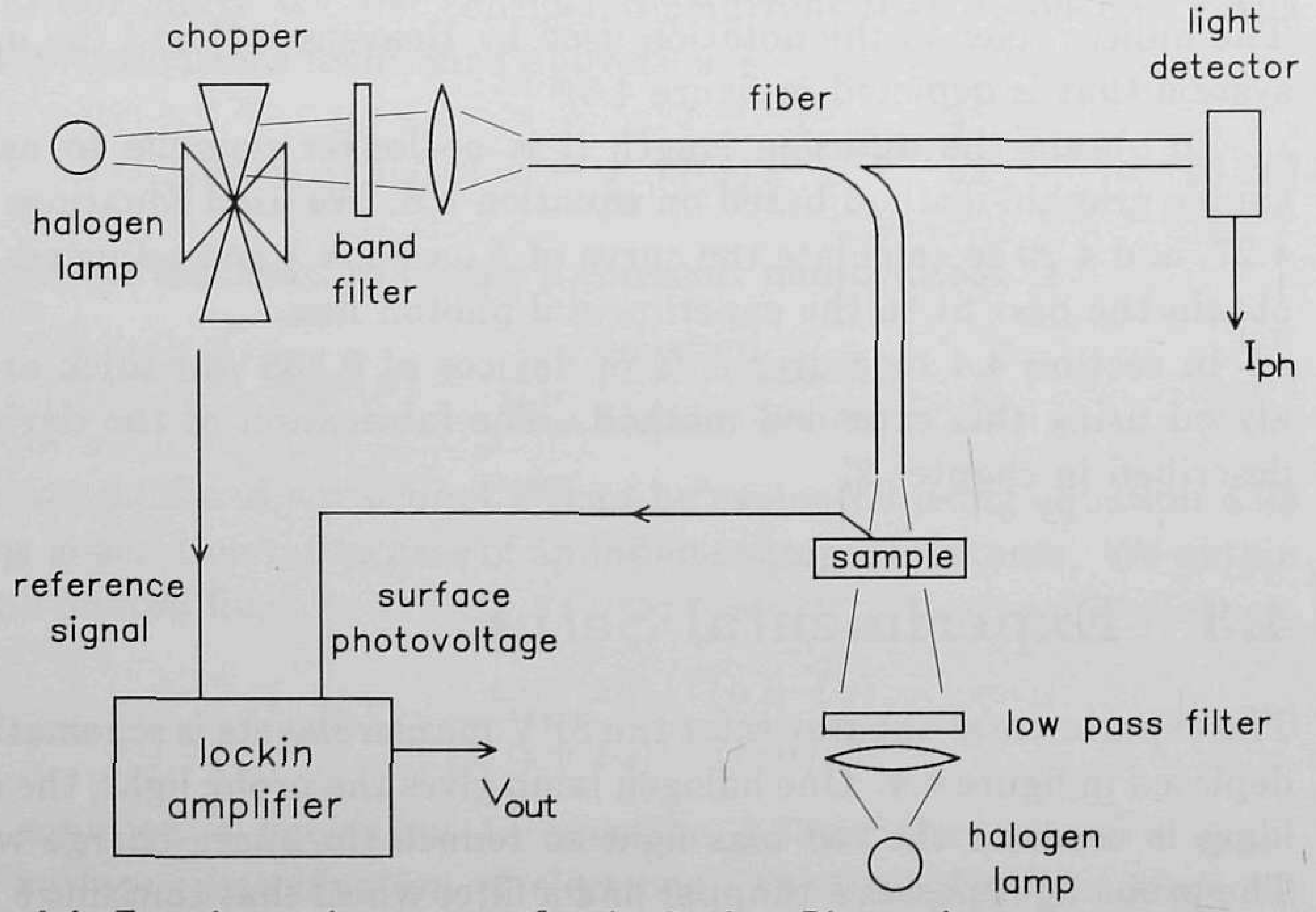

Figure 4.4: Experimental apparatus for the Surface Photovoltage measurements.

with a bandwidth at half maximum of 10 nm and with a maximum transmission for the wavelengths: 520, 540, 560, 580, 600, 620, 640, and 660 nm. The probe light is focussed at the fiber bundle that is split up into two bundles, one goes to an EG&G HUV 1100BQ silicon photodiode, the other goes to the sample. The red bias light is obtained by filtering the light of the halogen lamp with an ORIEL 51540 low pass transmission filter (transparent for long wavelengths) with a 50% transmission at 695 nm.

The generated photovoltage is measured by a PAR model 126 lock-in amplifier. The measurement frequency was 20 Hz which is determined by the chopper that generates a reference signal used by the lock-in amplifier to lock its internal reference frequency. The output of the lock-in amplifier, which is proportional to the surface photovoltage, was monitored by an external digital voltmeter.

We used the following procedure to measure the diffusion length. The surface photovoltage was held constant by adjusting the lamp voltage. Both the lamp voltage and the band filters were changed manually. The photon flux was obtained from the silicon photodetector which gave a voltage proportional to the photon flux in this wavelength region. The absorption coefficient α and the layer thickness d were obtained from the optical reflection and transmission of samples deposited in the same run on an uncoated Corning 7059 glass substrate. The diffusion length was obtained from the plot of the photon flux I_{ph} versus $(1/\alpha)$.

This procedure was repeated for several intensities of red bias light until the diffusion length did not change after an increase of intensity. The short-circuit current I_{sc} of the sample under bias light illumination was measured by an HP 4145B Parameter Analyzer. The I_{sc} was used to control the increase of bias light intensity, and the procedure we used was to increase the intensity so that the I_{sc} doubled and to repeat the diffusion length measurement.

4.4 Results in the Case of Thin Layers

In this section two experimental methods to obtain the photon flux as a function of the wavelength were used. In the first method we used

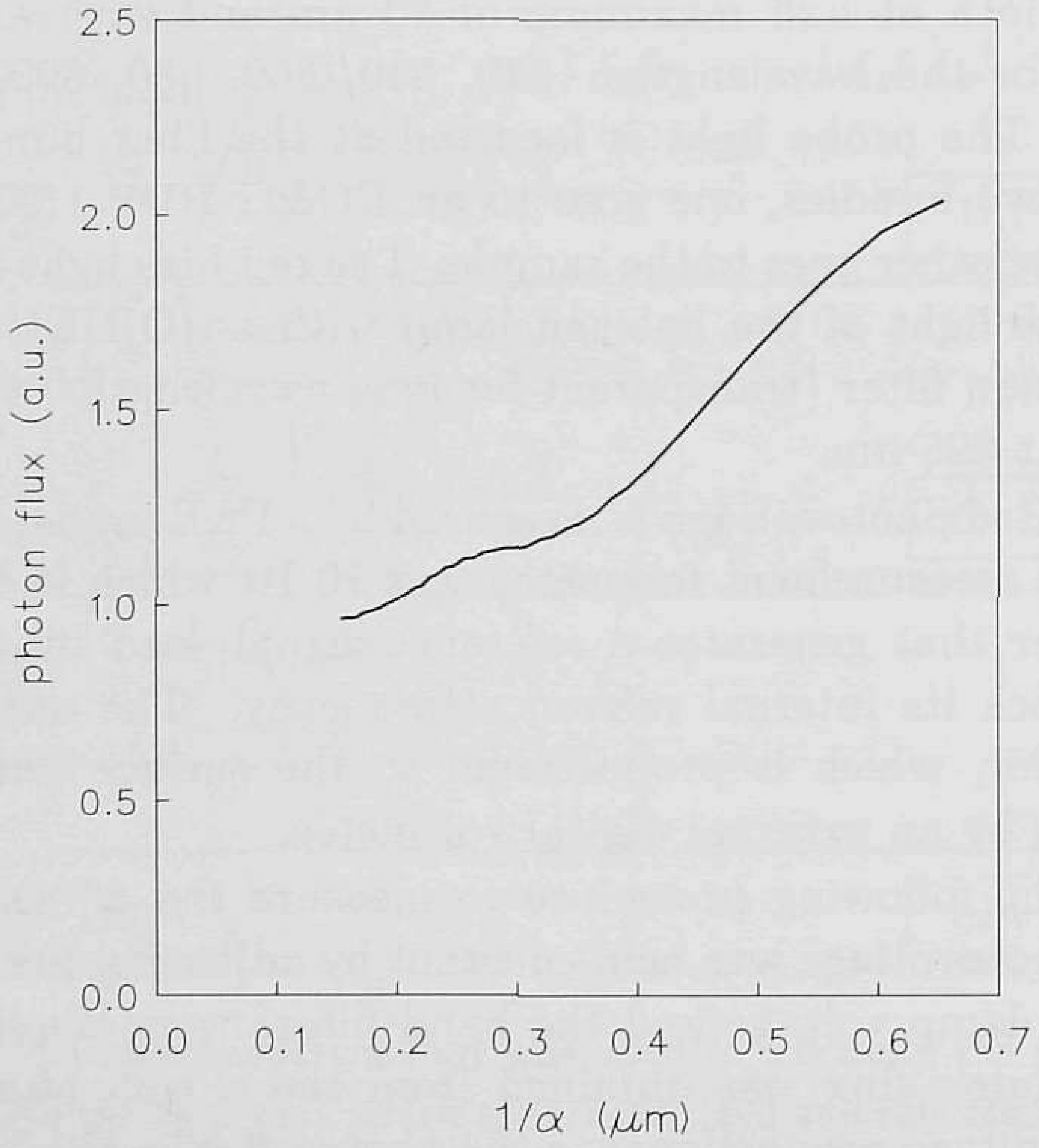

Figure 4.5: The "Goodman" plot of the measured photon flux versus the reciprocal absorption of the a-Si:H.

a monochromator to obtain monochromatic light in the wavelength region between 550 nm and 640 nm. The short-circuit current was held constant by adjusting the photon flux. In the second method we used a set of interference filters with wavelengths of 520, 560, 600, 620, and 640 nm with a bandwidth of 10 nm. In this measurement the photovoltage was held constant by adjusting the photon flux.

The photon flux versus the reciprocal absorption is shown in figure 4.5. These values were obtained by keeping the short-circuit current constant while changing the wavelength of the light. The interference effects caused by the reflection from the back contact can be easily seen. In figure 4.6 the calculated generation is shown as a function of position in the layer for a wavelength of 590 nm and a wavelength of 610 nm. The shift in the position of the peaks causes the interference effects in the photon flux. We used equations 4.26, 4.27, and 4.29 to calculate the photon flux. As can be seen from figure 4.7 the calculated curve for a diffusion length of 0.12 μm and a space-charge width of 0.19 μm agrees well with the measured curve. However, there are many combinations of a diffusion length and a space charge width that give a good fit to the measured curve. For example, a space charge width of 0.16 μm and a diffusion length of 0.15 μm also give a good fit. Therefore, red bias light was used, as suggested by Moore [12], to reduce the space charge width.

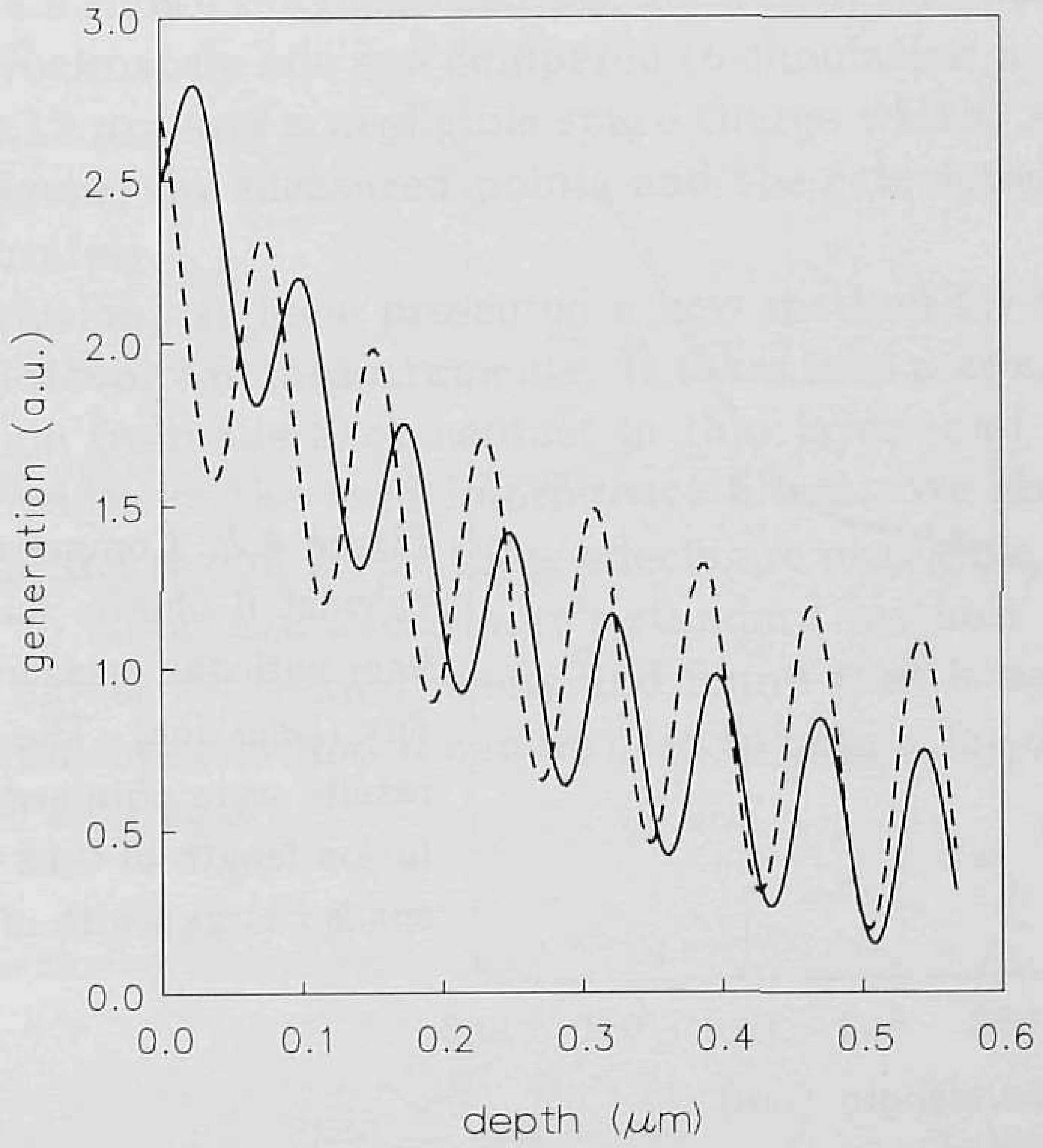

Figure 4.6: Calculated generation as a function of position in the a-Si:H layer. The solid curve corresponds to a wavelength of 590 nm, the dashed curve to a wavelength of 610 nm.

To obtain a sufficient intensity of the probe light in the case of bias light, a set of interference filters was used with a bandwidth of 10 nm instead of a monochromator. The bandwidth was taken into account by adding the calculated generation of several wavelengths within the bandwidth. This is an advantage of our method over that of Moore since it is not possible to account for a deviation from monochromatic light in equation 4.23.

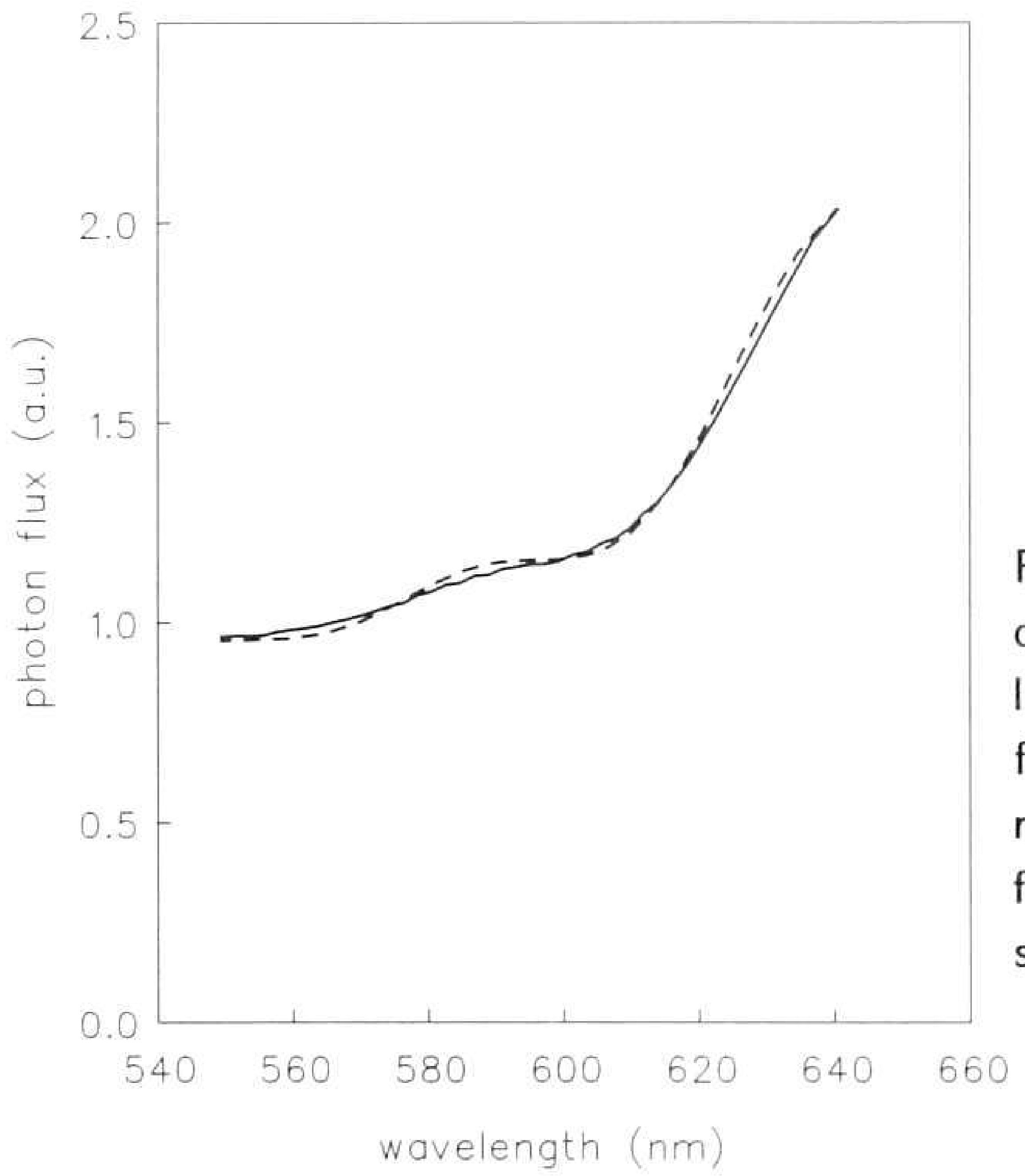

Figure 4.7: Comparison of the calculated photon flux (dashed line) with the measured photon flux (solid line). The calculated results were obtained for a diffusion length of 0.12 μm and a space charge width of 0.19 μm.

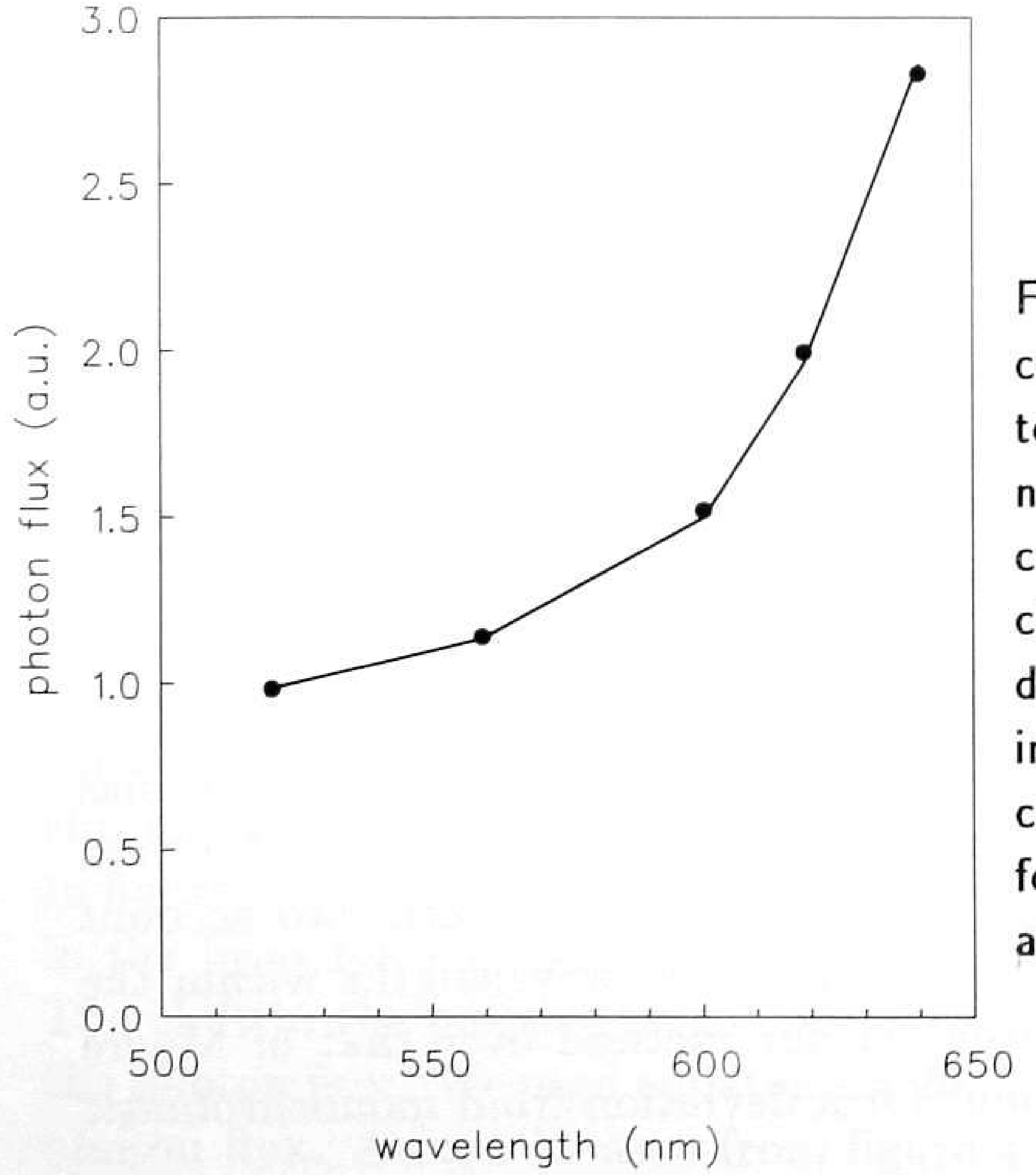

Figure 4.8: Comparison of the calculated and measured photon flux for light obtained from narrow band pass filters. The calculated data are indicated by closed circles, the experimental data by a solid line connecting the measured points. The calculated results were obtained for a diffusion length of 0.12 μm and no space charge width.

Figure 4.8 shows the measured photon flux at a red bias light intensity of approximately one sun compared to simulation using a diffusion length of 0.12 μm and a negligible space-charge width. As can be seen from the figure, the measured points and the calculated points correspond accurately.

In conclusion, we have presented a new method for the analysis of Surface Photovoltage measurements. It takes into account the effect of the reflection from the back contact in thin layers and the effect of a finite bandwidth of the used interference filters. We showed theoretically that in the region where these effects are negligible this method is equivalent to Goodman and Moore's standard method. We also compared the model with experiments and found that it agrees well with the measurements and that it can be used to obtain the diffusion length of a-Si:H in thin layers.

4.5 Schottky Barriers at the Substrate Interface

In this section the effect of the substrate on the diffusion length and on the quality of the diode is studied. The properties of the material close to the substrate can differ substantially from the properties of the bulk of the material. This can be caused by the deposition process itself as has been shown by ellipsometry [7] or by diffusion of impurities from the substrate [8]. We made diodes with the Schottky barrier at the substrate/a-Si:H interface to study these effects. We used current-voltage (I-V) measurements to obtain the ideality factor and used the SPV technique to obtain the diffusion length. The diffusion length as determined by the SPV technique measures the material close to the substrate (with a characteristic distance equal to the diffusion length). But the SPV technique is much less sensitive to interface states compared to the parameters of the Schottky barrier (as obtained from I-V measurements). By comparing the diodes on tin-oxide and chromium coated substrates we tried to measure the influence of the diffusion of tin [9] on the current-voltage characteristics and on the diffusion length.

4.5.1 Sample Preparation

As substrates we used chromium coated glass and tin-oxide coated glass. The thin chromium layers on Corning 7059 glass were made by evaporation. A thickness of 60 Å was used with a transparency of 40% for the light used in the SPV technique. For the tin-oxide coated glass commercially available coated glass (Corning) with a sheet resistance of the tin-oxide layer of 100 $\Omega/\square$ was used.

First an intrinsic layer was deposited on the substrates. The thickness of the intrinsic layer ranged from 1.5 to 2.5 μm. After the intrinsic layer an n-doped layer of 500 Å was deposited. The samples were then removed from the reactor chamber and ohmic contacts were made on top by evaporation of chromium and photolithography. Details of the fabrication of the a-Si:H layers can be found in chapter 2.

We did six deposition runs and with three runs we used the shutter in the reactor. The shutter was used to shield the substrates from the glow discharge plasma during the ignition of the plasma. After 1 minute it was assumed that the plasma had stabilized and the shutter was removed.

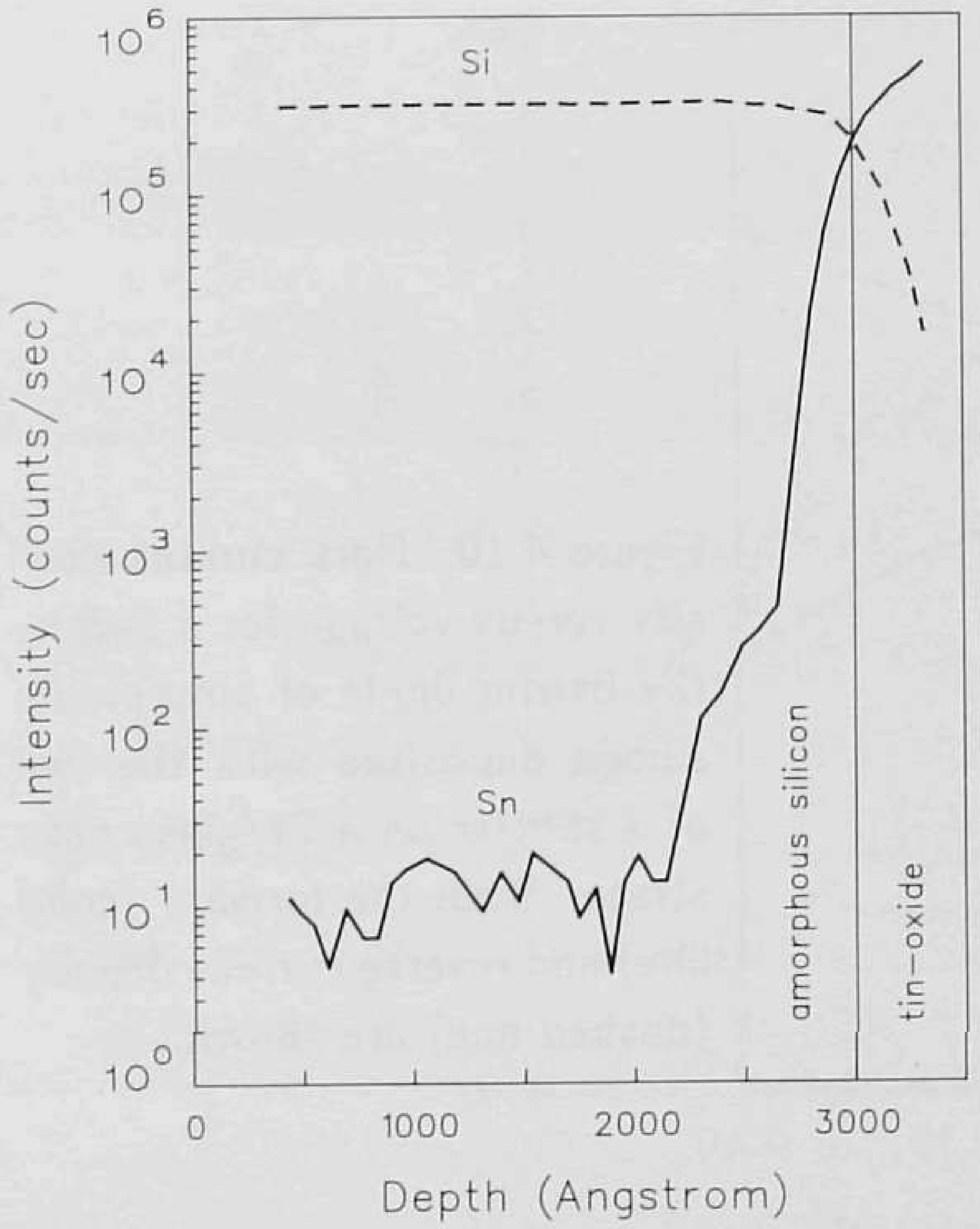

Figure 4.9: Silicon and tin profiles obtained by SIMS of an a-Si:H/SnO$_2$ interface. The silicon profile is indicated by the dashed line, and the tin profile is indicated by the solid line.

4.5.2 Secondary Ion Mass Spectroscopy

Secondary Ion Mass Spectroscopy (SIMS) was used to measure the diffusion of tin into the amorphous silicon layer. The principle of this technique is that a sputtering beam of ions with high energy removes the atoms from the surface of the sample layer (this process is called sputtering). These atoms (in the form of ions) are detected with a mass spectrometer. Because the sputter beam removes the atoms from the surface and the layer thickness decreases, the detected ions versus the sputter time give a depth profile of the layer.

In figure 4.9 the contamination of the a-Si:H layer with tin as determined by SIMS is shown. It can be seen in the figure that there is a tin tail that goes as deep as 700 Å into the a-Si:H.

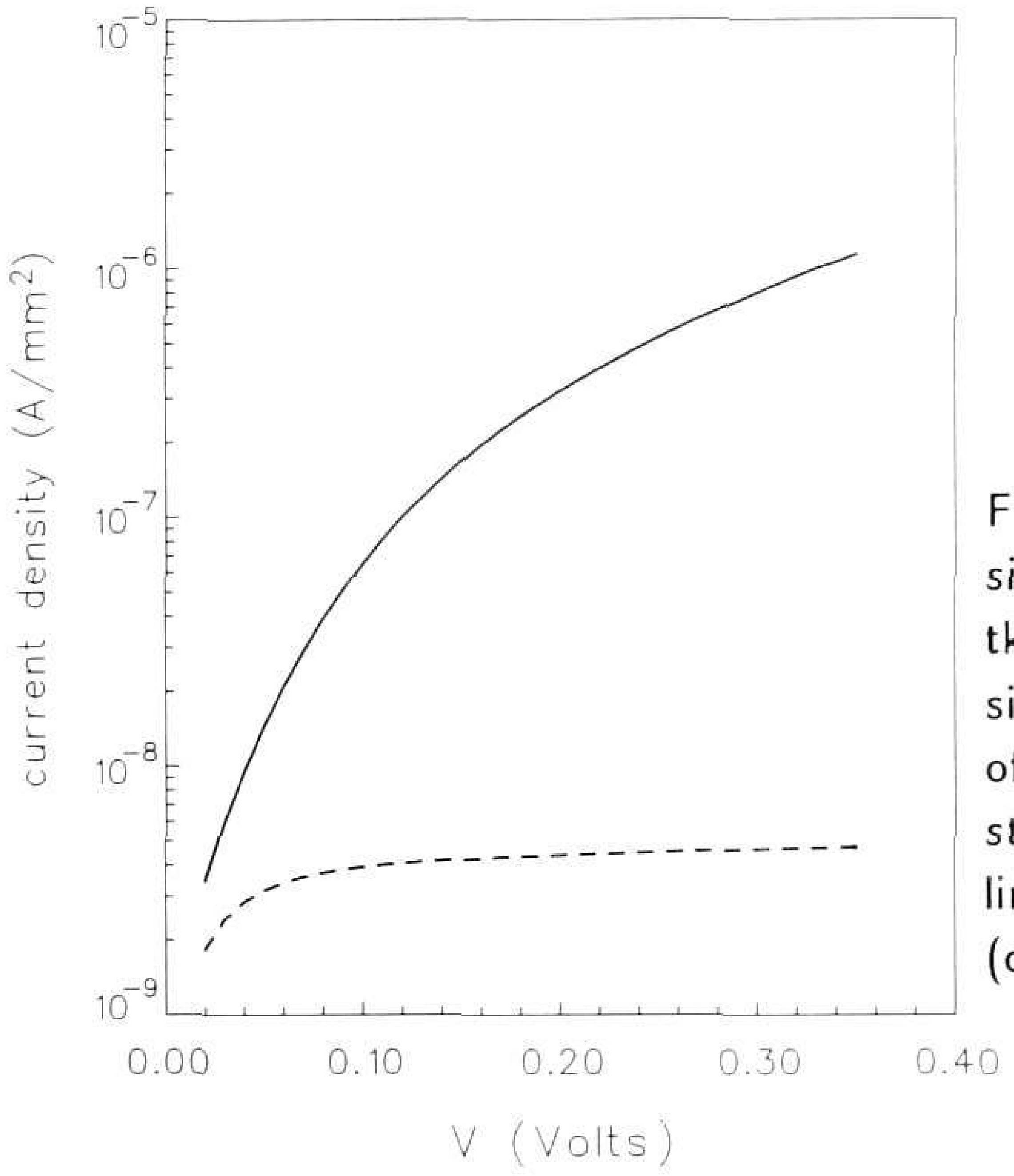

Figure 4.10: Dark current density versus voltage for a Schottky barrier diode of amorphous silicon deposited with the use of a shutter on a Cr/glass substrate. Both the forward (solid line) and reverse current density (dashed line) are shown.

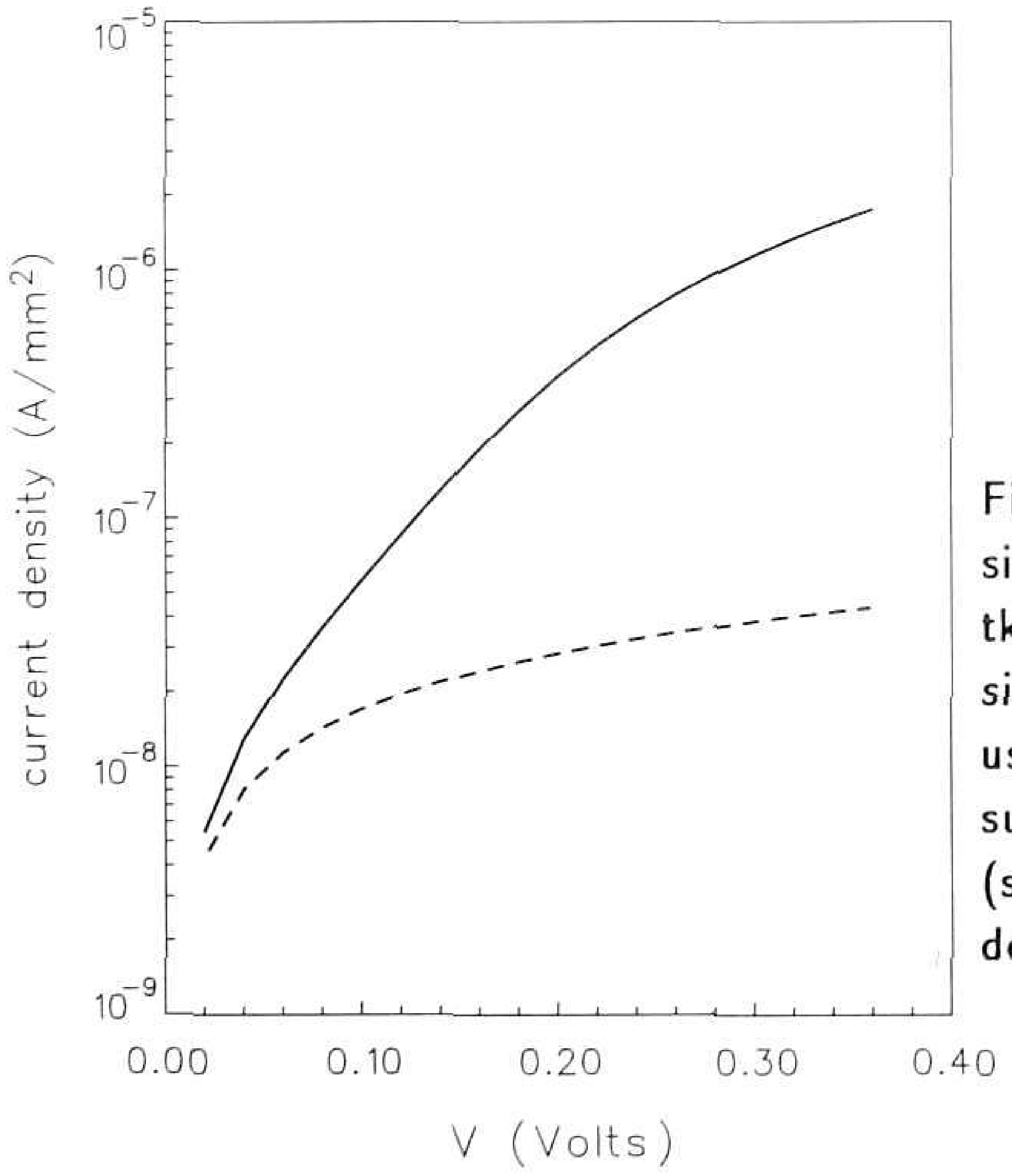

Figure 4.11: Dark current density versus voltage for a Schottky barrier diode of amorphous silicon deposited without the use of a shutter on a Cr/glass substrate. Both the forward (solid line) and reverse current density (dashed line) are shown.

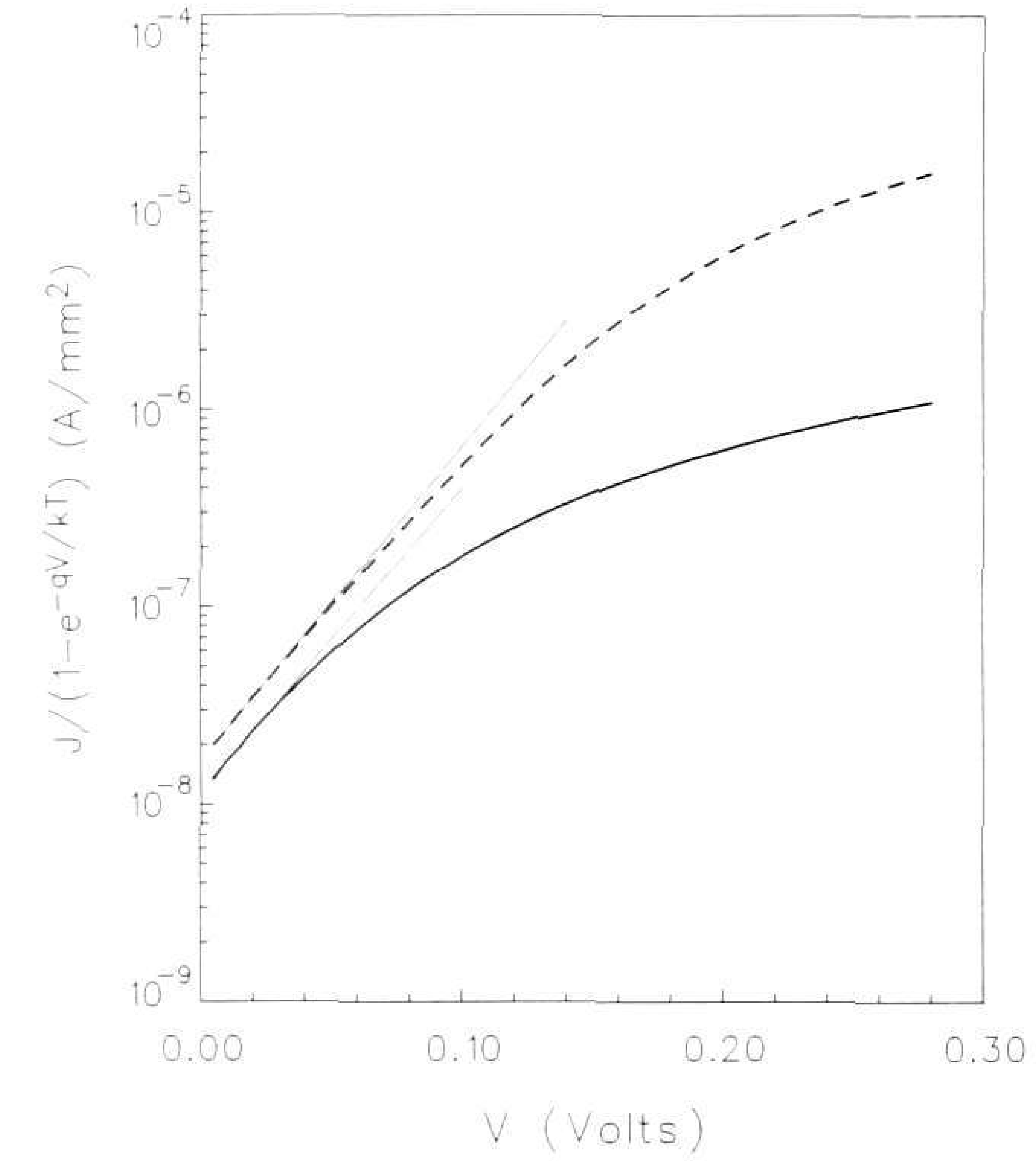

Figure 4.12: Forward current density divided by $[1 - e^{-qV/kT}]$ versus voltage for a Schottky barrier of amorphous silicon deposited with the use of a shutter on a Cr/glass substrate. The solid line is the dark current density, the dashed line is the current density with a low intensity bias light of 700 Å. The slope of the straight lines is used to obtain the ideality factor.

4.5.3 Current-Voltage Measurements

The J-V characteristics of the diodes on Cr/glass substrates deposited with and without the use of a shutter are shown in figure 4.10 and figure 4.11. The ideality factor of the diodes was estimated graphically using the following equation at low voltages [19]

$$J = J_0\, e^{qV/nkT}\left[1 - e^{-qV/kT}\right] , \tag{4.30}$$

where J_0 is the saturation current density. The plot of the log of $J/[1 - e^{-qV/kT}]$ versus V gave a straight line for voltages as low as 2 mV, the ideality factor was obtained from the slope of the plot [19].

To reduce the series resistance, low intensity red light of 700 nm

Table 4.1: Diode parameters obtained from J-V measurements for the different diode types.

substrate	ideality factor	J at $1V$ reverse bias nA/mm^2
	deposited using a shutter	
Cr/glass	1.17	8
SnO_2/glass	1.15	0.6
	deposited without a shutter (variation caused by different deposition runs)	
Cr/glass	1.56	40
Cr/glass	1.79	100
SnO_2/glass	1.76	20
SnO_2/glass	2.4	600

with uniform absorption throughout the layer was used. The ideality factor was obtained at higher voltages from the slope of the plot of the log of J versus V. This method gave results comparable with the one above. This is illustrated by figure 4.12 where the two methods are compared.

The values of n are listed in table 4.1. The diodes made without a shutter have a higher ideality factor and a higher reverse current density as can be seen in table 4.1. The values of n and the reverse current varied between depositions when no shutter was used. With an increasing value of n the reverse characteristic shows a dramatic increase in the current. There is no dependence of n on the used substrate (i.e. chromium or tin-oxide) for either deposition procedure (with and without using a shutter).

The J-V characteristics were measured in the temperature interval 300–360 K. According to the thermionic emission theory the saturation current density is given by

$$J_0 = A^* T^2 e^{-\phi/kT} , \tag{4.31}$$

where A^* is the Richardson constant and ϕ is the barrier height. When the current is diffusion limited it is given by

$$J_0 = q\mu_n N_c \mathcal{E}_S \, e^{-\phi/kT} , \tag{4.32}$$

where μ_n is the electron mobility, N_c is the effective density of states in the conduction band and $\mathcal{E}_S$ is the surface electric field in the semiconductor [20].

We used a diode on a SnO_2/glass substrate with an ideality factor of 1.15. The barrier height for the case of thermionic emission was obtained from the slope of the plot of $\ln J_0/T$ versus $1/T$. For the case of diffusion limited current the barrier height was obtained from the slope of the plot of $\ln J_0$ versus $1/T$. In this temperature interval both plots gave a straight line and yielded a barrier height of 0.8 eV and 0.75 eV respectively. The value of 0.8 eV for SnO_2 (for the case of thermionic emission) is equal to the value reported in literature when the tin-oxide was evaporated on top of the a-Si:H layer [21].

4.5.4 Surface Photovoltage Measurements

The diodes were illuminated from the substrate side with monochromatic light, and the light intensity at each wavelength was adjusted to give a constant photovoltage. The diffusion length was obtained from the intercept on the $1/\alpha$ axis of the straight line in the plot of I_{ph} versus $1/\alpha$. The values of α and the layer thickness were obtained from the reflection and transmission of i-n structures deposited on Corning 7059 glass substrates in the same run as the corresponding diodes.

The diffusion length obtained in this way was 0.25 μm for both the diodes on Cr/glass and on SnO_2/glass substrates. The use of a shutter did not influence the diffusion length. This diffusion length when compared to values in the literature is of an average value. A diffusion length of 0.8 μm has been obtained in excellent material and 0.1 μm or smaller is found in material of inferior quality [22]. Space Charge Limited Current measurements done on n-i-n structures deposited under the same conditions with the same intrinsic layer thickness show a density of states of 3×10^{16} cm^{-3}eV^{-1} and this value indicates good material. A possible explanation for the moderate diffusion length could be our reversed configuration. To our knowledge, this is the first time that this method has been used to measure the diffusion length of the material near the substrate, the material that is used for solar cells and thin film transistors.

4.5.5 Discussion

In a Schottky barrier the rectifying behaviour is caused by a potential barrier that arises from stable space charges in the semiconductor. These stable space charges can be caused by donor atoms in the semiconductor or in the case of amorphous silicon by localized states in the gap [23].

About the origin of the Schottky barrier several models have been considered. The classical model suggests that the barrier height reflects the difference of the metal work function and the electron affinity of the semiconductor. An alternative model is that the band bending is determined by surface states. There is no definite model for crystalline silicon or for amorphous silicon. The barrier height depends on the metal work function but the unmodified work function model cannot be applied. There is, however, evidence that barrier heights of several metals on a-Si:H parallel those of crystalline silicon [20]. The J-V characteristics are determined by the density of states in the gap of the amorphous silicon layer. The states in the gap influence the forward characteristic by increasing the recombination current and thereby increasing the ideality factor [24]. The reverse current is increased by these states because in this regime they serve as generation centers. When there is a very large density of states in the gap, tunnelling through the barrier will become an important mechanism and will dominate the reverse current [25].

The SPV measurement is also determined by the density of states in the gap because these states determine the lifetime of the carriers through recombination. In section 4.2 the following expression for the diffusion length of a-Si:H was obtained

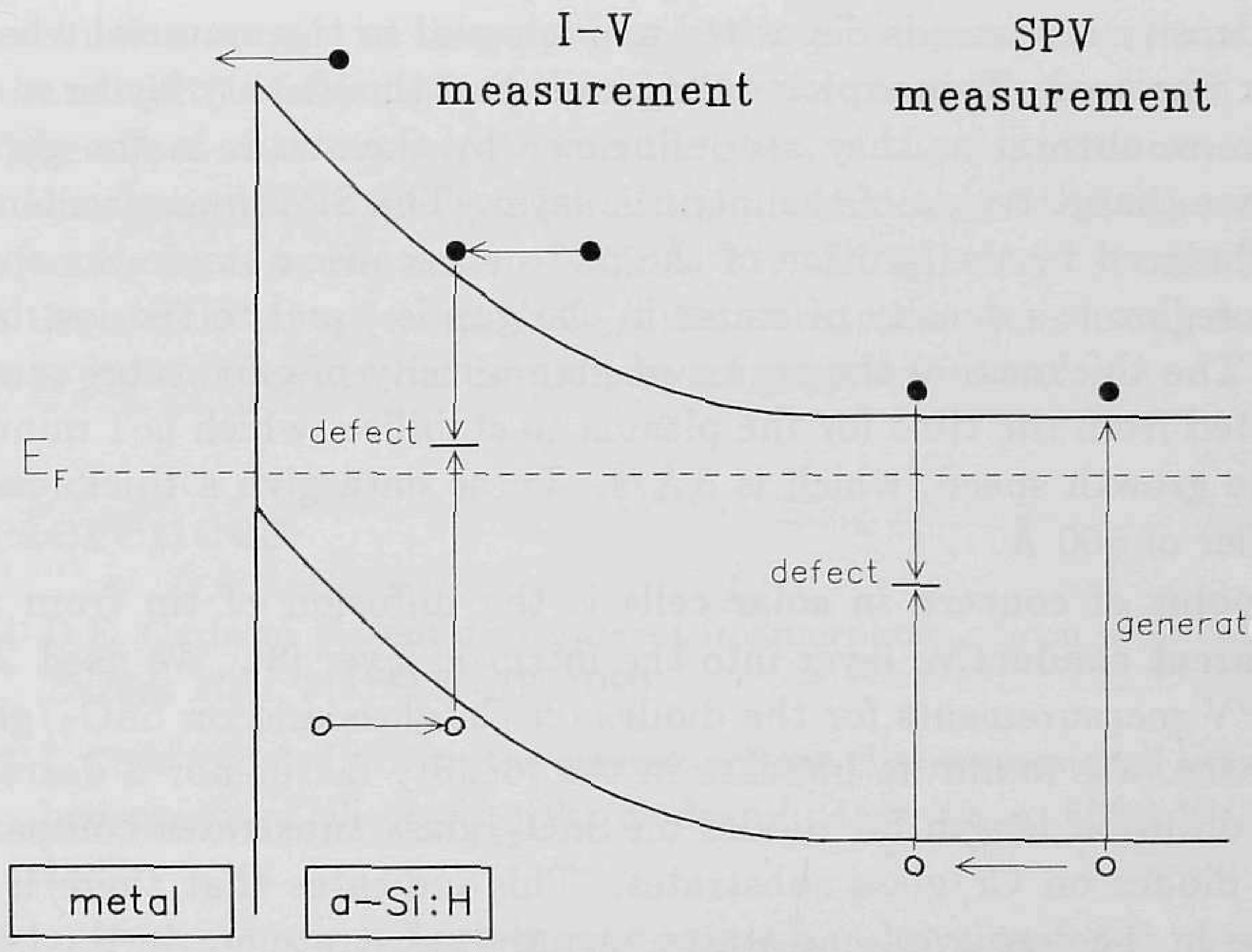

Figure 4.13: The recombination path for the diode in forward bias, and the recombination path in the SPV measurement.

$$L_d = \sqrt{\frac{2kT}{q}\mu_p^d(\tau_p + \tau_n)} \tag{4.33}$$

The density of states in the gap determines the lifetimes τ_p and τ_n, and thereby L_d.

In the SPV measurement a hole-electron pair is generated far from the interface so the recombination takes place outside the space-charge region. In the J-V measurements the recombination takes place inside the space charge region so the two measurements are determined by the density of states in the gap at different places in the intrinsic layer. These two recombination paths are illustrated in figure 4.13. A position dependent density of gap states can explain the difference in the J-V characteristics for diodes deposited with or without using a shutter while the diffusion length is not influenced.

At the time of the ignition of the plasma a layer with a high density of states is deposited. After stabilization of the plasma, material with a low density of states is deposited and is equal to the material when a shutter was used. This explains the increase of the ideality factor n and the reverse current as they are influenced by the states in the gap in the space charge region of the intrinsic layer. The SPV measurement is not influenced by the ignition of the plasma because outside the space charge region the density of states in the gap is equal to the low bulk value. The thickness of the region of high density of gap states can be estimated from the time for the plasma to stabilize, which is 1 minute, and the growth speed, which is 5 Å/s. These data give a thickness in the order of 300 Å.

A point of concern in solar cells is the diffusion of tin from the transparent conductive layer into the intrinsic layer [8]. We used J-V and SPV measurements for the diodes on Cr/glass and on SnO_2/glass substrates. We found no increase in the ideality factor nor a decrease in the diffusion length for diodes on SnO_2/glass substrates compared to the diodes on Cr/glass substrates. This indicates that there is no increase in the density of gap states near the substrate nor in the bulk. Therefore, it must be concluded that the tin tail extending 700 Å deep into the a-Si:H layer does not have a large influence on the density of gap states.

4.6 Conclusions

The Surface Photovoltage (SPV) Technique measures the ambipolar diffusion length of undoped a-Si:H. The ambipolar diffusion length consists of the mobility and lifetime of both holes and electrons. Because the electron mobility is much higher than the hole mobility, there is an electric field caused by the difference in hole and electron concentrations. This electric field causes a hole drift current that is of the same order of magnitude as the hole diffusion current. The drift current assists the diffusion current and increases the measured diffusion length by a factor $\sqrt{2}$ compared to the situation with diffusion alone.

We have demonstrated the use of an extended method to obtain the diffusion length from the photon flux I_{ph} versus the absorption coefficient α. The method is based on the calculated generation instead of on an analytic expression. With this method it is possible to measure the diffusion length in thin devices. It is also possible to incorporate the bandwidth of the light if the light is not monochromatic [6].

The effect of the substrate and the start of the deposition was studied. We showed that the ignition of the plasma causes the deposition of a defective layer in the order of 300 Å. The tin tail that extended 700 Å into the a-Si:H layer (when SnO_2/glass substrates were used) does not have a great influence on the density of gap states [26].

References

[1] D.E. Carlson. Recent development in amorphous silicon solar cells. *Sol. Energy Mat.*, 3(4):503–518, 1980.

[2] I. Chen and S. Lee. On the current-voltage characteristics of amorphous hydrogenated silicon schottky diodes. *J. Appl. Phys.*, 53(2):1045–1051, 1982.

[3] A. Deneuville and M.H. Brodsky. Influence of preparation conditions on forward-bias currents of amorphous silicon diodes. *J. Appl. Phys.*, 50(3):1414, 1979.

[4] L. Mariucci et al. Effects of tunneling on a-Si:H schottky barriers. *J. Appl. Phys.*, 62(8):3285–3287, 1987.

[5] C.R. Wronski, D.E. Carlson, and R.E. Daniel. Schottky-barrier characteristics of metal-amorphous-silicon diodes. *Appl. Phys. Lett.*, 29(9):602–605, 1976.

[6] J.C van den Heuvel, R.C. van Oort, and M.J. Geerts. Diffusion length measurements of thin amorphous silicon layers. *Solid State Comm.*, 69(8):807–810, 1989.

[7] A.M. Antoine, B. Drevillon, and P. Roca i Cabarrocas. In situ investigation of the growth of rf glow-discharge deposited amorphous germanium and silicon films. *J. Appl. Phys.*, 61(7):2501–2515, 1987.

[8] M. Kitagawa, K. Mori, S. Isihara, M. Ohno, T. Hirao, Y. Yoshioka, and S. Kohiki. Interaction of hydrogenated amorphous silicon films with transparent conductive films. *J. Appl. Phys.*, 54(6):3236–3271, 1983.

[9] A.M. Antoine and B. Drevillon. Influence of the substrate on the early stage of the growth of hydrogenated amorphous silicon evidenced by kinetic ellipsometry. *J. Appl. Phys.*, 63(2):360–367, 1988.

[10] A. Goodman. A method for the measurement of short minority carrier diffusion lengths in semiconductors. *J. Appl. Phys.*, 32(12):2550–2552, 1961.

[11] A.R. Moore. Theory and experiment on the surface-photovoltage diffusion-length measurement as applied to amorphous silicon. *J. Appl. Phys.*, 54(1):222–228, 1983.

[12] A.R. Moore. *Semiconductors and Semimetals*, chapter 7, pages 239–256. Volume 21C, Academic Press, London, 1984.

[13] S.S. Hegedus, H.S. Lin, and A.R. Moore. Light-induced degradation in undoped hydrogenated amorphous silicon films studied by the surface photovoltage technique: a comparison of lifetime versus space-charge effects. *J. Appl. Phys.*, 64(3):1215–1219, 1988.

[14] P.J. McElheny, J.K. Arch, and S.J. Fonash. Assessment of the surface-photovoltage diffusion-length measurement. *Appl. Phys. Lett.*, 51(20):1611–1613, 1987.

[15] P.J. McElheny, J.K. Arch, H.S. Lin, and S.J. Fonash. Range of validity of the surface-photovoltage diffusion length measurement: a computer simulation. *J. Appl. Phys.*, 63(3):1254–1265, 1988.

[16] A. Rothwarf and K.W. Boer. Direct conversion of solar energy through photovoltaic cells. *Prog. Solid State Chem.*, 10:71–102, 1975.

[17] J. Reichman. Collection efficiency of low-mobility solar cells. *Appl. Phys. Lett.*, 38(4):251–253, 1981.

[18] O.S. Heavens. *Optical Properties of Thin Solid Films.* Butterworths, London, 1955.

[19] E.H. Rhoderick. *Metal-Semiconductor Contacts*, page 87. Clarendon Press, Oxford, 1980.

[20] C.R. Wronski and D.E. Carlson. Surface states and barrier heights of metal-amorphous silicon schottky barriers. *Solid State Comm.*, 23(7):421–424, 1977.

[21] N. Brutscher and M. Hoheisel. Schottky diodes with high series resistance: a simple method of determining the barrier heights. *Solid State Electron.*, 31(1):87–89, 1988.

[22] B. Faughan, A.R. Moore, and R.S. Crandall. Relationship between collection length and diffusion length in amorphous silicon. *Appl. Phys. Lett.*, 44(6):613–615, 1984.

[23] W. Schottky. Halbleitertheorie der sperrschicht. *Naturwissenschaften*, 26:843, 1938.

[24] E.H. Rhoderick. *Metal-Semiconductor Contacts*, page 105. Clarendon Press, Oxford, 1980.

[25] E.H. Rhoderick. *Metal-Semiconductor Contacts*, page 111. Clarendon Press, Oxford, 1980.

[26] J.C. van den Heuvel, R.C. van Oort, M.J. Geerts, B. Bokhorst, and J.W. Metselaar. Influence of the defect density of amorphous silicon at the substrate interface on the schottky barrier characteristics. In *15th International Conference on Defects in Semiconductors*, 1988.

Chapter 5

Space Charge Limited Current Measurements

5.1 Introduction

The Space Charge Limited Current (SCLC) technique is widely used to obtain the density of states in the gap of intrinsic hydrogenated amorphous silicon (a-Si:H). The principle of this technique is that a device with an injecting contact is used and the opposite contact blocks the carriers with opposite polarity. In this case a space charge builds up in the intrinsic a-Si:H at voltages above a certain threshold voltage. We used n-i-n a-Si:H devices and in this case the space charge consists of electrons which are trapped by states in the bandgap [1].

The space charge results in a deviation from the linear current-voltage (*I*-*V*) characteristics of the Ohmic regime. A typical *I*-*V* curve of an n-i-n device is depicted in figure 5.1. Because the space charge consists of electrons that are trapped by gap states, the *I*-*V* characteristics can be used to obtain the density of these gap states. The method to obtain the density of gap states from the *I*-*V* characteristics is described in section 5.2.

It is believed that in the high electric field regime Poole-Frenkel emission could affect the density of gap states measurements [2,3]. We investigated the relevance of the Poole-Frenkel effect for SCLC measurements of n-i-n a-Si:H devices. If an electron is trapped by a positive charged defect, then the effective barrier for the electron to escape will be lowered by a high electric field [4,5]. This is called the Poole-Frenkel (PF) effect. It results in a lower space charge and the calculated density of gap states using the standard SCLC theory is too low. We will show

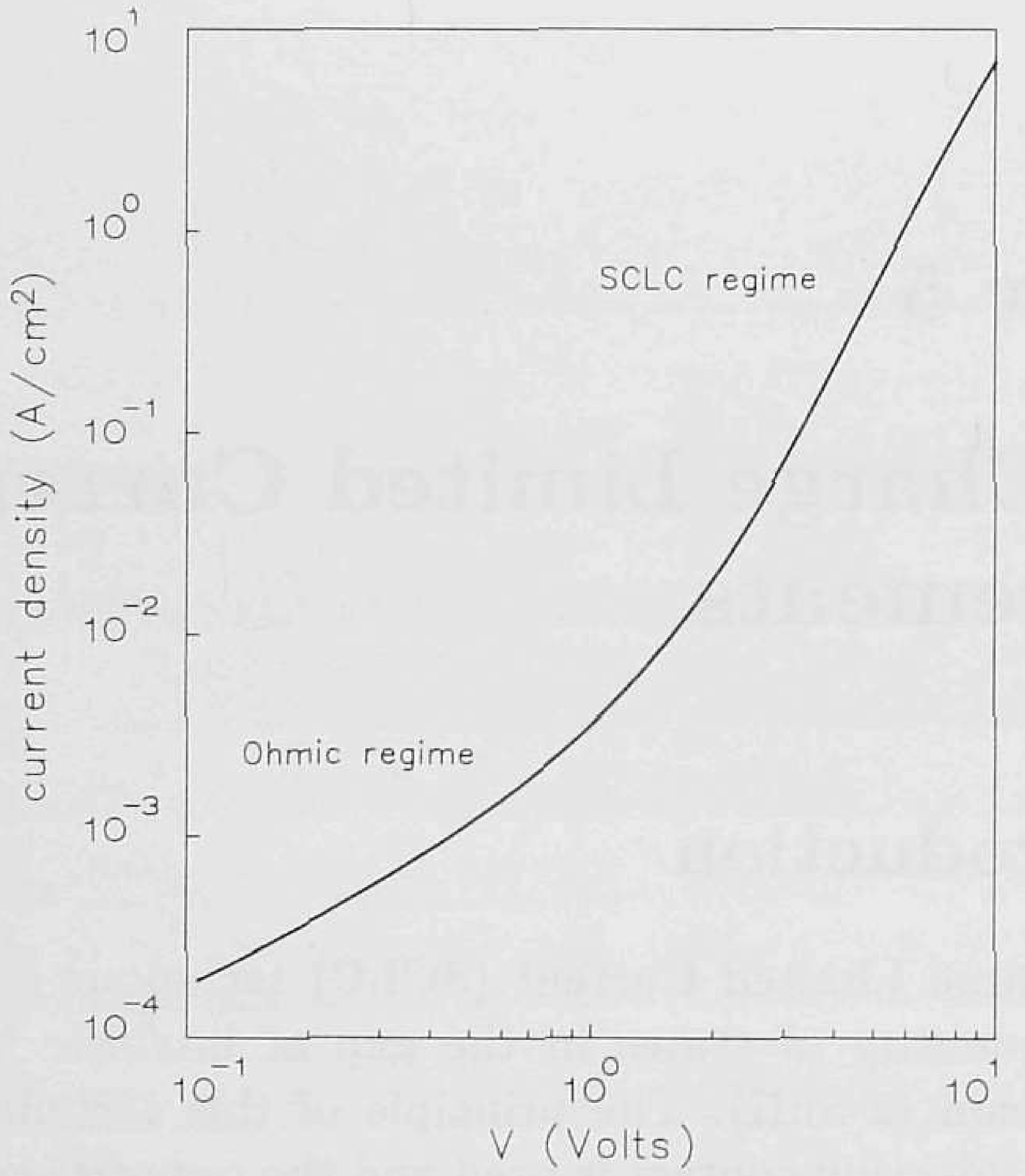

Figure 5.1: A typical *I-V* curve of an n-i-n device.

in section 5.4 that the PF effect is absent in n-i-n a-Si:H devices [6].

We measured the current-voltage (*I-V*) characteristics of n-i-n a-Si:H devices with intrinsic layer thicknesses of 0.7, 1.5, and 3.0 μm at temperatures between 170 K and 340 K. The *I-V* measurements were analyzed using the step-by-step method developed by den Boer [7] to obtain the density of gap states. We modified the step-by-step method to obtain the density of gap states in the case of PF emission. These two densities of gap states were compared. From this comparison we concluded that the PF effect is absent.

We also studied the characteristic temperature which is based on the concept that the distribution of gap states is exponential. The characteristic temperature is obtained from the slope of $\ln(I)$ versus $\ln(V)$ in the SCLC regime. This method requires high electric fields. Because of the high fields the measurement of the characteristic temperature is very sensitive to the PF effect. No PF effect on the characteristic temperature was found, and this confirms the conclusion that the PF effect is absent.

The density of gap states and the characteristic temperature show a large temperature dependence. A computer simulation was developed to simulate the *I-V* curves of n-i-n a-Si:H devices. With the use of these simulations it will be shown that the temperature dependence of the density of gap states and the characteristic temperature is a result of the conduction band tail.

5.2 Theory of the SCLC Measurements

5.2.1 The Step-by-Step Method

In this subsection the step-by-step method is described that will be used to obtain the density of gap states from current-voltage measurements. This method is valid under the following conditions:

1. Quasi-equilibrium exists.
2. Double injection does not occur or is negligible.
3. Diffusion currents are negligible.
4. The current is not limited by the ohmic contact.
5. The effect of the space charge regions near the contact is negligible.
6. The traps are homogeneously distributed in the layer.
7. The emission of electrons out of traps does not depend on the electric field (thus no PF effect).

The first five conditions have been examined by Den Boer [7,3] who has found that these conditions have been fulfilled for SCLC measurements of n-i-n devices.

There is evidence for an inhomogeneous distribution of gap states in the layer (condition 6), especially near the substrate the material has more traps than in the bulk of the layer [8,9]. In this section it is shown that the injected charge is concentrated near the injecting contact. Since we have used the top contact as the injecting contact for all our measurements, the injected charge is trapped by the gap states near the contact. In this way the defects near the substrated (opposite the top contact) cannot disturb the measurements.

The last condition will be examined in section 5.4. In that section the Poole-Frenkel (PF) effect, which is the increase of the emission rate of electrons from positive traps under the influence of an electric field [5], is investigated. It will be shown in section 5.4 that the PF effect is absent in a-Si:H devices, thus the last condition is also valid for a-Si:H.

We will now describe the step-by-step method developed by Den Boer [3,7] that is used to obtain the density of gap states. The principle of this technique is that the shift in the Fermi level and the increase of the space charge can be calculated from the increase of the current after a step in the voltage. When the shift in the Fermi level and the increase of the space charge is known, then the average density of gap states between the initial and shifted Fermi level can be calculated. It is called the step-by-step method, because the average density of gap states is calculated after each voltage step and the Fermi level is traced by adding the shift in the Fermi level to the equilibrium Fermi level that is obtained by activation energy measurements.

The shift in the Fermi level between two current-voltage points (I_1, V_1) and (I_2, V_2) is given by

$$\Delta E_{f_1} = kT \ln\left(\frac{I_2 V_1}{I_1 V_2}\right) = E_{f_2} - E_{f_1} . \tag{5.1}$$

This expression is derived from the electron density in the extended states

$$n_e = N_c \, e^{(E_f - E_c)/kT} , \tag{5.2}$$

and the current density

$$J = q\mu_n^e n_e \frac{V}{d} , \tag{5.3}$$

where μ_n^e is the electron mobility in the extended states and d is the thickness of the intrinsic layer.

The localized charge injected per unit area can be expressed approximately as

$$\mathcal{Q}_1 = -\frac{\kappa\epsilon_s}{d}(V_2 - V_1) , \tag{5.4}$$

where ϵ_s is the static dielectric constant, and κ is a constant that accounts for the nonuniformity of the space charge. For a uniform distribution of the space charge $\kappa = 1$, and if the space charge is concentrated at the injecting contact $\kappa = 2$. We will use $\kappa = 2$ for the analysis of the I-V measurements. $\mathcal{Q}_1$ can be related to the average density of gap states g_1 by

$$\mathcal{Q}_1 = -qd\Delta E_{f_1} g_1 . \tag{5.5}$$

Combining equations 5.4 and 5.5 gives the average density of gap states for the first interval:

$$g_1 = \frac{\kappa\epsilon_s}{qd^2\Delta E_{f_1}}(V_2 - V_1) , \tag{5.6a}$$

where

$$\Delta E_{f_1} = kT \ln\left(\frac{I_2 V_1}{I_1 V_2}\right) . \tag{5.6b}$$

When the voltage is increased in a step-like manner the shift of the Fermi level at every step and the average density of gap states can be obtained from equation 5.6. In this way $g(E)$ can be calculated in a step-by-step process.

5.2.2 Error Estimation of the SCLC Analysis

In the derivation of equation 5.6, which is the basis of the step-by-step method the following approximations are used:

1. The space charge is distributed homogeneously in the layer.
2. The electric field is uniform in the film.
3. The Fermi-Dirac distribution is a step function.

The first two approximations are contradictory and this introduces an error in the density of gap states of a factor of two at the most. This effect is incorporated in the factor κ in equation 5.6a that takes a value between 1 and 2.

The effect of the first two approximations can be estimated with the use of an exponential distribution of gap states. The exponential distribution gives a good approximation for the density of gap states near the Fermi level for a-Si:H, and there is an analytic solution for the current as a function of the voltage. The analytic solution does not use the assumptions 1 and 2, but solves the Poisson equation and the continuity equation [10]. We will use the analytic solution to estimate the value of κ. The expression for the exponential distribution is

$$g(E) = \frac{N_t}{kT_c}\, e^{(E-E_c)/kT_c}\,, \tag{5.7}$$

where N_t is a constant, E_c is the conduction band edge, and T_c is the so-called characteristic temperature. The current-voltage characteristics can be obtained by using equation 5.4 and 5.5 for the charge per unit area and assuming that this charge is completely trapped

$$\mathcal{Q}_1 = -\frac{\kappa\epsilon_s}{d}(V_2 - V_1) = -qd\int_{E_{f1}}^{E_{f2}} \frac{N_t}{kT_c}\, e^{(E-E_c)/kT_c}\, dE\,. \tag{5.8}$$

If we combine equation 5.8 with the following equation for the current density

$$J = q\mu_n^e N_c\, e^{(E_f-E_c)/kT}\frac{V}{d}\,, \tag{5.9}$$

we obtain the following equation for the current density

$$J = q\mu_n^e N_c \left(\frac{\kappa\epsilon_s}{qN_t}\right)^{\ell} \frac{V^{\ell+1}}{d^{2\ell+1}}\,, \tag{5.10}$$

where the exponent ℓ is equal to T_c/T. The analytic solution is [10]

$$J = q\mu_n^e N_c \left(\frac{\ell\epsilon_s}{qN_t(\ell+1)}\right)^{\ell} \left(\frac{2\ell+1}{\ell+1}\right)^{\ell+1} \frac{V^{\ell+1}}{d^{2\ell+1}}\,. \tag{5.11}$$

When the two solutions are compared, we find for the factor κ the following equation:

$$\kappa^{\ell} = \left(\frac{\ell}{\ell+1}\right)^{\ell} \left(\frac{2\ell+1}{\ell+1}\right)^{\ell+1}. \tag{5.12}$$

This means that $\ell \equiv T_c/T = 3$, which is a typical value for a-Si:H [11,12], gives $\kappa = 1.58$. If the space charge is uniformly distributed then $\kappa = 1$, and $\kappa = 2$ if the space charge is concentrated near the injecting contact. The value of 1.58 for κ shows that the space charge is concentrated near the injecting contact. Since we use the top contact as the injecting contact, we measure the density of gap states of the top of the layer.

We will use $\kappa = 2$ for the analysis of the current-voltage measurements, and this means that the correction in the density of gap states for the nonuniformity of the space charge is at most a 25 % reduction of the measured density of gap states.

The analytic solution of equation 5.11 and the solution of equation 5.10 were obtained with the approximation that the Fermi-Dirac distribution is a step function. The error introduced by considering the Fermi-Dirac distribution as a step function can be evaluated with the use of the exponential distribution of gap states and the Sommerfeld expansion [13]. The Sommerfeld expansion is used to calculate integrals of the form

$$\int_{-\infty}^{\infty} g(E)f(E)\, dE\,, \qquad f(E) = \frac{1}{e^{(E-E_f)/kT} + 1}\,, \tag{5.13}$$

where $g(E)$ is the density of gap states and $f(E)$ is the Fermi-Dirac distribution. This integral can be expanded to

$$\int_{-\infty}^{\infty} g(E)f(E)\, dE = \int_{-\infty}^{E_f} g(E)\, dE + \sum_{n=1}^{\infty} a_n (kT)^{2n} \frac{d^{2n-1}}{dE^{2n-1}} g(E)\bigg|_{E=E_f}\,, \tag{5.14}$$

where the a_n are dimensionless numbers given by

$$a_n = 2\sum_{k=1}^{\infty} \frac{(-1)^{k+1}}{k^{2n}}\,. \tag{5.15}$$

The first order expansion is given by

$$\int_{-\infty}^{\infty} g(E)f(E)\, dE \approx \int_{-\infty}^{E_f} g(E)\, dE + \frac{\pi^2}{6}(kT)^2 \frac{d}{dE} g(E)\bigg|_{E=E_f}. \tag{5.16}$$

The first term of this expansion is the integral with a step function for the Fermi-Dirac distribution, while the second term gives the correction to this approximation. When the first order Sommerfeld expansion is applied to the exponential distribution of gap states, we have

$$\begin{aligned}
&\int_{-\infty}^{\infty} \frac{N_t}{kT_c} e^{(E-E_c)/kT_c} f(E)\, dE \approx \\
&\quad \frac{N_t}{kT_c} \int_{-\infty}^{E_f} e^{(E-E_c)/kT_c}\, dE + \frac{N_t}{kT_c} \frac{\pi^2}{6} (kT)^2 \frac{d}{dE} e^{(E-E_c)/kT_c} \Big|_{E=E_f} \\
&\qquad = N_t\, e^{(E_f-E_c)/kT_c} \left(1 + \frac{\pi^2}{6} \left(\frac{T}{T_c}\right)^2\right) . \qquad (5.17)
\end{aligned}$$

When $\ell = T_c/T = 3$ is substituted in equation 5.17, the correction for the deviation from a step function is found. This correction is 20% for $\ell = 3$ which means that the space charge and the density of gap states is about 20% lower than measured with the step-by-step method.

The two corrections of 25% and 20% result in a correction in the density of gap states of 40% at the most.

5.2.3 The Poole-Frenkel Correction

In this subsection a correction of the step-by-step method is presented that takes into account the Poole-Frenkel (PF) effect. This PF effect is the increase of the emission rate of electrons from positive traps under the influence of an electric field [5].

In figure 5.2 the potential energy of an electron in the electric field of a positive defect is depicted. The potential energy is

$$U(r) = \frac{-q^2}{4\pi\epsilon_s |r|} , \qquad (5.18)$$

where q is the elementary charge, ϵ_s is the static dielectric constant of the semiconductor, and r is the distance between the electron and the defect. When an electric field $\mathcal{E}$ is applied the potential energy is given by

$$U(r) = \frac{-q^2}{4\pi\epsilon_s |r|} - q\mathcal{E}\, r . \qquad (5.19)$$

This electric field results in the lowering of the effective barrier for the electron to escape [5]. The effective barrier is lowered by an amount

$$\Delta U = \frac{q^2}{4\pi\epsilon_s |r_m|} - q\mathcal{E}\, r_m = q\sqrt{\frac{q\mathcal{E}}{\pi\epsilon_s}} = \beta_{pf}\sqrt{\mathcal{E}} , \qquad (5.20)$$

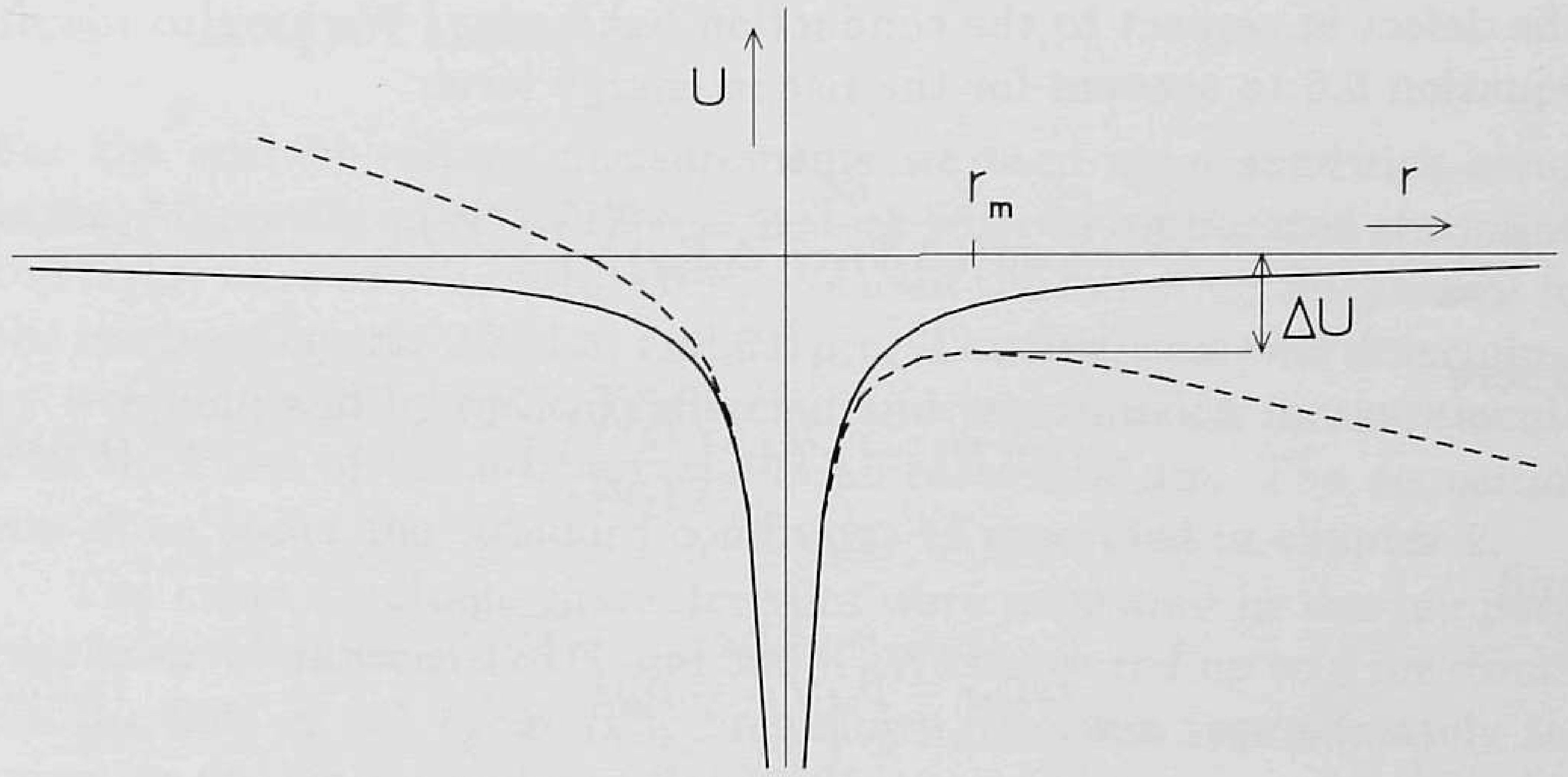

Figure 5.2: The potential energy of an electron as a function of the distance between the electron and a positive defect. The solid line is without an external field, the dashed line is with an external field.

where β_{pf} is called the Poole-Frenkel constant

$$\beta_{pf} = q\sqrt{\frac{q}{\pi\epsilon_s}} , \qquad (5.21)$$

and r_m is the distance between the electron and the defect where the maximum in the potential energy is obtained for $r > 0$.

The probability that an electron is emitted from a trap by thermal excitation is increased by a factor $\exp(\Delta U/kT)$. This factor was used by Frenkel [5] to obtain the following equation for the conductivity:

$$\sigma = \sigma_0\, e^{\beta_{pf}\sqrt{\mathcal{E}}/kT} . \qquad (5.22)$$

In the literature, equations like equation 5.22 have been used to analyze the current-voltage characteristic [14,15,16,17]. We will not do this, but instead we will use equation 5.20 to obtain the lowering of the barrier and use this to modify the step-by-step method of equation 5.6. This is a more general method than equation 5.22. The modified step-by-step method will be used to obtain the correct density of gap states in the case of positive defects. The lowering of the barrier for the electron to escape from a positive defect results in the rise of the energy level of the defect in respect to the conduction band edge. We have to rewrite equation 5.6 to account for the rise in energy level:

$$g_1 = \frac{\kappa\epsilon_s}{qd^2(\Delta E_{f1} - \Delta E_{pf})}(V_2 - V_1)\,, \tag{5.23a}$$

where

$$\Delta E_{f_1} = kT\ln\left(\frac{I_2V_1}{I_1V_2}\right), \tag{5.23b}$$

and

$$\Delta E_{pf} = \beta_{pf}\sqrt{\mathcal{E}} = \beta_{pf}\sqrt{\frac{V_2}{d}}\,. \tag{5.23c}$$

This equation can be used to obtain $g(E)$ from the J-V characteristics when the gap states are positive defects.

The current-voltage characteristics in the case of an exponential distribution can be derived in the same way as equation 5.10. The charge per unit area is

$$\mathcal{Q}_1 = -\frac{\kappa\epsilon_s}{d}(V_2 - V_1) = \int\limits_{E_{f1}-\beta_{pf}\sqrt{V_2/d}}^{E_{f2}-\beta_{pf}\sqrt{V_1/d}} -qd\frac{N_t}{kT_c}\,e^{(E-E_c)/kT_c}\,dE\,. \tag{5.24}$$

Following the same method as for equation 5.10, we obtain for the current density

$$J = q\mu_n^e N_c\left(\frac{\kappa\epsilon_s}{qN_t}\right)^{\ell}\frac{V^{\ell+1}}{d^{2\ell+1}}\,e^{\beta_{pf}\sqrt{(V/d)}/kT}\,. \tag{5.25}$$

The characteristic temperature is obtained from the slope of $\ln(J)$ versus $\ln(V)$

$$\frac{T_c'}{T} = \frac{d\ln(J)}{d\ln(V)} - 1 = \frac{T_c}{T} + \frac{\beta_{pf}\sqrt{V/d}}{2kT}\,. \tag{5.26}$$

The last term is the deviation of the measured characteristic temperature T_c' from the real characteristic temperature T_c caused by the PF effect.

5.3 Experiment

For the current-voltage measurements we used n-i-n sandwich structures. Mono-silicon wafers, 0.5 mm thick with an evaporated chromium top layer, were used as substrates. We used the following thicknesses for the intrinsic layers: 0.7, 1.5, and 3.0 μm. The thickness was determined by weighing and by optical reflection and transmission measurements. The thickness of the n-layers was in all cases 0.05 μm. The deposition was done under the standard conditions as described in chapter 2.

The current-voltage characteristics were measured in the temperature interval between 170 K and 340 K. We measured up to a maximum electric field of 10^5 V/cm. The breakdown field was approximately the same for all devices and was 3×10^5 V/cm.

The deviation from a linear I-V characteristics can in certain cases be caused by ordinary Joule heating of the device due to the high currents [18] (and be mistaken for a space charge limited current). We found a maximum current-density of 10 A/cm^2, and a maximum voltage of 10 V for the 1.5 μm thick device with a dot area of 0.25 mm^2. The increase in temperature depends on the applied power (100 W/cm^2), on the thickness of the wafer (5×10^{-2} cm), and on the thermal conductivity of silicon (1.5 W/Kcm). This gives a worst case temperature increase of 3 K, so Joule heating can be neglected in our measurements.

5.4 Investigation of the Poole-Frenkel Effect

The scaling law is a universal law for SCLC measurements [1]. We used this scaling law to verify that the deviation from a linear I-V characteristics can be attributed to a bulk SCLC mechanism [1,2]. The scaling law gives the following relation between the layer thickness and the critical voltage [19]

$$\frac{V_c}{d^2} = \text{constant}\,. \tag{5.27}$$

The critical voltage (V_c) is defined as the transition voltage from an Ohmic to an SCL current. We obtained this transition voltage from

Table 5.1: The relation between the layer thickness and the critical voltage.

layer thickness (μm)	0.7	1.5	3.0
critical voltage (V)	0.19	1.3	6.0
V_c/d^2 (V/μm^2)	0.39	0.58	0.67

a linear extrapolation of the Ohmic and the SCL current. The intersection point of the two lines in the $\ln(I)$ versus $\ln(V)$ plot gives the critical voltage. As can be seen in table 5.1, there is a deviation from this relation for the sample with a thickness of $0.7\,\mu$m. We believe this to be caused by the difficulty of obtaining V_c accurately, and the fact that the space charge regions in the intrinsic layer cannot be neglected in thin samples. The values for $d = 1.5\,\mu$m and $d = 3.0\,\mu$m confirm a true SCLC current-voltage characteristics.

We used equation 5.6 (the step-by-step method) to obtain the density of gap states. Figure 5.3a shows the density of gap states measured at different temperatures using an n-i-n device with an i-layer thickness of $1.5\,\mu$m. Using equation 5.23 we obtain the density of gap states in the case of PF emission. The results of this analysis are shown in figure 5.3b. When the figures 5.3a and 5.3b are compared it can be seen that the PF effect results in a higher density of gap states compared to figure 5.3a, which was expected. It can also be seen that the density of gap states curve increases rapidly in figure 5.3b, and that this rapid increase shifts with the temperature. We believe that this rapid increase in the DOS is not realistic but the result of the analysis and that it is a compensation in the DOS for the incorporation of the PF effect. The extrapolation of the density of gap states to E_c would give nonrealistic values of $g(E_c)$ for figure 5.3b. Therefore, we conclude that there is no PF effect, so the gap states in a-Si:H are predominantly neutral when empty. The temperature dependence of the density of gap states will be discussed in the next section.

We also examined the characteristic temperature, because this value is obtained at high fields and is very sensitive to the PF effect. The characteristic temperature (T_c) was obtained from the slope of the $\ln(I)$

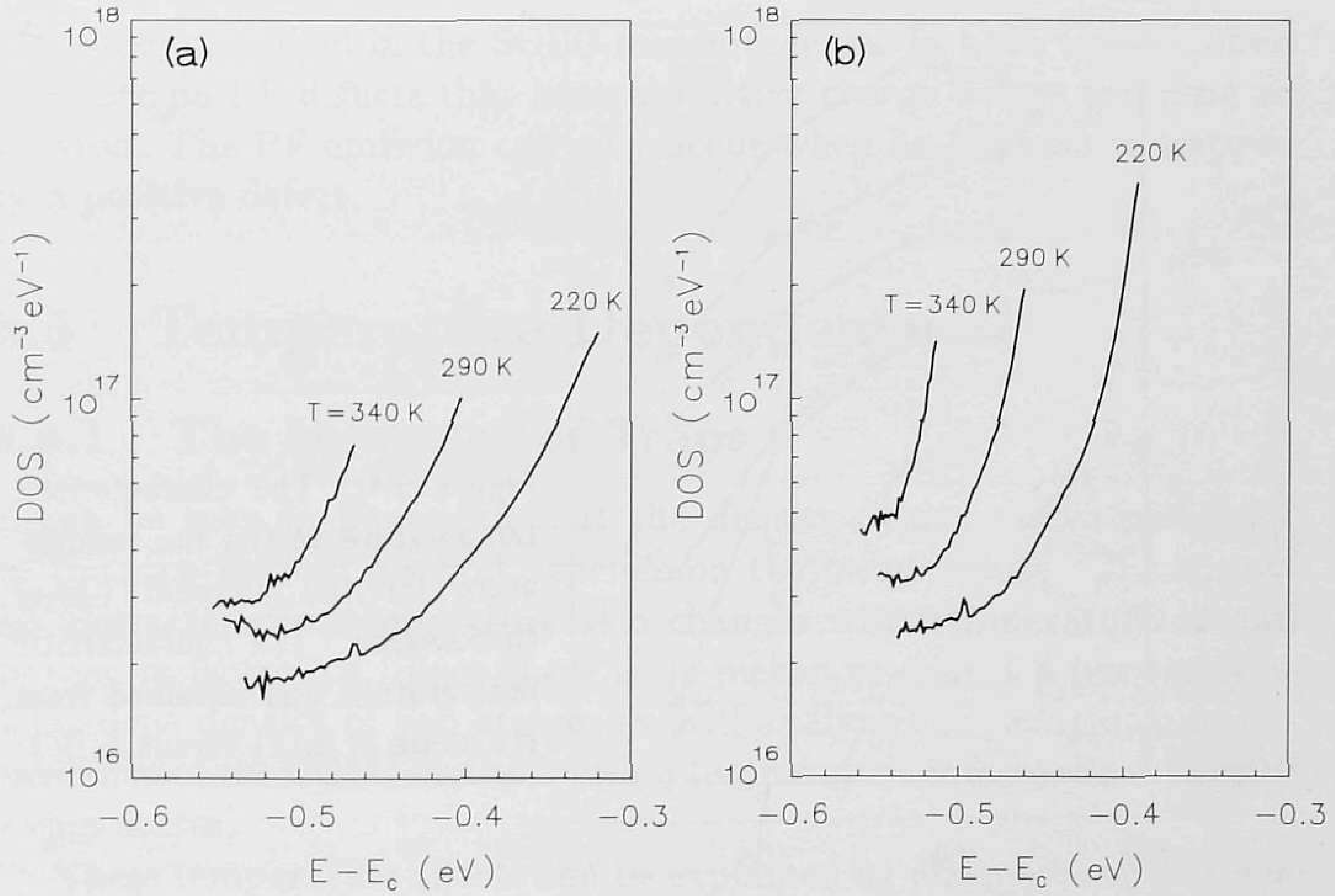

Figure 5.3: The density of gap states distribution that was obtained from *I-V* measurements: (a) with the use of the step-by-step method (b) using the step-by-step method that has been corrected for the PF effect.

versus $\ln(V)$ plot in the SCLC regime using the following equation

$$\ln(I) = (T_c/T + 1)\ln(V) + \text{constant}\,, \qquad (5.28)$$

which can be obtained from equation 5.10. This means that a steep slope in the plot of $\ln(I)$ versus $\ln(V)$ gives a high T_c, while in the plot of the gap states distribution versus E a steep slope means a low T_c. All the $\ln(I)$ versus $\ln(V)$ plots gave a straight line in the SCLC regime. Figure 5.4 shows T_c for the different layer thicknesses and temperatures, and it is clear from the figure that T_c falls in a wide range from 300 to 1300 K as was already reported by Furukawa et al. [19]. The PF effect on an exponential distribution is described by equation 5.26, and it shows that T_c should increase with increasing electric field. Equation 5.26 also shows that T_c should be independent of the temperature. The dependence of T_c on the layer thickness cannot be explained by an increase of the electric field since all devices have been measured up to a

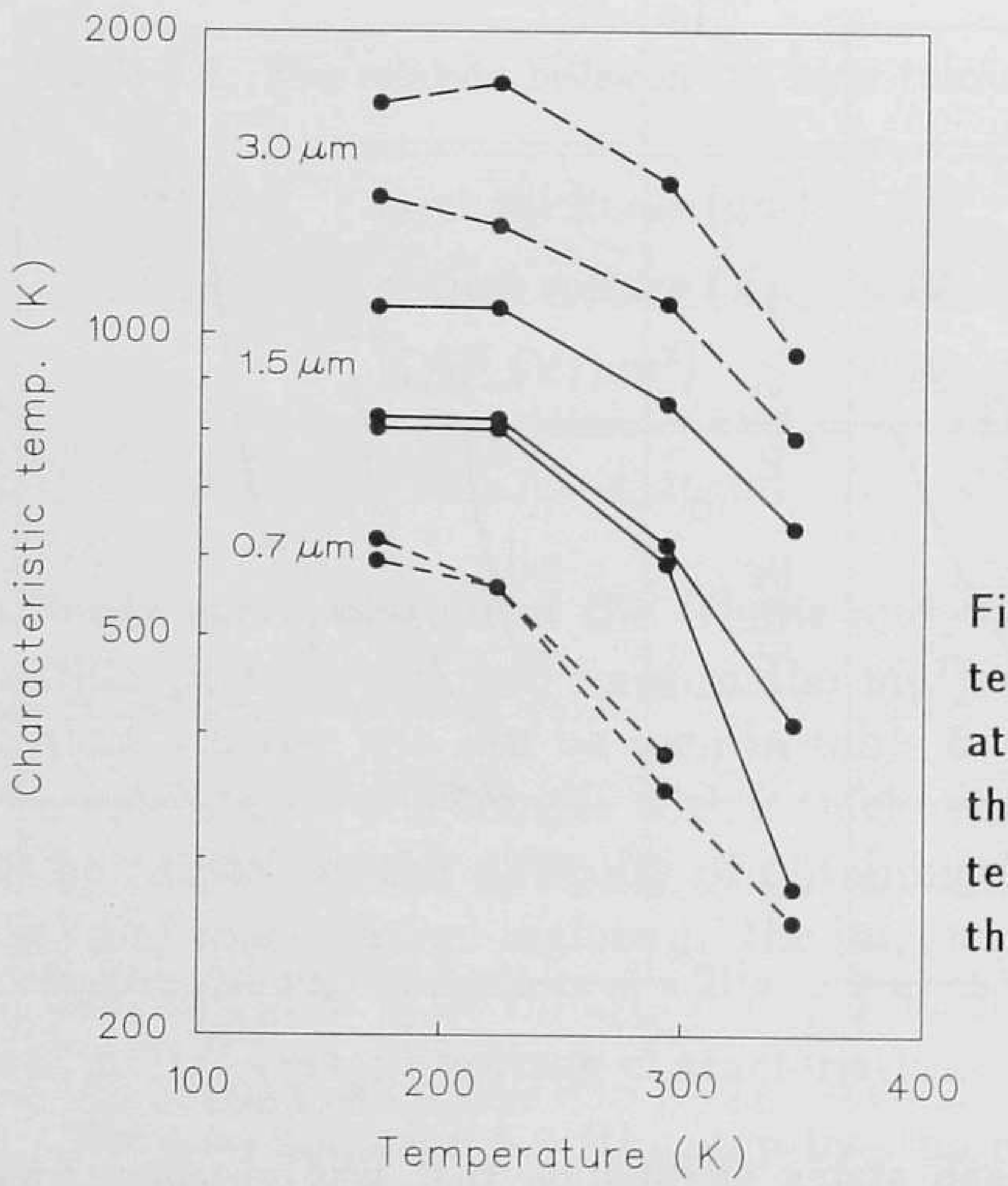

Figure 5.4: The characteristic temperature versus the temperature for the different i-layer thicknesses. The characteristic temperature was obtained from the slope of $\ln(I)$ versus $\ln(V)$.

maximum field of 10^5 V/cm at 220 K (at higher temperatures the maximum current limits the maximum field). Therefore, the temperature dependence of T_c and the increase of T_c with increasing layer thickness cannot be explained by a PF effect. The temperature dependence of T_c will be further discussed in the next section together with the increase of T_c with increasing layer thickness.

Our conclusion that there is no PF effect in a-Si:H devices can also be based on the current models for the gap states distribution of a-Si:H. There are two models for the gap states in a-Si:H that are often used [20]. One model supposes that the states in the middle of the gap originate from band tails of localized states (this is the CFO model, see chapter 1). Those derived from the conduction band are neutral when empty and those from the valence band are neutral when full. The states that originate from the conduction band are the ones that are filled in the SCLC measurements. The other model regards dangling bonds as the defects that cause the states in the middle of the gap (this is the model of Mott, see chapter 1). These dangling bonds are considered to be neutral with an unpaired spin, and they become negative

when they are filled in the SCLC measurements. In both these models there are no PF defects that have a positive charge before trapping an electron. The PF emission can only occur when an electron is trapped by a positive defect.

5.5 Temperature Dependence

5.5.1 The Influence of Traps

It can be seen in figure 5.3 that the density of gap states measured by the step-by-step method depends on the temperature. The apparent characteristic temperature also changes with temperature as can be seen in figure 5.4. Since there is no reason to expect a temperature dependent density of gap states, we will analyze this temperature dependence of the SCLC method with a temperature independent density of gap states.

These temperature effects can be explained by discrete trap levels in the energy band since their charge state depends strongly on temperature. We consider first a single trap level. Since equilibrium is assumed the emission rate and the capture rate must be equal

$$\nu_0 N_t^- \, e^{(E_t-E_c)/kT} = \sigma_t v_{th} n_e N_t^0 \,, \tag{5.29}$$

where ν_0 is the release rate, E_t the trap energy level, σ_t the capture cross section of the trap, v_{th} the carrier thermal velocity, and N_t^0 and N_t^- are the empty and filled trap densities, respectively. The space charge due to these traps is

$$Q_t = -qN_t^- = -q\frac{\sigma_t v_{th} n_e N_t}{\nu_0 \, e^{(E_t-E_c)/kT} + \sigma_t v_{th} n_e} \,, \tag{5.30}$$

where the total trap density is used, which is defined by $N_t = N_t^0 + N_t^-$. Since σ_t, v_{th}, and ν_0 have a small temperature dependence compared to n_e and $\exp[(E_t - E_c)/kT]$, we can write

$$Q_t = -q\frac{s_t n_e N_t}{e^{(E_t-E_c)/kT} + s_t n_e} \,, \tag{5.31}$$

where

$$s_t = \frac{\sigma_t v_{th}}{\nu_0} = \text{constant} \,. \tag{5.32}$$

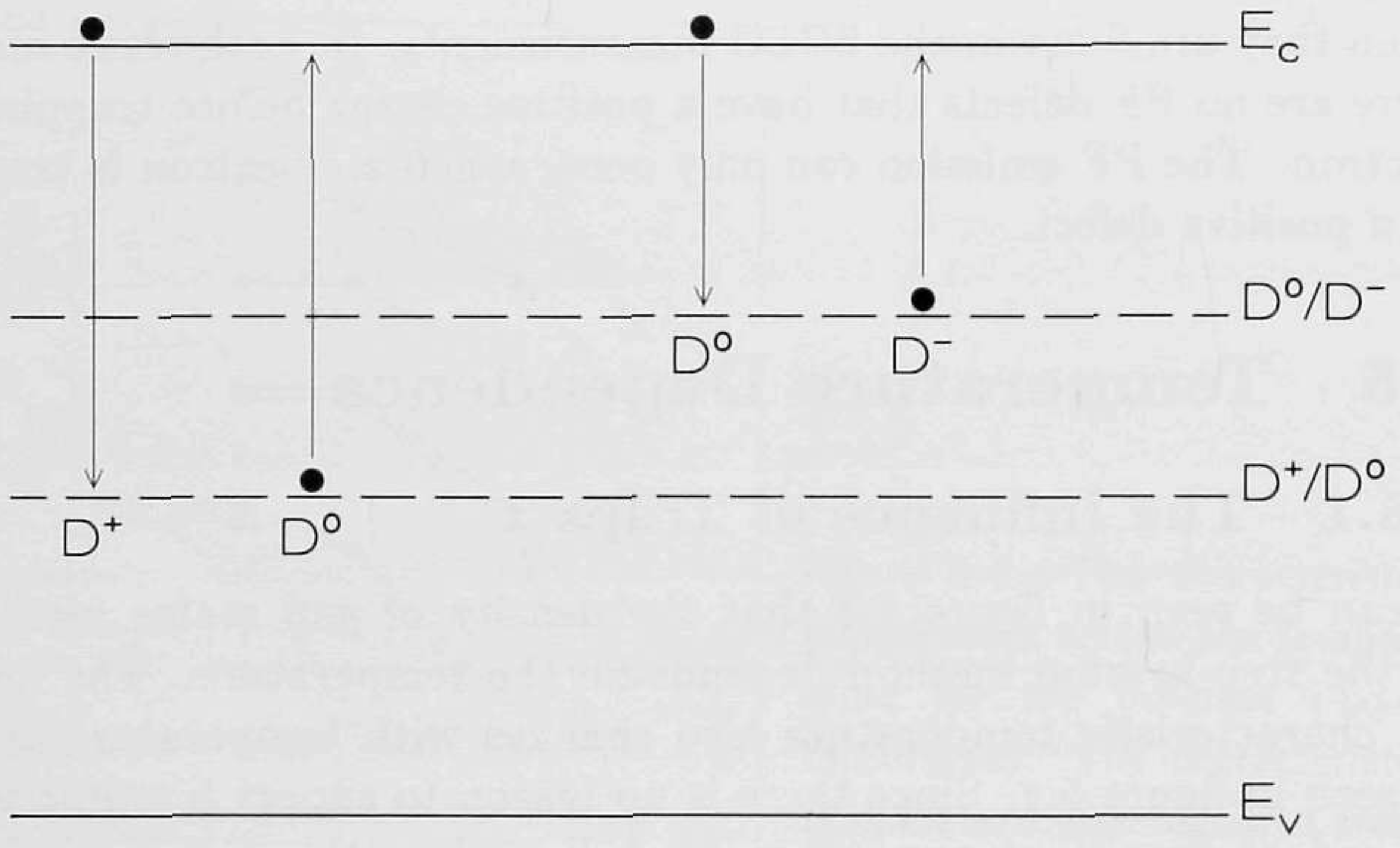

Figure 5.5: The capture and release of electrons by dangling bonds. D^0, D^-, and D^+ indicate the neutral, negative, and positive dangling bond, respectively.

Another kind of defect is the dangling bond. This dangling bond can have three charge states, namely empty (N_{db}^+), single occupied (N_{db}^0), and double occupied (N_{db}^-). A special feature of the dangling bond is that it has two levels in the energy gap separated by the correlation energy [21,22]. The correlation energy is the difference in energy of a double and single occupied dangling bond. This correlation energy is positive, i.e., the double occupied dangling bond has a higher energy than the single occupied dangling bond. A negative correlation energy would give the Poole-Frenkel effect [22,23]. The capture and release of electrons by dangling bonds is depicted in figure 5.5. For the density of single occupied dangling bonds we have

$$N_{db}^0 = \frac{s_{db}^+ n_e N_{db}}{e^{(E_{db}^0 - E_c)/kT} + s_{db}^+ n_e + s_{db}^+ s_{db}^0 n_e^2 \, e^{(E_c - E_{db}^-)/kT}} \,, \tag{5.33}$$

and for the density of double occupied dangling bonds we have

$$N_{db}^- = \frac{s_{db}^+ s_{db}^0 n_e^2 N_{db} \, e^{(E_c - E_{db}^-)/kT}}{e^{(E_{db}^0 - E_c)/kT} + s_{db}^+ n_e + s_{db}^+ s_{db}^0 n_e^2 \, e^{(E_c - E_{db}^-)/kT}} \,. \tag{5.34}$$

The charge in the dangling bonds is

$$\begin{aligned} Q_{db} &= q(N_{db} - 2N_{db}^- - N_{db}^0) \\ &\approx q \frac{N_{db} \, e^{(E_{db}^0 - E_c)/kT} - s_{db}^+ s_{db}^0 n_e^2 N_{db} \, e^{(E_c - E_{db}^-)/kT}}{e^{(E_{db}^0 - E_c)/kT} + s_{db}^+ n_e + s_{db}^+ s_{db}^0 n_e^2 \, e^{(E_c - E_{db}^-)/kT}} \,, \end{aligned} \tag{5.35}$$

where we have used the inequalities

$$n_e \ll N_{db} \quad \text{and} \quad \frac{e^{(E_{db}^- - E_c)/kT}}{N_{db} s_{db}^0} \ll 1 \,. \tag{5.36}$$

We will also consider an exponential distribution of gap states that increases with increasing energy, and another exponential distribution that decreases with increasing energy. These exponential distributions will be called *deep* tail states to discriminate them from the *shallow* tail states near the mobility edges. These deep tails are also mentioned in chapter 1 in relation with the CFO model for the density of states. The deep tail of the conduction band contributes to the density of gap states with

$$g_{ct}(E) = \frac{N_{ct}}{kT_{ct}} e^{(E - E_c)/kT_{ct}} \,, \tag{5.37}$$

and the deep tail of the valence band contributes with

$$g_{vt}(E) = \frac{N_{vt}}{kT_{vt}} e^{(E_v - E)/kT_{vt}} \,. \tag{5.38}$$

The charge in the deep tail of the conduction band is

$$Q_{ct} = -q \int_{-\infty}^{\infty} g_{ct}(E) f(E) \, dE \approx -q N_{ct} \left(1 + \frac{\pi^2 T^2}{6 T_{ct}^2}\right) e^{(E_f - E_c)/kT_{ct}} \,, \tag{5.39}$$

and in the deep tail of the valence band the charge is

$$Q_{vt} = q \int_{-\infty}^{\infty} g_{vt}(E)(1 - f(E)) \, dE \approx q N_{vt} \left(1 + \frac{\pi^2 T^2}{6 T_{vt}^2}\right) e^{(E_v - E_f)/kT_{vt}} \,. \tag{5.40}$$

The space charge is given by the total charge. The total charge is the sum of the charge in the traps, in the dangling bonds, and in the deep tail states given by

$$Q_{tot} = Q_t + Q_{db} + Q_{ct} + Q_{vt} \,. \tag{5.41}$$

The *J-V* characteristics of n-i-n devices can be simulated with the use of the equations for the space charge. The following procedure is used with the Fermi level as a parameter:

1. Calculate n_e using the Fermi level and $n_e = N_c\, e^{(E_f - E_c)/kT}$.
2. Calculate the space charge with equation 5.41.
3. The voltage is obtained from $V = -(Qd^2)/(\kappa\epsilon_s)$.
4. The current is obtained from $J = q\mu_n^e n_e V/d$.

These four steps are repeated in the indicated order for a range of Fermi levels to obtain a smooth *J-V* curve.

In figure 5.6 the simulated current-voltage characteristics of an n-i-n device is shown. The density of gap states of this simulation consists of dangling bonds with the input parameters of table 5.2. The values of the input parameters have been obtained from the literature [25,26]. In figure 5.7 the apparent density of gap states is shown as obtained from the *J-V* characteristics with the step-by-step method. It is clear that the apparent density of gap states depends strongly on the temperature. The slope of $\ln(J)$ versus $\ln(V)$ in the SCLC regime is independent of T, and J is proportional to V^2. This means that the characteristic temperature, obtained by equation 5.28, is equal to the measurement temperature. The increase of the characteristic temperature with increasing temperature was not observed in our measurements. On the contrary, the opposite effect was observed as can be seen in figure 5.4.

The simulation of the *J-V* characteristics of an n-i-n device with the two exponential distributions and a single trap level for the density of gap states is shown in figure 5.8. The apparent density of gap states as obtained by the step-by-step method, shown in figure 5.9, is similar to the measured curves of figure 5.3a. We will use this distribution as a starting point for the comparison of simulated and experimental data in the next subsection.

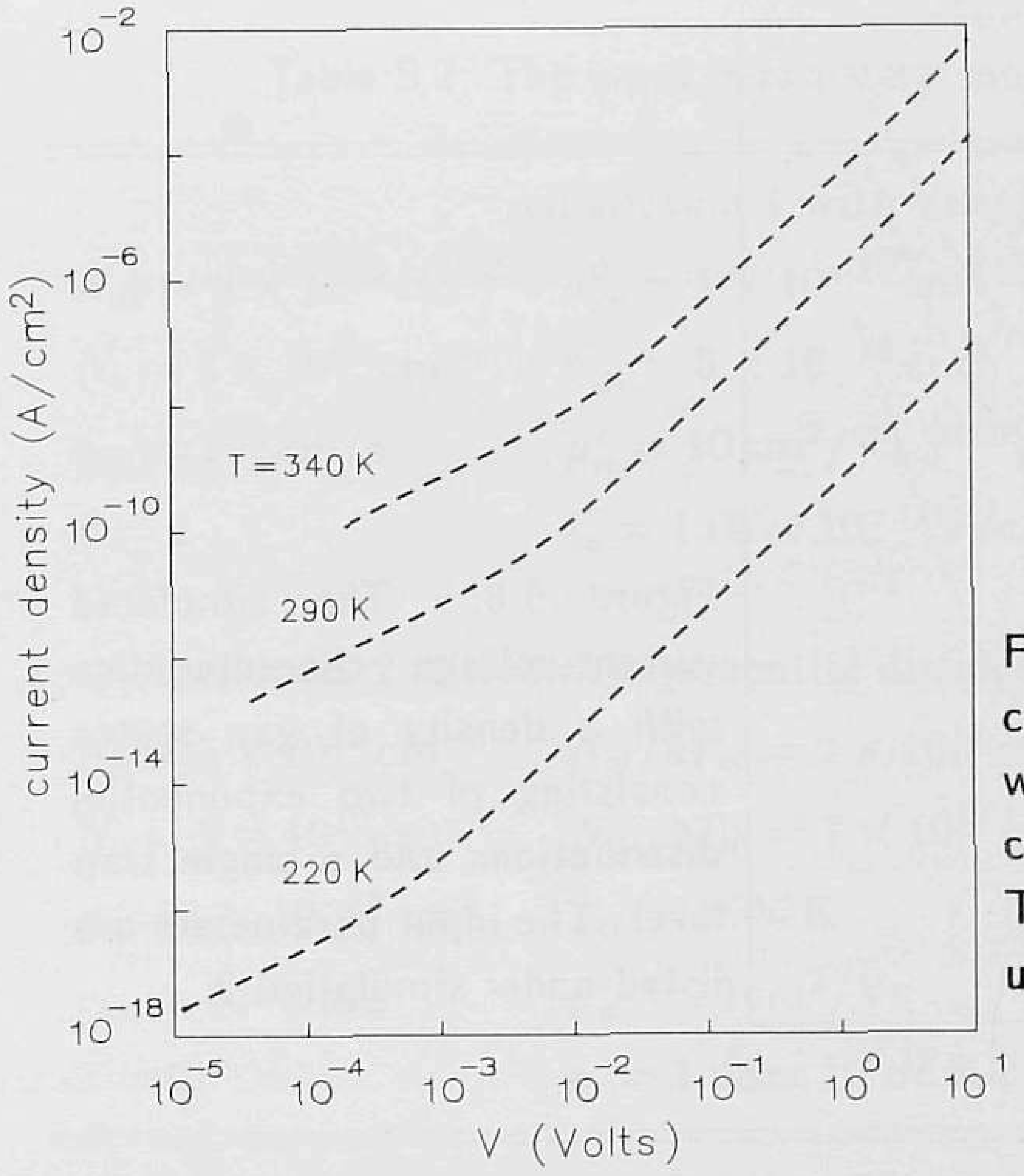

Figure 5.6: The simulated current-voltage characteristics with a density of gap states consisting of dangling bonds. The input parameters are listed under simulation 1.

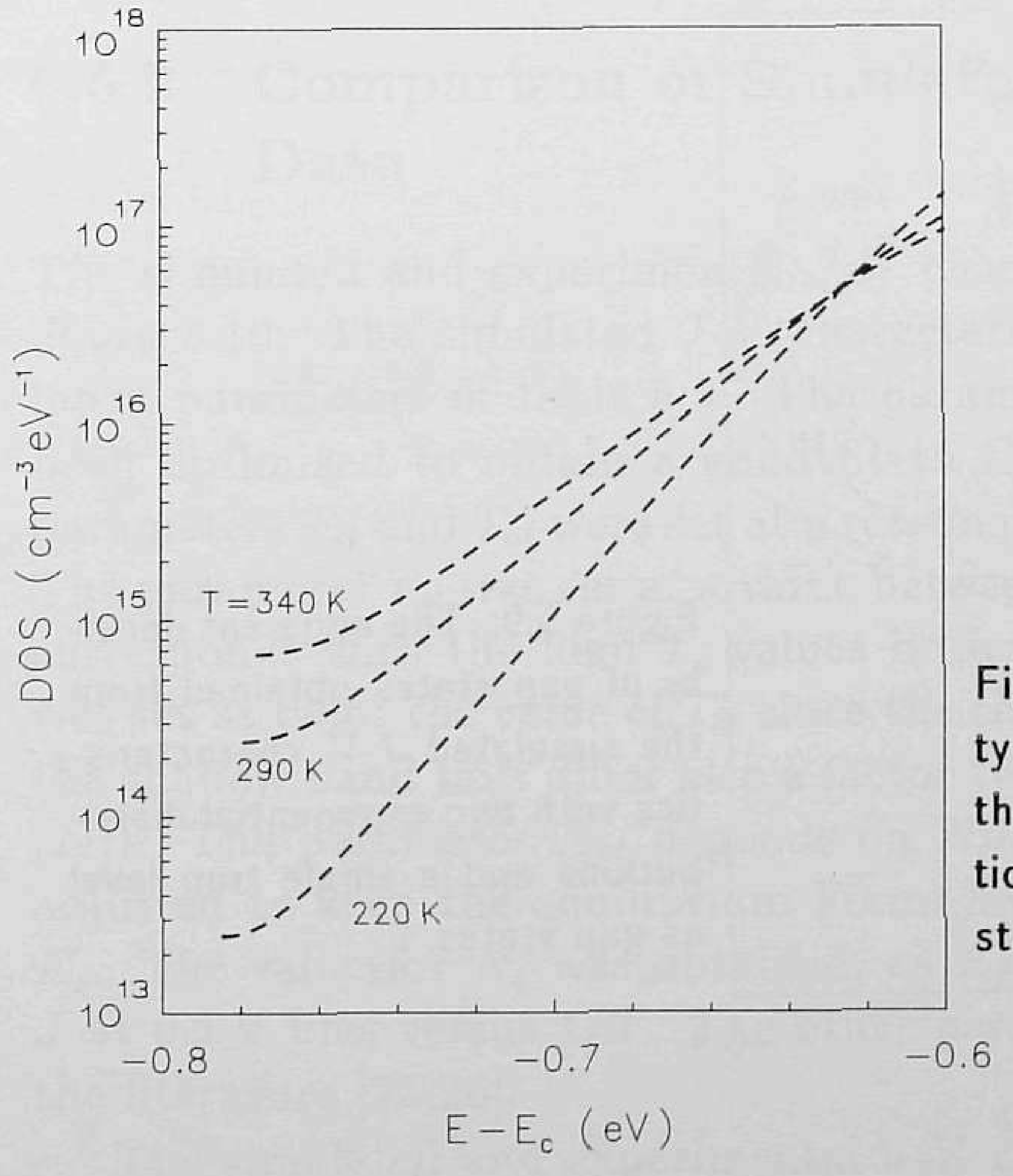

Figure 5.7: The apparent density of gap states obtained from the simulated *J-V* characteristics with dangling bonds as gap states.

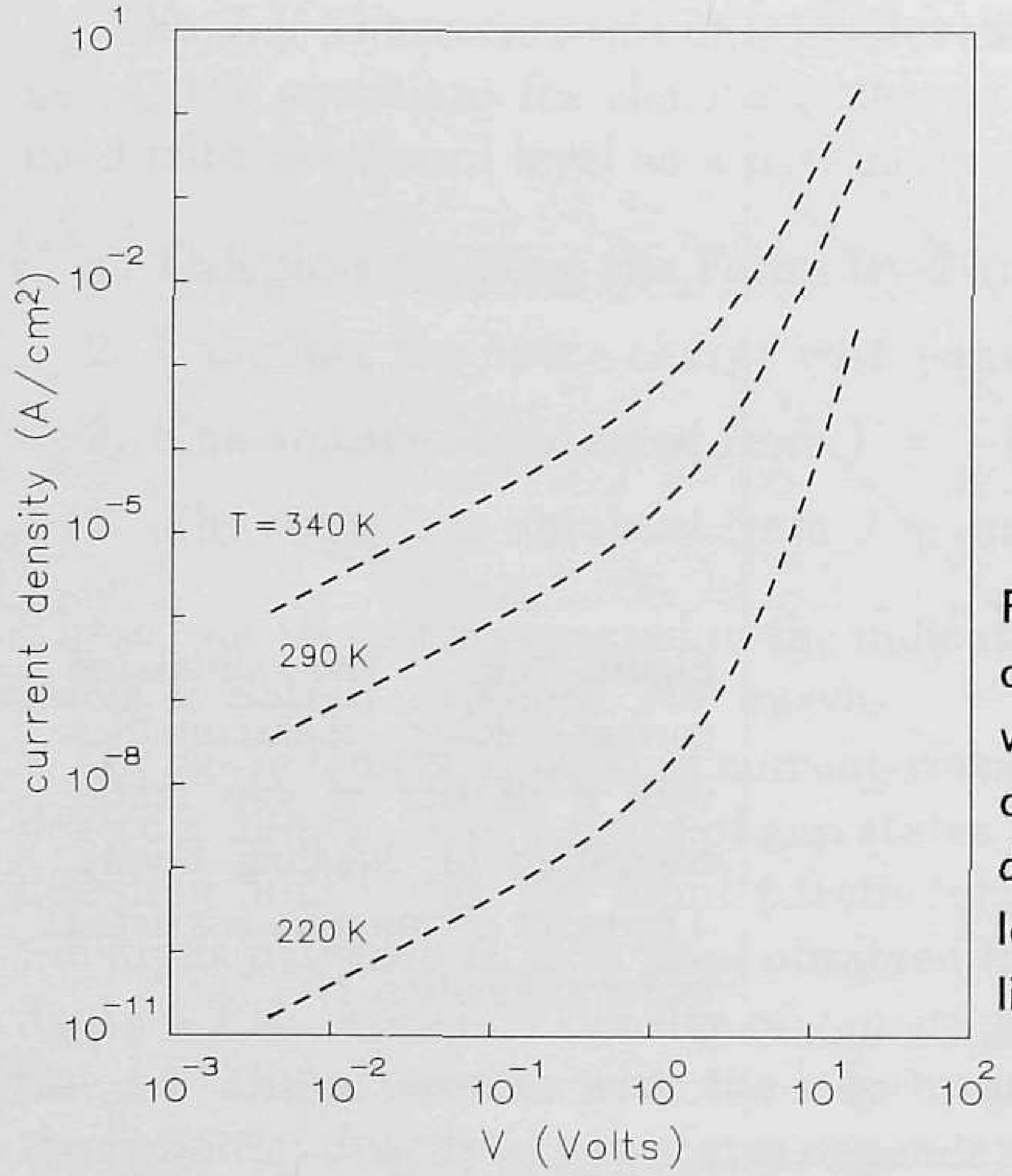

Figure 5.8: The simulated current-voltage characteristics with a density of gap states consisting of two exponential *distributions and a single trap* level. The input parameters are listed under simulation 2.

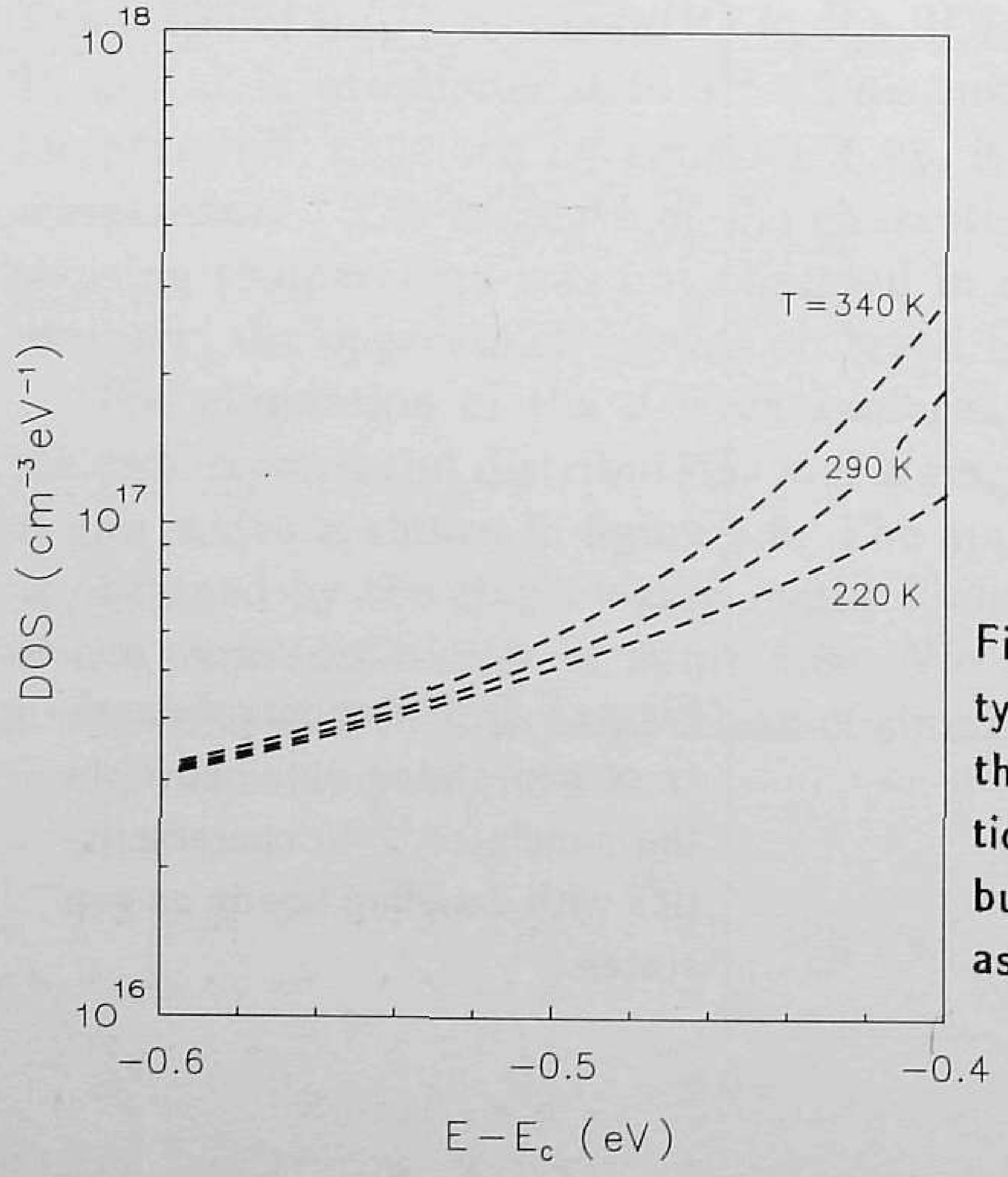

Figure 5.9: The apparent density of gap states obtained from the simulated *J-V* characteristics with two exponential distributions and a single trap level as gap states.

Table 5.2: The input parameters used for the simulations.

	simulation 1 with dangling bonds	
$N_{db} = 2 \times 10^{16}\,\mathrm{cm}^{-3}$	$\sigma_{db}^{0} = 1 \times 10^{-15}\,\mathrm{cm}^2$	$E_c - E_{db}^{-} = 0.6\,\mathrm{eV}$
$N_c = 2 \times 10^{19}\,\mathrm{cm}^{-3}$	$\sigma_{db}^{+} = 5 \times 10^{-15}\,\mathrm{cm}^2$	$E_c - E_{db}^{0} = 1.0\,\mathrm{eV}$
$v_{th} = 10^7\,\mathrm{cm/s}$	$\mu_n^e = 10\,\mathrm{cm^2/Vs}$	$\nu_0 = 10^{12}\,\mathrm{s}^{-1}$
$\kappa = 2$	$\epsilon_s = 1.05 \times 10^{-12}\,\mathrm{F/cm}$	$d = 1.5\,\mu\mathrm{m}$
	simulation 2 with two exponential distributions and a single trap level	
$N_t = 5 \times 10^{18}\,\mathrm{cm}^{-3}$	$N_{ct}/kT_{ct} = 2 \times 10^{18}\,\mathrm{cm^{-3}eV^{-1}}$	$E_c - E_t = 0.25\,\mathrm{eV}$
$N_c = 2 \times 10^{19}\,\mathrm{cm}^{-3}$	$N_{vt}/kT_{vt} = 7 \times 10^{17}\,\mathrm{cm^{-3}eV^{-1}}$	$E_c - E_v = 1.7\,\mathrm{eV}$
$\sigma_t = 1 \times 10^{-15}\,\mathrm{cm}^2$	$T_{ct} = 1500\,\mathrm{K}$	$T_{vt} = 3000\,\mathrm{K}$
$v_{th} = 10^7\,\mathrm{cm/s}$	$\mu_n^e = 10\,\mathrm{cm^2/Vs}$	$\nu_0 = 10^{12}\,\mathrm{s}^{-1}$
$\kappa = 2$	$\epsilon_s = 1.05 \times 10^{-12}\,\mathrm{F/cm}$	$d = 1.5\,\mu\mathrm{m}$

5.5.2 Comparison of Simulated and Experimental Data

The simulated and experimental *J-V* characteristics are compared in figure 5.10. The simulated *J-V* characteristics are obtained with the input parameters of table 5.3. The parameters N_t, E_t, and N_{ct} have been optimized to obtain a good fit to the experimental data. The parameters T_{ct} and T_{vt} were set at a reasonable value and not optimized. The parameter T_{ct} was set at a value between 1000 K and 1500 K which corresponds with the high T_c values in figure 5.4. The parameter T_{vt} was set at twice the value of T_{ct} since the characteristic temperatures of the shallow band tails differ also a factor two (namely 250 K and 500 K [24]). The parameter N_{vt} depends on N_{ct}, if N_{ct} changes then N_{vt} is adjusted to keep the equilibrium Fermi level pinned at 0.56 eV below E_c. The value for N_c was obtained, as E_f, from the Arhenius plot of J at 0.1 V bias versus $1/T$. The other parameters were obtained from the literature [25,26].

The simulated and experimental *J-V* characteristics, shown in fig-

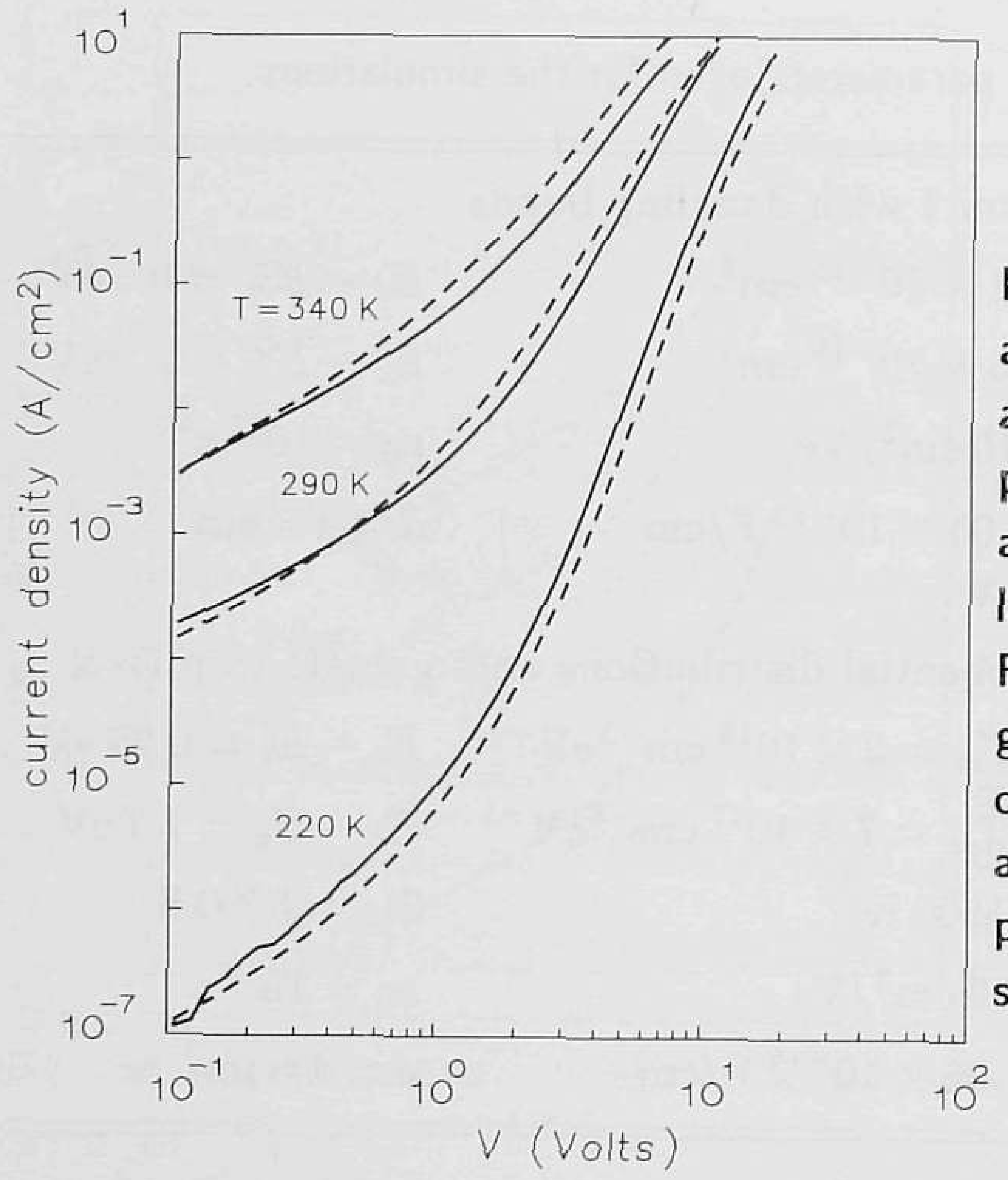

Figure 5.10: The simulated and experimental current-voltage characteristics. The experimental data is drawn with a solid line, and the simulated data with a dashed line. For the simulation a density of gap states was used consisting of two exponential distributions and a single trap level. The input parameters are listed under simulation 3.

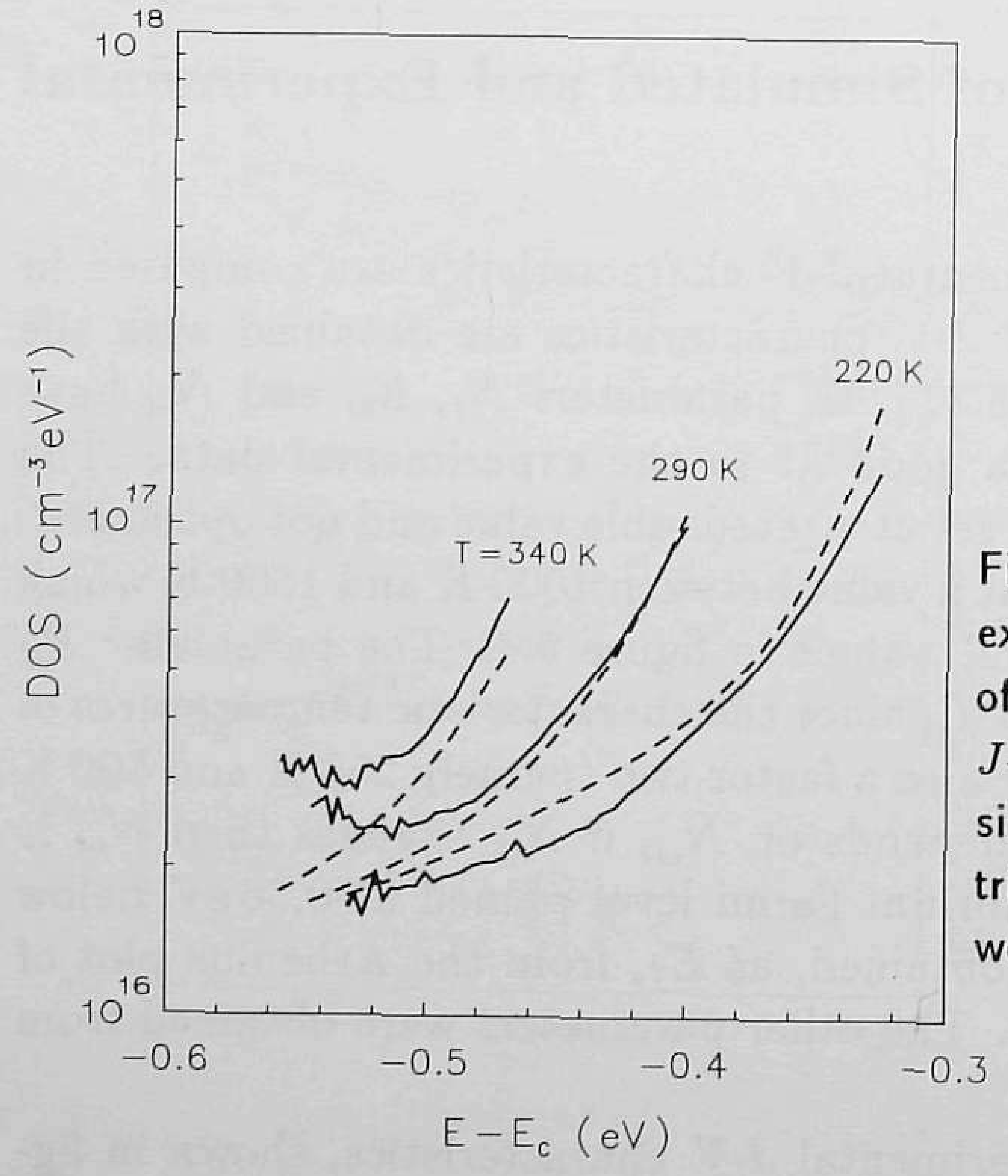

Figure 5.11: The simulated and experimental apparent density of gap states obtained from the *J-V* characteristics. For the simulation two exponential distributions and a single trap level were used as gap states.

Table 5.3: The input parameters used for the simulations which are compared with the experimental data.

simulation 3 with two exponential distributions and a single trap level		
$N_t = 2 \times 10^{19}\,\mathrm{cm}^{-3}$	$N_{ct}/kT_{ct} = 7.6 \times 10^{17}\,\mathrm{cm}^{-3}\mathrm{eV}^{-1}$	$E_c - E_t = 0.12\,\mathrm{eV}$
$N_c = 7 \times 10^{20}\,\mathrm{cm}^{-3}$	$N_{vt}/kT_{vt} = 4.1 \times 10^{17}\,\mathrm{cm}^{-3}\mathrm{eV}^{-1}$	$E_c - E_v = 1.7\,\mathrm{eV}$
$\sigma_t = 1 \times 10^{-15}\,\mathrm{cm}^2$	$T_{ct} = 1500\,\mathrm{K}$	$T_{vt} = 3000\,\mathrm{K}$
$v_{th} = 10^7\,\mathrm{cm/s}$	$\mu_n^e = 10\,\mathrm{cm}^2/\mathrm{Vs}$	$\nu_0 = 10^{12}\,\mathrm{s}^{-1}$
$\kappa = 2$	$\epsilon_s = 1.05 \times 10^{-12}\,\mathrm{F/cm}$	$d = 1.5\,\mu\mathrm{m}$
simulation 4 with additional dangling bonds:		
additional parameters and modified parameters		
$\sigma_{db}^0 = 1 \times 10^{-15}\,\mathrm{cm}^2$	$N_{db} = 1.6 \times 10^{15}\,\mathrm{cm}^{-3}$	$E_c - E_{db}^- = 0.6\,\mathrm{eV}$
$\sigma_{db}^+ = 5 \times 10^{-15}\,\mathrm{cm}^2$	$N_c = 3 \times 10^{20}\,\mathrm{cm}^{-3}$	$E_c - E_{db}^0 = 1.0\,\mathrm{eV}$
	$N_{ct}/kT_{ct} = 3.2 \times 10^{18}\,\mathrm{cm}^{-3}\mathrm{eV}^{-1}$	$T_{ct} = 1000\,\mathrm{K}$
	$N_{vt}/kT_{vt} = 1.0 \times 10^{19}\,\mathrm{cm}^{-3}\mathrm{eV}^{-1}$	$T_{vt} = 2000\,\mathrm{K}$

ure 5.10, correspond reasonably well. We have also plotted the apparent density of gap states as obtained by the step-by-step method, since this is a differential technique that can show other details and can help to interpret the difference between the simulation and experiment. In figure 5.11 the apparent density of gap states is shown. It can be seen that the simulation describes the temperature dependence quite well. The trap level increases the apparent density of gap states with increasing temperature due to the broadening of the Fermi-Dirac distribution. The origin of the trap level is most likely not an impurity level, but the conduction band tail states that are caused by the intrinsic disorder. These tail states are close to E_c and very steep, so they can be easily modeled with a trap level at 0.12 eV below E_c.

The simulation shown in the figures 5.10 and 5.11 have the largest error near E_f. We tried to improve the simulation by adding dangling bonds to the density of gap states, since the dangling bonds are close to E_f. We have optimized the total number of dangling bonds N_{db}, and for the other parameters we have used values obtained from the literature. The values for the parameters are listed in table 5.3. The results of this simulation are shown in figure 5.12 and figure 5.13. It is clear that the added dangling bonds improve the fit near the Fermi level. The density of gap states that corresponds with the input parameters of simulation 4 is shown in figure 5.14.

The tail states increase the apparent density of gap states, and they increase the slope of the apparent gap states distribution as can be seen in figure 5.11. The slope of the gap states distribution is related to the characteristic temperature (T_c). An increase in the slope means a decrease in T_c. This explains the temperature dependence of T_c that is shown in figure 5.4. With increasing temperature the influence of the tail states increases, and the slope of the apparent density of gap states versus E increases which means a decrease in T_c.

The increase in T_c with increasing layer thickness can be explained by two effects. The first is the influence of the space charge regions that moves the Fermi level close to the tail states for thin samples. The second effect is that for a constant electric field the space charge density is proportional to the inverse layer thickness. Because we have measured all devices up to a maximum field of 10^5 V/cm, the maximum space charge density decreases with increasing layer thickness. The result is that the shift in the Fermi level is less for thick samples compared to thin samples, and this means that the Fermi level is closer to the tail states for thin samples. When the Fermi level is close to the tail states, the influence of the tail states is large which, reduces T_c.

5.6 Conclusions

In section 5.2 the step-by-step method, which is used to obtain the density of gap states from the I-V characteristics, was analyzed. An exponential distribution of gap states, with $T_c/T = 3$, was used to estimate the errors of the step-by-step method. The error in the density of gap states caused by the deviation from a uniform space charge, which is assumed in the step-by-step method, was estimated to be about 25%. The error in the density of gap states caused by the deviation from a step function of the Fermi-Dirac distribution was estimated to

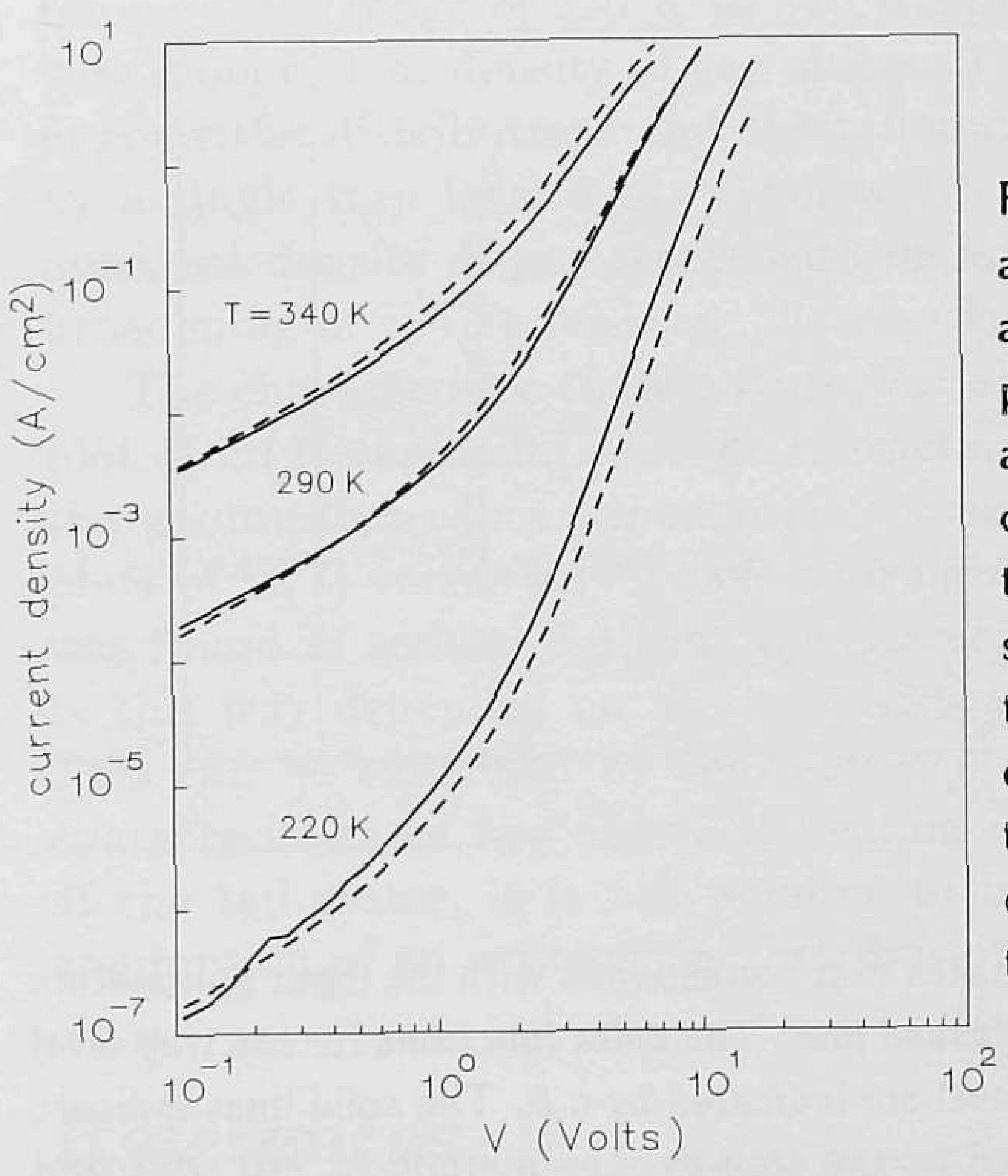

Figure 5.12: The simulated and experimental current-voltage characteristics. The experimental data is drawn with a solid line, and the simulated data with a dashed line. For the simulation a density of gap states was used consisting of two exponential distributions, dangling bonds, and a single trap level. The input parameters are listed under simulation 4.

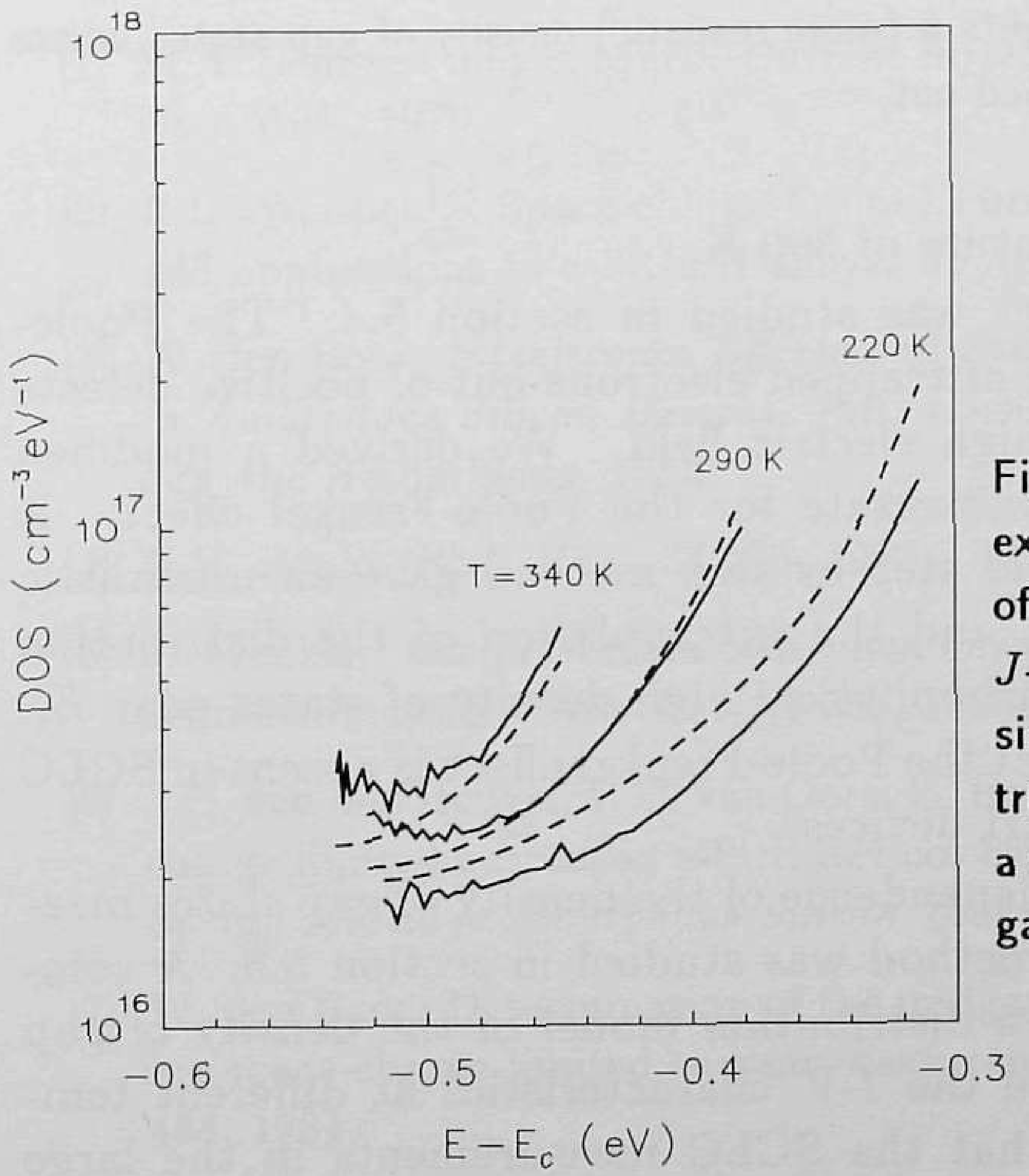

Figure 5.13: The simulated and experimental apparent density of gap states obtained from the J-V characteristics. For the simulation two exponential distributions, dangling bonds, and a single trap level were used as gap states.

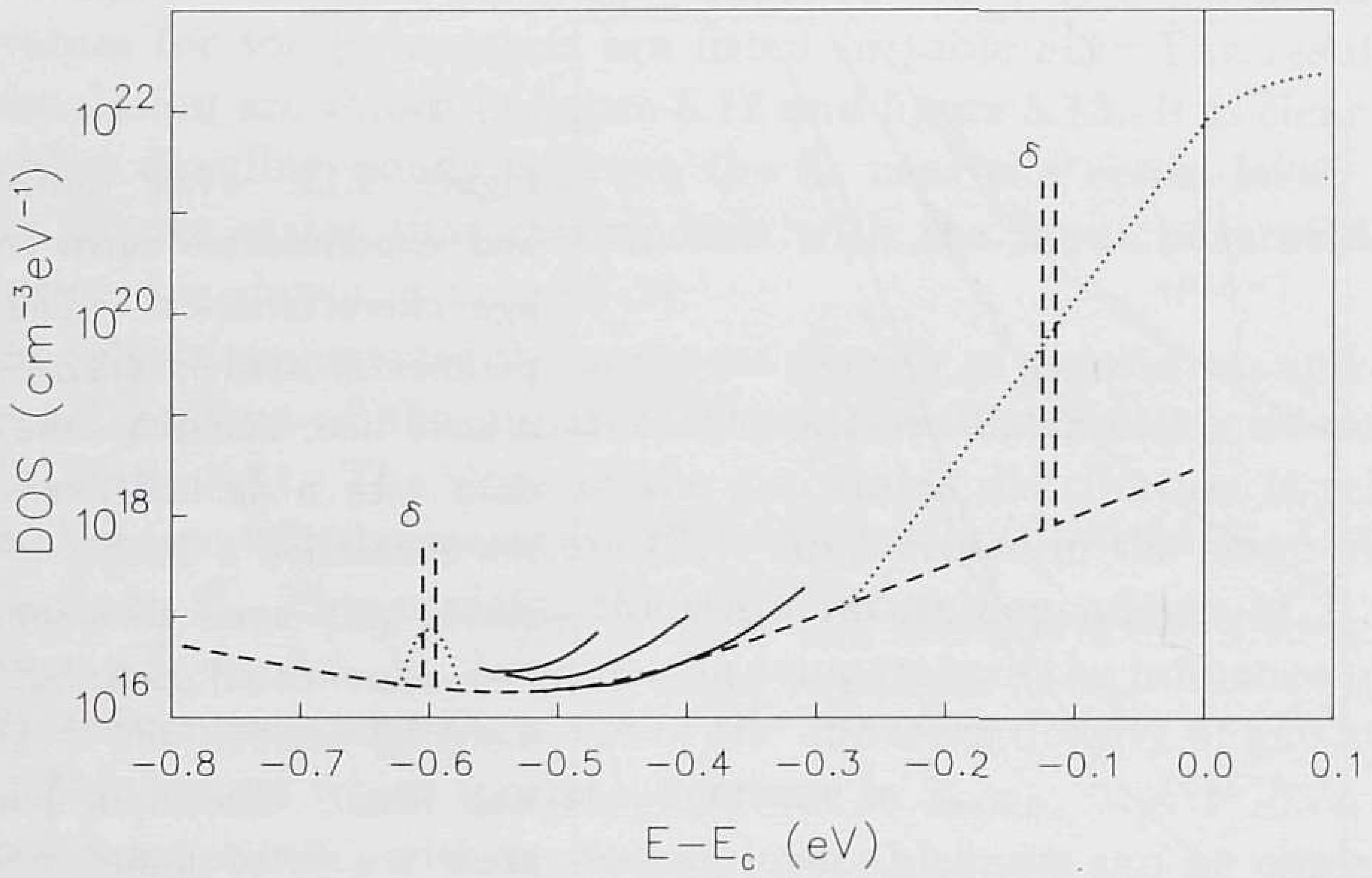

Figure 5.14: The density of gap states that corresponds with the input parameters of simulation 4 is indicated by a dashed line. The delta functions for the trap level and the negative dangling bond level are indicated by a δ. The solid lines indicate the density of gap states obtained by the step-by-step method at 220, 290, and 340 K. The dotted line represents a (more realistic) density of gap states where the delta functions are smoothed out.

be about 20% at a temperature of 300 K.

The Poole-Frenkel effect was studied in section 5.4. The Poole-Frenkel effect is the release of trapped electrons out of positive defects under the influence of a high electric field. We derived a modified step-by-step method to compensate for the Poole-Frenkel effect. It was found that the modified step-by-step method gave an unrealistic high density of gap states, and the extrapolation of the distribution of gap states to E_c gave an unphysical high density of states near E_c. Therefore, we concluded that the Poole-Frenkel effect is absent in SCLC measurements of n-i-n a-Si:H devices.

The large temperature dependence of the density of gap states measured by the step-by-step method was studied in section 5.5. A computer simulation based on a distribution model of the density of gap states was used to simulate the *I-V* characteristics at different temperatures. It was found that the SCLC measurements in the large temperature range of 220 K to 340 K can be explained by a temperature independent density of gap states. These gap states consist of two exponential distributions and the tail states near E_c that are modeled by a single trap level 0.12 eV below E_c. The tail states increase the apparent density of gap states with increasing temperature due to the broadening of the Fermi-Dirac distribution.

The characteristic temperature was obtained from the slope of the plot of $\ln(I)$ versus $\ln(V)$. The characteristic temperature is based on the assumption of an exponential distribution of gap states. All the plots of $\ln(I)$ versus $\ln(V)$ gave a straight line in the SCLC regime. It was found in section 5.4 that the characteristic temperature obtained in this way depended on the temperature and on the layer thickness. This can be explained by the influence of the tail states on the *I-V* characteristics as was shown in section 5.5. Because of the influence of the tail states, it is not possible to investigate the validity of the assumption of an exponential distribution.

References

[1] M.A. Lampert and P. Mark. *Current Injection in Solids*. Academic Press, New York, 1970.

[2] R.L. Weisfield. Space-charge-limited currents: refinements in analysis and applications to a-SiGe:H alloys. *J. Appl. Phys.*, 54:6401, 1983.

[3] W. den Boer. *Interference Effects and Space-Charge-Limited Conduction in Amorphous Silicon Devices*. PhD thesis, Delft University of Technology, the Netherlands, 1983.

[4] H.H. Poole. *Phil. Mag.*, 34:195, 1917.

[5] J. Frenkel. On pre-breakdown phenomena in insulators and electronic semi-conductors. *Phys. Rev*, 54:657, 1938.

[6] J.C. van den Heuvel, R.C. van Oort, B. Bokhorst, and M.J. Geerts. Space charge limited current in a-Si:H devices using high electric fields. In *MRS Spring Meeting: Amorphous Silicon Technology*, 1989.

[7] W. den Boer. Determination of the midgap density of states in a-Si:H using space-charge-limited current measurements. *J. de Phys.*, 42(C4):451–454, 1981.

[8] R.C. van Oort. *Hydrogenated Amorphous and Microcrystalline Silicon Deposited from Silane-Hydrogen Mixtures.* PhD thesis, Delft University of Technology, the Netherlands, 1989.

[9] J. Sworakowski and S. Nespurek. On the determination of the density of states in inhomogeneous samples for steady-state space-charge-limited currents. *J. Appl. Phys.*, 65(4):1559–1565, 1989.

[10] M.A. Lampert and P. Mark. *Current Injection in Solids*, pages 72–76. Academic Press, New York, 1970.

[11] R.H. Jarman. A note on the analysis of space-charge-limited current data. *J. Appl. Phys.*, 60(3):1210–1211, 1986.

[12] S. Ashok, P.A. Lester, and S.J. Fonash. Evidence of space-charge-limited current in amorphous silicon Schottky diodes. *IEEE Electron Dev. Lett.*, 1(10):200–202, 1980.

[13] N.W. Ashcroft and N.D. Mermin. *Solid State Physics*, pages 760–761. Holt-Saunders International Editions, 1976.

[14] A.K. Jonscher. Electronic conduction in amorphous semiconductors. *J. Vac. Sci. Technol.*, 8(1):135–144, 1971.

[15] J.G. Simmons. Poole-frenkel effect and Schottky effect in metal-insulator-metal systems. *Physical Review*, 54(3):657–660, 1967.

[16] C.A. Hogarth and M. Zor. Observations of the anomalous Poole-Frenkel effect in al-polyethylene-al thin film structures. *Phys. Stat. Sol. (a)*, 98:611–616, 1986.

[17] W.K Choi, J.J. Delima, and A.E. Owen. A model for the variations in the field-dependent behaviour of the Poole-Frenkel effect. *Phys. Stat. Sol. (b)*, 137:345–351, 1986.

[18] C.A. Dimitriadis, L. Papadimitrou, J. Stoemenos, N.A. Economou, D.B. Meakin, and P.A. Coxon. Conduction in n-i-n thin film polycrystalline/silicon devices in relation to the film deposition conditions. *J. Appl. Phys.*, 63(4):1104–1110, 1988.

[19] S. Furukawa, T. Kagawa, and N. Matsumoto. Estimation of localized state distribution profiles in undoped and doped a-Si:H by measuring space-charge-limited current. *Solid State Comm.*, 44(6):927–930, 1982.

[20] N.F. Mott and E.A. Davis. *Electronic Processes in Non-Crystalline Materials*, page 211. Clarendon Press, Oxford, 2 edition, 1979.

[21] D. Adler. *Semiconductors and Semimetals*, chapter 14, pages 291–318. Volume 21A, Academic Press, London, 1984.

[22] M. Kastner, D. Adler, and H. Fritzsche. Valence-alternation model for localized gap states in lone-pair semiconductors. *Phys. Rev. Lett.*, 37(22):1504–1507, 1976.

[23] H. Kahnt, F. Schirrmeister, and A. Feltz. The Poole-Frenkel effect in the model of charged dangling bonds. *Phys. Stat. Sol. (a)*, 57:K183–K185, 1980.

[24] T. Tiedje. *Semiconductors and Semimetals*, chapter 6, pages 207–238. Volume 21C, Academic Press, London, 1984.

[25] A. Doghmane and W.E. Spear. Determination of the recombination rate constants in amorphous silicon from double-injection experiments. *Phil. Mag. B*, 53(6):463–475, 1986.

[26] P.G. Le Comber and W.E. Spear. The energy of the dangling-bond states in a-Si. *Phil. Mag. B*, 53(1):L1, 1986.

Appendix A

Simulation of the Reflection and Transmission

In this appendix the calculation of R and T for a number of optical systems is described. The following optical systems are treated:

- A single non-absorbing layer, coherent or incoherent.
- A single absorbing layer.
- A thin film (coherent) on a substrate (incoherent).
- The method to obtain R and T for a large number of layers.

A layer is considered to be coherent if its thickness is much smaller than the coherence length of the light that is used. Likewise, a layer is considered to be incoherent if its thickness is much larger than the coherence length. The coherence length is determined by the light source and the bandwidth of the monochromator.

The light emitted by a thermal light source, such as a tungsten filament lamp, consists of short wave-trains. Since the phases of these wave-trains are independent, the coherence length is the average length of the wave-trains. A lifetime of 10^{-9} sec for atomic fluorescence lifetimes gives a coherence length in the order of a mm [1]. The coherence length caused by the bandwidth $\Delta\lambda$ of the monochromator is [2]

$$\ell_c = \frac{\lambda^2}{\Delta\lambda} \cdot \frac{1}{2\pi} . \tag{A.1}$$

The bandwidth of the monochromator is 1 nm and this gives a coherence length of about $100\,\mu$m at $\lambda = 1\,\mu$m. The coherence length obtained by combining these two effects is the smallest value, i.e. $100\,\mu$m.

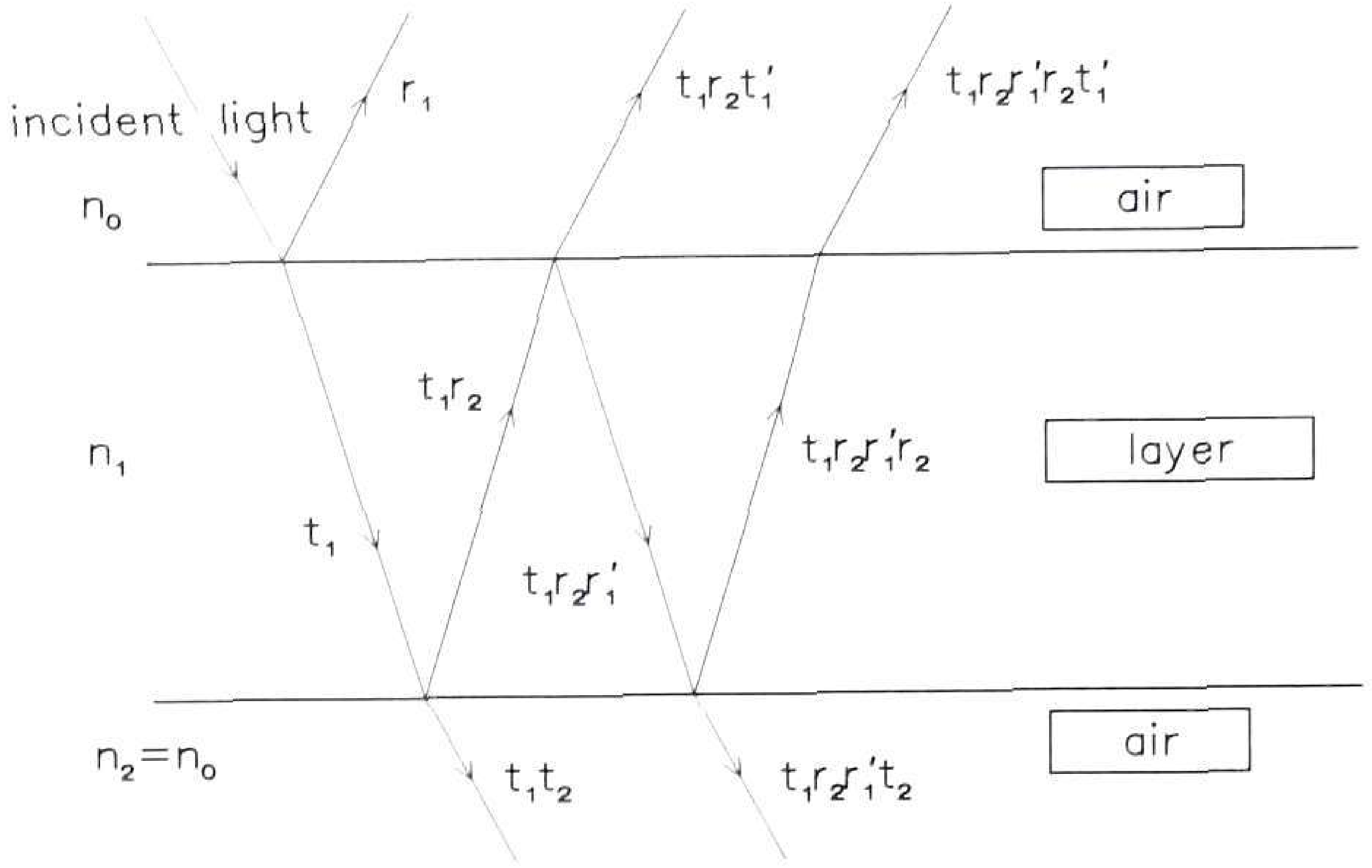

Figure A.1: The multiple reflections in a single layer.

The thickness of the a-Si:H layer is around $1\,\mu$m and can be considered as coherent. The thickness of the Corning 7059 substrate is 0.5 mm and can be considered as incoherent.

A single layer

In the case of a single layer we have two boundaries, namely between air and the layer and between the layer and air. This situation is depicted in figure A.1. The notation is the same as used by O.S. Heavens [3]. The multiple reflections in the film complicate the calculation of the reflection and transmission. There are two cases to be distinguished, namely that the multiple reflections add coherently or incoherently.

If the multiple reflections add coherently we have to add the amplitudes to obtain a combined reflection and a combined transmission coefficient. These combined coefficients are given by

$$\tilde{r}_{1,2} = r_1 + t_1t_1'r_2\,e^{-2i\delta_1}\sum_{k=0}^{\infty}(r_2r_1'\,e^{-2i\delta_1})^k = r_1 + \frac{t_1t_1'r_2\,e^{-2i\delta_1}}{1 - r_2r_1'\,e^{-2i\delta_1}} , \tag{A.2}$$

and

$$\tilde{t}_{1,2} = t_1 t_2\, e^{-i\delta_1} \sum_{k=0}^{\infty} (r_2 r_1'\, e^{-2i\delta_1})^k = \frac{t_1 t_2\, e^{-i\delta_1}}{1 - r_2 r_1'\, e^{-2i\delta_1}}\,, \tag{A.3}$$

where

$$\delta_1 = \frac{2\pi}{\lambda} n_1 d_1\,. \tag{A.4}$$

The Fresnel coefficients r_1, r_2, r_1', t_1, t_2, and t_1' are defined as

$$r_1 = \frac{n_0 - n_1}{n_0 + n_1}\,, \quad r_2 = \frac{n_1 - n_2}{n_1 + n_2}\,, \quad r_1' = \frac{n_1 - n_0}{n_0 + n_1}\,,$$

$$t_1 = \frac{2n_0}{n_0 + n_1}\,, \quad t_2 = \frac{2n_1}{n_1 + n_2}\,, \quad \text{and} \quad t_1' = \frac{2n_1}{n_0 + n_1}\,. \tag{A.5}$$

where n_0 is the refractive index of the first medium, n_1 is the refractive index of the second medium, and n_2 is the refractive index of the third medium. The phase shift δ_1 is described in terms of the wavelength λ, the refractive index of the layer n_1, and the layer thickness d_1. The phase shift δ_1 is the shift in phase of the light wave when it travels from the top to the end of the layer. From equation A.5 it can be seen that $r_1' = -r_1$ and $r_1^2 + t_1 t_1' = 1$. Using these expressions the reflection coefficient of equation A.2 can be written as

$$\tilde{r}_{1,2} = \frac{r_1 + r_2\, e^{-2i\delta_1}}{1 + r_2 r_1\, e^{-2i\delta_1}}\,. \tag{A.6}$$

The reflection and transmission are obtained with

$$R = |\tilde{r}_{1,2}|^2 \quad \text{and} \quad T = (n_2/n_0)|\tilde{t}_{1,2}|^2\,. \tag{A.7}$$

It can be seen from equation A.6 that the reflection is minimal for $\exp(-2i\delta_1) = 1$ and maximal for $\exp(-2i\delta_1) = -1$ if $n_1 > n_0$ and $n_1 > n_2$ ($r_1 < 0$ and $r_2 > 0$). These extrema in the reflection occur when the double layer thickness equals an integer multiple of the half wavelength in the layer (the wavelength in the layer is λ/n_1).

If the multiple reflections add incoherently we have to add the energies (i.e., the square of the amplitudes), in this case the reflection and transmission are

$$R = r_1^2 + t_1^2 t_1'^2 r_2^2 \sum_{k=0}^{\infty} (r_2^2 r_1'^2)^k = r_1^2 + \frac{t_1^2 t_1'^2 r_2^2}{1 - r_2^2 r_1'^2}\,, \tag{A.8}$$

and

$$T = \frac{n_2}{n_0} t_1^2 t_2^2 \sum_{k=0}^{\infty} (r_2^2 r_1'^2)^k = \frac{n_2}{n_0} \frac{t_1^2 t_2^2}{1 - r_2^2 r_1'^2}\,. \tag{A.9}$$

A single absorbing layer

The absorption of the layer can be introduced by using a complex refractive index

$$\tilde{n}_1 = n_1 - ik_1\,, \qquad \text{where} \qquad k_1 = \frac{\lambda\alpha_1}{4\pi}\,. \tag{A.10}$$

The absorption coefficient is given by α_1, and k_1 is the extinction coefficient of the layer. In the case of absorption the Fresnel coefficients are also complex numbers, for example

$$\tilde{t}_1 = \frac{2n_0}{n_0 + n_1 - ik_1}\,. \tag{A.11}$$

The phase shift is also a complex number

$$\tilde{\delta}_1 = \frac{2\pi}{\lambda} d_1 (n_1 - ik_1) = \delta_1 - \frac{i}{2}\alpha_1 d_1\,, \tag{A.12}$$

where the imaginary part of $\tilde{\delta}_1$ introduces the absorption.

In the case of a coherent layer the combined reflection coefficient and the combined transmission coefficient are

$$\tilde{r}_{1,2} = \tilde{r}_1 + \frac{\tilde{t}_1 \tilde{t}_1' \tilde{r}_2\, e^{-2i\delta_1} e^{-\alpha_1 d_1}}{1 - \tilde{r}_2 \tilde{r}_1'\, e^{-2i\delta_1} e^{-\alpha_1 d_1}} = \frac{\tilde{r}_1 + \tilde{r}_2\, e^{-2i\delta_1} e^{-\alpha_1 d_1}}{1 + \tilde{r}_2 \tilde{r}_1\, e^{-2i\delta_1} e^{-\alpha_1 d_1}}\,, \tag{A.13}$$

and

$$\tilde{t}_{1,2} = \frac{\tilde{t}_1 \tilde{t}_2\, e^{-i\delta_1} e^{-\alpha_1 d_1/2}}{1 - \tilde{r}_2 \tilde{r}_1'\, e^{-2i\delta_1} e^{-\alpha_1 d_1}} = \frac{\tilde{t}_1 \tilde{t}_2\, e^{-i\delta_1} e^{-\alpha_1 d_1/2}}{1 + \tilde{r}_2 \tilde{r}_1\, e^{-2i\delta_1} e^{-\alpha_1 d_1}}\,, \tag{A.14}$$

using $\tilde{r}_1' = -\tilde{r}_1$ and $\tilde{r}_1^2 + \tilde{t}_1 \tilde{t}_1' = 1$. The complex reflection coefficients $\tilde{r}_1$ and $\tilde{r}_2$ can be approximated by $|\tilde{r}_1|$ and $|\tilde{r}_2|$ since their imaginary part is much smaller than their real part. For example, a-Si:H has $n_1 = 4$ and $k_1 = 0.4$ at $\lambda = 500\,\text{nm}$ ($\alpha = 10^5\,\text{cm}^{-1}$), which gives for $\tilde{r}_2$ ($n_2 = 1$)

$$\tilde{r}_2 = \frac{\tilde{n}_1 - n_2}{\tilde{n}_1 + n_2} \approx 0.6 - 0.03\,i\,. \tag{A.15}$$

The reflection and transmission can be approximated by

$$R = |\tilde{r}_{1,2}|^2 \approx \frac{|\tilde{r}_1|^2 + 2|\tilde{r}_1||\tilde{r}_2|\, e^{-\alpha_1 d_1} \cos 2\delta_1 \; + |\tilde{r}_2|^2\, e^{-2\alpha_1 d_1}}{1 + 2|\tilde{r}_2||\tilde{r}_1|\, e^{-\alpha_1 d_1} \cos 2\delta_1 \; + |\tilde{r}_2|^2\, |\tilde{r}_1|^2\, e^{-2\alpha_1 d_1}} \tag{A.16}$$

and

$$T = \frac{n_2}{n_0}\, |\tilde{t}_{1,2}|^2 \approx \frac{(1 - |\tilde{r}_1|^2)(1 - |\tilde{r}_2|^2)\, e^{-\alpha_1 d_1}}{1 + 2|\tilde{r}_2||\tilde{r}_1|\, e^{-\alpha_1 d_1} \cos 2\delta_1 \; + |\tilde{r}_2|^2\, |\tilde{r}_1|^2\, e^{-2\alpha_1 d_1}}\,, \tag{A.17}$$

using $(n_2/n_0)\tilde{t}_1^2\tilde{t}_2^2 = (1 - \tilde{r}_1^2)(1 - \tilde{r}_2^2)$.

In the case of a incoherent layer the reflection and transmission are

$$R = |\tilde{r}_1|^2 + \frac{|\tilde{t}_1|^2\, |\tilde{t}'_1|^2\, |\tilde{r}_2|^2\, e^{-2\alpha_1 d_1}}{1 - |\tilde{r}_2|^2\, |\tilde{r}'_1|^2\, e^{-2\alpha_1 d_1}}\,, \tag{A.18}$$

and

$$T = \frac{n_2}{n_0}\, \frac{|\tilde{t}_1|^2\, |\tilde{t}_2|^2\, e^{-\alpha_1 d_1}}{1 - |\tilde{r}_2|^2\, |\tilde{r}'_1|^2\, e^{-2\alpha_1 d_1}}\,. \tag{A.19}$$

A thin film on a substrate

We measured the reflection and transmission of intrinsic layers of a-Si:H on Corning 7059 glass substrates, where the optical system consists of a coherent layer on top of an incoherent non-absorbing substrate. The a-Si:H layer can be described by a complex reflection and transmission coefficient, which are given by equations A.13 and A.14. Now equations A.8 and A.9 for the reflection and transmission of an incoherent non-absorbing layer can be modified by replacing r_1 with $\tilde{r}_{1,2}$, t_1 with $\tilde{t}_{1,2}$, r'_1 with $\tilde{r}'_{1,2}$, and t'_1 with $\tilde{t}'_{1,2}$. The $\tilde{r}'_{1,2}$ and $\tilde{t}'_{1,2}$ can be obtained in a similar way as $\tilde{r}_{1,2}$ and $\tilde{t}_{1,2}$.

This gives for the reflection and transmission

$$R = |\tilde{r}_{1,2}|^2 + \frac{|\tilde{t}_{1,2}|^2\, |\tilde{t}'_{1,2}|^2\, |r_3|^2}{1 - |r_3|^2\, |\tilde{r}'_{1,2}|^2}\,, \tag{A.20}$$

and

$$T = \frac{n_3}{n_0}\, \frac{|\tilde{t}_{1,2}|^2\, |t_3|^2}{1 - |r_3|^2\, |\tilde{r}'_{1,2}|^2}\,. \tag{A.21}$$

A large number of layers

Since a single film can be replaced by a single surface with a complex reflection and transmission coefficient, it is clear that any number of coherent layers can be replaced by a single surface [4,5]. The following recurrence relations can be used to compress any number of coherent layers.

$$\begin{aligned}
\tilde{r}_{1,2\ldots N+1} &= \tilde{r}_{1,2\ldots N} + \tilde{t}_{1,2\ldots N}\tilde{t}'_{1,2\ldots N}\tilde{r}_{N+1}\, \tilde{e}_N^2/\tilde{c}_N\,, && \text{(A.22a)}\\
\tilde{t}_{1,2\ldots N+1} &= \tilde{t}_{1,2\ldots N}\tilde{t}_{N+1}\, \tilde{e}_N/\tilde{c}_N\,, && \text{(A.22b)}\\
\tilde{r}'_{1,2\ldots N+1} &= \tilde{r}'_{N+1} + \tilde{t}'_{N+1}\tilde{t}_{N+1}\tilde{r}'_{1,2\ldots N}\, \tilde{e}_N^2/\tilde{c}_N\,, && \text{(A.22c)}\\
\tilde{t}'_{1,2\ldots N+1} &= \tilde{t}'_{N+1}\tilde{t}'_{1,2\ldots N}\, \tilde{e}_N/\tilde{c}_N\,, && \text{(A.22d)}
\end{aligned}$$

where

$$\tilde{c}_N = 1 - \tilde{r}_{N+1}\tilde{r}'_{1,2\ldots N}\, \tilde{e}_N^2 \qquad \text{and} \qquad \tilde{e}_N = e^{-i\delta_N} e^{-\alpha_N d_N/2}\,. \tag{A.23}$$

The Fresnel coefficients $\tilde{r}_{N+1}$, $\tilde{r}'_{N+1}$, $\tilde{t}_{N+1}$, and $\tilde{t}'_{N+1}$ are given by

$$\tilde{r}_{N+1} = \frac{\tilde{n}_N - \tilde{n}_{N+1}}{\tilde{n}_N + \tilde{n}_{N+1}}\,, \quad \tilde{r}'_{N+1} = \frac{\tilde{n}_{N+1} - \tilde{n}_N}{\tilde{n}_N + \tilde{n}_{N+1}}\,,$$

$$\tilde{t}_{N+1} = \frac{2\tilde{n}_N}{\tilde{n}_N + \tilde{n}_{N+1}}\,, \quad \text{and} \quad \tilde{t}'_{N+1} = \frac{2\tilde{n}_{N+1}}{\tilde{n}_N + \tilde{n}_{N+1}}\,. \tag{A.24}$$

After all the coherent layers are replaced by a single surface the optical system consists of a single surface or an incoherent layer (the substrate). The reflection and transmission can be calculated by using the $\tilde{r}$ and $\tilde{t}$ of the single surface, or in case of a remaining incoherent layer by making use of equations A.18 and A.19.

References

[1] P.W. Milonni and J.H. Eberly. *Lasers*, page 5. John Wiley & Sons, 1988.

[2] L. Ley. *Topics in Applied Physics*, chapter 3, page 127. Volume 56, Springer-Verlag, 1984.

[3] O.S. Heavens. *Optical Properties of Thin Solid Films.* Butterworths, London, 1955.

[4] P. Rouard. *Ann. d. Physique*, 7:291, 1937.

[5] A. Vasicek. *J. de Phys.*, 11:342, 1950.

List of Tables

List of Figures

List of Symbols

A	constant, depends on boundary conditions
A^*	Richardson constant
B	constant used in the Tauc relation
C_{H}	hydrogen concentration in the a-Si:H layer
d	layer thickness
D_p	hole diffusion coefficient
E	energy
E_c	energy of the conduction band edge
E_{db}^-	energy level of negative dangling bond level
E_{db}^0	energy level of neutral dangling bond level
E_f	energy of the Fermi level
E_g	bandgap, optical gap
$E_n(\vec{k})$	energy, solution of Bloch's theorem
E_t	energy level of traps
E_v	energy of the valence band edge
$\mathcal{E}$	electric field
$\mathcal{E}_S$	surface electric field
$f(E)$	Fermi-Dirac distribution
F_1	integrating factor
F_2	integrating factor
G	generation
$g(E)$	density of states
$g_{ct}(E)$	deep tail states of the conduction band
$g_{vt}(E)$	deep tail states of the valence band
h	Planck's constant
$h\nu$	photon energy
$\hbar$	$h/2\pi$
$\hbar\omega_g$	Penn gap
I	current
I_{ph}	photon flux
I_{sc}	short-circuit current
J	current density
J_0	saturation current density

J_n	electron current density
J_p	hole current density
J_p^{diff}	hole diffusion current density
J_p^{drift}	hole drift current density
k	Boltzmann constant
k	extinction coefficient
$\mathrm{k_o}$	integer, $\mathrm{k_o} = 1, 2, 3\ldots$
$\vec{k}$	wave vector
L_d	ambipolar diffusion length
L_p	hole diffusion length in crystalline material
ℓ	T_c/T
ℓ_c	coherence length
m	electron mass
N_0	constant, magnitude of exponential distribution
N_{ct}	density for the conduction band deep tail
N_c	effective density of states in the conduction band
$N_c(E)$	conduction band density of states
N_{db}	dangling bond density, $N_{db} = N_{db}^0 + N_{db}^- + N_{db}^+$
N_{db}^+	density of positive dangling bonds
N_{db}^-	density of negative dangling bonds
N_{db}^0	density of neutral dangling bonds
n	diode ideality factor
n_{ct}	electron concentration in the conduction band tail
n_e	electron concentration in extended states
n_i	intrinsic carrier concentration
n_t	total electron concentration
N_t	trap density, $N_t = N_t^- + N_t^0$
N_t^-	density of negative traps
N_t^0	density of neutral traps
N_{vt}	density for the valence band deep tail
$N_v(E)$	valence band density of states
$N_{\mathrm{c\text{-}Si}}$	number of atoms per unit volume in crystalline silicon
N_{H}	number of hydrogen atoms per unit volume
$N_{\mathrm{Si-H}}$	number of Si–H bonds per unit volume
$N_{\mathrm{Si-Si}}$	number of Si–Si bonds per unit volume
N_{Si}	number of silicon atoms per unit volume
N_{os}	number of oscillators per unit volume

n	refractive index
n_∞	refractive index at long wavelengths
n_{max}	refractive index at maximum reflection point
p	hole concentration in crystalline material
p_0	equilibrium hole concentration in crystalline material
p_e	hole concentration in extended states
p_t	total hole concentration
p_{vt}	hole concentration in the valence band tail
$P_{\mathrm{am}}(\omega)$	momentum matrix element for an amorphous semicond.
$P_{\mathrm{cr}}(\omega)$	momentum matrix element for a crystalline semicond.
q	elementary charge
Q_{ct}	charge density in the conduction band deep tail
Q_{db}	charge density in dangling bonds
Q_t	charge density in traps
Q_{vt}	charge density in the valence band deep tail
$\mathcal{Q}$	charge per unit area
r	reflection coefficient
R	reflection
r	space coordinate
R_{calc}	calculated reflection
R_{meas}	measured reflection
$\vec{r}$	space coordinate
$\vec{R}$	translation vector
s_{db}^+	capture constant of positive dangling bonds
s_{db}^0	capture constant of neutral dangling bonds
S_n	electron surface recombination velocity
S_p	hole surface recombination velocity
s_t	capture constant of traps, $s_t = \sigma_t v_{th}/\nu_0$
T	absolute temperature
t	transmission coefficient
T	transmission
T_{ct}	characteristic temp. of the cond. band deep tail
T_c	characteristic temperature
T_{vt}	characteristic temp. of the valence band deep tail
T_{calc}	calculated transmission
T_{meas}	measured transmission
U	potential energy

U	recombination
$U(\vec{r})$	periodic potential in a crystal
V	voltage
V_c	critical voltage
v_{th}	thermal velocity
W	depletion width
x	distance from the surface
α	absorption coefficient
α_p	polarizability
$\alpha_{\mathrm{Si-H}}$	polarizability of the Si–H bond
$\alpha_{\mathrm{Si-Si}}$	polarizability of the Si–Si bond
$\alpha_{\mathrm{SiH_4}}$	polarizability of the silane molecule
β_{pf}	Poole-Frenkel constant
γ	damping factor
δ	phase shift after light has travelled through a layer
$\epsilon(\omega)$	dielectric constant at optical frequencies
$\tilde{\epsilon}(\omega)$	complex dielectric constant at optical frequencies
ϵ_s	static dielectric constant
κ	constant, $1 < \kappa < 2$
λ	wavelength (in vacuum)
λ_{max}	wavelength at maximum reflection point
$\Delta\lambda$	bandwidth
μ_n	electron mobility in crystalline material
μ_n^d	electron drift mobility
μ_n^e	electron extended state mobility
μ_p	hole mobility in crystalline material
μ_p^d	hole drift mobility
ν	frequency
ν_0	release rate
σ	conductivity
σ_{db}^+	capture cross section of positive dangling bonds
σ_{db}^0	capture cross section of neutral dangling bonds
σ_t	trap capture cross section
τ_n	electron lifetime
τ_p	hole lifetime
ϕ	barrier height
$\psi(\vec{r})$	wave function

ω	angular frequency
ω_0	natural frequency of the oscillator
ω_1	$\omega_1^2 = \omega_0^2 - \omega_p^2/3$
ω_p	plasma frequency

Summary

Hydrogenated amorphous silicon (a-Si:H) is a relatively new semiconductor that is of practical use in a number of applications; it is also an interesting material from a scientific point of view. Hydrogenated amorphous silicon is an alloy of silicon and hydrogen atoms. The atoms are distributed in space in a more or less random way. This is in contrast with crystalline silicon where the silicon atoms are ordered in a regular pattern, i.e. the crystal lattice. The practical use of a-Si:H is largely based on the ability to deposit thin layers of a-Si:H on a wide range of cheap substrates and the ability to cover large areas. However, the electrical properties are inferior to those of crystalline silicon and much research is aimed at the improvement of the electrical properties.

In this thesis the optical properties and transport properties of a-Si:H are studied. These properties are closely related to the performance of a-Si:H solar cells, since the absorption of light and the transport of the generated electrons and holes determine the efficiency of the solar cell. The optical properties are studied in chapter 3 after the general introduction in chapter 1, and the description of the fabrication of the layers and devices of a-Si:H in chapter 2. The transport properties are studied in chapters 4 and 5. The investigation presented in this thesis is directed at increasing the understanding of the material in relation with the practical application of a-Si:H in solar cells.

In chapter 3 the optical properties of intrinsic layers of a-Si:H are studied. The reflection of light and the transmission of light of these layers were measured, and these measurements were used to obtain the refractive index and the optical gap. A model for the incorporation of hydrogen in the a-Si:H layer is introduced to describe the relations between the hydrogen concentration in the layer, the refractive index, and the optical gap. These theoretical relations agree with our experimental results and the experimental results of other research groups.

Reflection and transmission measurements were also used to study the inhomogeneity of microcrystalline silicon. Microcrystalline silicon (μc-Si:H) consists of microcrystals of approximately 100 Å in diameter surrounded by a-Si:H. This material (μc-Si:H) can be used for the

first layer in a solar cell, because of its low light absorption and high conductivity. It is shown that the first 200 Å of a μc-Si:H layer is amorphous. This thin interfacial layer has to be eliminated to obtain solar cells with a high efficiency.

The diffusion length of a-Si:H is studied in chapter 4. The diffusion length is the average distance that a generated hole travels before it recombines with an electron. The diffusion length of a-Si:H was measured with the Surface Photovoltage (SPV) technique. It is shown that the term "diffusion length" is misleading, since the hole drift current is of the same order of magnitude as the hole diffusion current. This hole drift current increases the diffusion length with a factor $\sqrt{2}$.

The SPV technique was used in combination with current-voltage measurements to measure the influence of the tin-oxide layer on the quality of the a-Si:H layer that was deposited on top of the tin-oxide layer. A tin-oxide layer is used as a transparent and highly conductive bottom layer in solar cells in order to collect the generated current. It is shown that tin atoms of the tin-oxide layer diffuse into the a-Si:H layer. However, current-voltage measurements and SPV measurements show no degradation of the quality of the a-Si:H layer as a result of this tin diffusion.

In chapter 5 the Space Charge Limited Current (SCLC) method is investigated. This SCLC method is used to obtain the density of states in the gap of a-Si:H. The influence of high electric fields, known as the Poole-Frenkel effect, on the measured density of gap states was studied. It is shown that high electric fields do not disturb the SCLC measurements. This result is a confirmation of the theoretical models for the gap states of a-Si:H.

The density of gap states obtained by the SCLC method show a large temperature dependence, however, the density of gap states of a-Si:H is supposed to be independent of the temperature. It is shown that the temperature dependence is caused by the tail states near the conduction band edge, and not by a change in the density of gap states.

Samenvatting

Gehydrogeneerd amorf silicium (a-Si:H) is een relatief nieuwe halfgeleider met verscheidene praktische toepassingen; het is tevens een interessant materiaal uit wetenschappelijk oogpunt. Gehydrogeneerd amorf silicium is een legering van silicium en waterstof atomen. De atomen bevinden zich op min of meer willekeurige plaatsen. Dit in tegenstelling tot kristallijn silicium, waar de silicium atomen geordend zijn volgens een regelmatig patroon, namelijk het kristalrooster. De praktische toepassingen van a-Si:H zijn voor een groot deel gebaseerd op de mogelijkheid om dunne lagen van a-Si:H op een verscheidenheid van goedkope substraten aan te brengen en de mogelijkheid om grote oppervlakken te bedekken. Echter, de elektrische eigenschappen zijn minder goed dan die van kristallijn silicium, en veel onderzoek is gericht op het verbeteren van de elektrische eigenschappen.

In dit proefschrift worden de optische eigenschappen en de transport eigenschappen van a-Si:H bestudeerd. Deze eigenschappen zijn sterk verbonden met de werking van a-Si:H zonnecellen, aangezien de licht absorptie en het transport van de gegenereerde elektronen en gaten het rendement van de zonnecel bepalen. De optische eigenschappen worden onderzocht in hoofdstuk 3 na de algemene inleiding in hoofdstuk 1, en de beschrijving van de vervaardiging van de lagen en de structuren van a-Si:H in hoofdstuk 2. De transport eigenschappen worden onderzocht in de hoofdstukken 4 en 5. Het onderzoek in dit proefschrift is gericht op het uitbreiden van het begrip van het materiaal in samenhang met de praktische toepassing van a-Si:H in zonnecellen.

In hoofdstuk 3 worden de optische eigenschappen van intrinsieke lagen van a-Si:H bestudeerd. De reflectie van licht en de transmissie van licht van deze lagen werden gemeten, en deze metingen werden gebruikt om de optische bandafstand en de brekingsindex te bepalen. Een model voor de inbouw van waterstof in de a-Si:H laag wordt geïntroduceerd om de relaties tussen de waterstof concentratie in de laag, de brekingsindex, en de optische bandafstand te beschrijven. Deze theoretische relaties komen overeen met onze experimentele resultaten en de experimentele resultaten van andere onderzoeks groepen.

Reflectie en transmissie metingen werden ook gebruikt om de inhomogeniteit van microkristallijn silicium te onderzoeken. Microkristallijn silicium (μc-Si:H) bestaat uit microkristallen met een diameter van ongeveer 100 Å omringd door a-Si:H. Dit materiaal (μc-Si:H) kan gebruikt worden voor de eerste laag in een zonnecel vanwege de lage licht absorptie en de hoge geleidbaarheid. De eerste 200 Å van een μc-Si:H laag blijkt amorf te zijn. Deze dunne tussenlaag moet vermeden worden om zonnecellen met een hoog rendement te vervaardigen.

De diffusielengte van a-Si:H wordt onderzocht in hoofdstuk 4. Deze diffusielengte is de gemiddelde afstand die een gegenereerd gat aflegt voordat deze recombineert met een elektron. De diffusie lengte van a-Si:H werd gemeten met de *Surface Photovoltage*[1] (SPV) techniek. Er wordt getoond dat de term "diffusielengte" misleidend is aangezien de driftstroom van de gaten van dezelfde orde van grootte is als de diffusiestroom van de gaten. Deze driftstroom van de gaten vergroot de diffusielengte met een factor $\sqrt{2}$.

De SPV techniek werd gebruikt om de invloed te bepalen van de tinoxide laag op de kwaliteit van de a-Si:H laag die bovenop de tinoxide laag werd aangebracht. Een tinoxide laag wordt gebruikt als een transparante en sterk geleidende onderlaag in zonnecellen om de gegenereerde stroom naar de kontakten te leiden. De tin atomen van de tinoxide laag blijken in de a-Si:H laag te diffunderen. Echter, stroomspanning metingen en SPV metingen laten geen degradatie van de a-Si:H laag zien als gevolg van deze tin diffusie.

In hoofdstuk 5 wordt de *Space Charge Limited Current*[2] (SCLC) methode onderzocht. Deze SCLC methode wordt gebruikt om de toestandsdichtheid tussen de valentie en geleidingsband van a-Si:H te bepalen. De invloed van hoge elektrische velden, bekend als het Poole-Frenkel effect, op de gemeten toestandsdichtheid werd onderzocht. Er wordt aangetoond dat hoge elektrische velden de SCLC metingen niet beïnvloeden. Dit resultaat is een bevestiging voor de theoretische modellen voor de toestandsdichtheid in a-Si:H.

De toestandsdichtheid die wordt verkregen met de SCLC methode is afhankelijk van de temperatuur, terwijl de toestandsdichtheid van a-Si:H als onafhankelijk van de temperatuur wordt beschouwd.

---

[1] Door licht gegenereerde spanning aan het oppervlak.

[2] De door ruimtelading begrensde stroom.

Er wordt aangetoond dat de temperatuur afhankelijkheid veroorzaakt wordt door de *tail* toestanden bij de rand van de geleidingsband, en niet door een verandering in de toestandsdichtheid.

Acknowledgements

The study described in this thesis was financially supported by the Netherlands Organization for Scientific Research. It was part of the ISES-Netherlands research program aimed at the development of amorphous silicon and gallium-arsenide solar cells.

The study described in this thesis could not have been carried out without the help of many people. First of all, I want to thank Ronald van Oort and Rien Geerts for their advice and for our numerous helpful discussions. I want to thank Barend Bokhorst, Humphry de Groot, and Tao Guoqiao, who contributed to this research during their electrotechnical engineering course.

I want to thank all my collegues in the Laboratory of Electrical Materials with whom it was a pleasure to work, in particular, Stefan Blasko, Jaap Hoekstra, Ben Jansen, Leon Jansen, Bram van der Male, Wim Metselaar, Gertjan Ouwerling, Nico Spiekerman, Jan-Chris Staalenburg, Jan van Staden, Wilf Stefan, Jannie Vermeulen, and Piet Zonneveld.

I also wish to express my appreciation to Ms. Jane Zaat-Jones for correcting the English text.

About the Author

Johan van den Heuvel was born in Sommelsdijk, the Netherlands, on October 7, 1959. After receiving his Atheneum-B diploma in 1979 from the Rijksscholengemeenschap Goeree-Overflakkee in Middelharnis, he studied physics at the University of Leiden. He graduated in 1985 on the subject of electron spin resonance in the spin-glass $\mathrm{Eu_xSr_{1-x}S}$. After his graduation he worked for several months as a physics teacher at the Rembrandt Scholengemeenschap in Leiden.

In December 1985 he became a research assistant at the Faculty of Electrical Engineering of Delft University of Technology where he has investigated the optical properties and transport properties of hydrogenated amorphous silicon.

Stellingen

behorend bij het proefschrift

"Optical Properties and Transport Properties
of
Hydrogenated Amorphous Silicon"

door J.C. van den Heuvel

Delft, 11 november 1989

1. *Door de krachtige en goedkope computers van dit moment hoeft een experiment niet meer geanalyseerd te worden met een sterk vereenvoudigd rekenmodel maar kan een complex rekenmodel gebruikt worden. Echter, een vereenvoudigd rekenmodel op maat gemaakt voor een specifiek experiment voldoet evengoed als een complex rekenmodel, geeft meer inzicht in de relevante processen en is sneller te ontwikkelen.*

2. *Het onderzoek naar ohmse kontakten voor GaAs zonnecellen moet zich meer op een lage kostprijs dan op een lage kontaktweerstand richten. Dit in tegenstelling tot GaAs laserdiodes, waarbij een lage kontaktweerstand het belangrijkste is.*

3. *Een oscillator model gecombineerd met een model voor de inbouw van waterstof in het a-Si:H netwerk kan de optische eigenschappen van a-Si:H als functie van de waterstof concentratie beschrijven.*

   Dit proefschrift, hoofdstuk 3.

4. *De stabiliteit in het onderwijs zou verbeteren als het onderwijs niet meer door de politiek misbruikt zou worden om maatschappelijke veranderingen te bewerkstelligen, zie de Mammoetwet en de Middenschool.*

5. *De diffusielengte van gaten in dunne lagen van a-Si:H is te meten met de "Surface Photovoltage" methode als de reflectie aan het achterkontakt wordt meegenomen in de uitdrukking voor de lichtgeneratie.*

   Dit proefschrift, hoofdstuk 4.

6. *De bedrijfjes die rondom een ondernemende universiteit ontstaan en op onduidelijke wijze gebruik kunnen maken van door de overheid gesubsidieerde faciliteiten veroorzaken concurrentie vervalsing ten opzichte van bedrijven die voor zulke faciliteiten moeten betalen.*

7. *Uit diffusielengte metingen en stroom-spanning metingen aan Schottky diodes blijkt dat de degradatie van a-Si:H zonnecellen tengevolge van tin diffusie uit de tinoxide laag te verwaarlozen is.*

   Dit proefschrift, hoofdstuk 4.

8. *De factor* $\sqrt{2}$ *in de formule van Moore voor de ambipolaire diffusielengte van a-Si:H is het gevolg van een elektrisch veld dat ontstaat door het verschil in beweeglijkheid tussen gaten en elektronen.*

   A.R. Moore, J. Appl. Phys., 54(1):222–228, 1983.
   Dit proefschrift, hoofdstuk 4.

9. *Doordat kwantitatieve modellen voor het sinteren van keramische poeders ontoereikend zijn, vindt de ontwikkeling van keramische filters, met een specifieke poriegrootte verdeling, proefondervindelijk plaats.*

   James S. Reed. Introduction to the Principles of Ceramic Processing, pages 445–464. John Wiley & Sons, 1988.

10. *Voor een economisch haalbare energie opwekking met zonnecellen, moet er voldoende grond beschikbaar zijn waar de opbrengst per hectare, bij plaatsing van zonnecellen, vergelijkbaar is met de opbrengst per hectare wanneer deze grond gebruikt wordt voor de landbouw.*

11. *Het ontbreken van een Poole-Frenkel effect in a-Si:H devices ondersteunt de theorie dat dangling bonds in a-Si:H een positieve correlatie energie hebben.*

    Dit proefschrift, hoofdstuk 5.

12. *Als het profijtbeginsel bij de studiefinanciering wordt doorgezet, dan kunnen er in de toekomst schadeclaims komen van studenten die niet voldoende profijt hebben gehad van de studie.*